Protein-level regulation of oncogenic RIT1 in non-small cell lung cancer

Amanda K. Riley

A dissertation

submitted in partial fulfillment of the

requirements for the degree of

Doctor of Philosophy

University of Washington

2024

Reading Committee:

Alice H. Berger, Chair

Susan Biggins

Lucas Sullivan

Program Authorized to Offer Degree:

Molecular and Cellular Biology

University of Washington

Abstract

Protein-level regulation of oncogenic RIT1 in non-small cell lung cancer

Amanda K. Riley

Chair of the Supervisory Committee:
Associate Professor Alice H. Berger
Human Biology Division, Fred Hutchinson Cancer Center

Lung cancer is the leading cause of cancer-related deaths worldwide. Non-small cell lung cancer is the most diagnosed type of lung cancer, and lung adenocarcinoma is the most prevalent subtype. Approximately 50% of lung adenocarcinoma tumors harbor druggable mutations in genes such as *EGFR* and *ALK*, and targeted therapies are highly effective at reducing tumor burden. Indeed, targeted therapies have revolutionized cancer treatment and are becoming standard of care over cytotoxic chemotherapy; however, many mutations are not clinically actionable. Up to 15% of lung adenocarcinoma tumors are driven by mutation or amplification of the RAS-family gene *RIT1*, and *RIT1* mutations do not co-occur with other canonical driver mutations. There is a growing understanding that the protein abundance of RIT1 is essential for its function. Therefore, inhibiting positive regulators of RIT1 abundance could be a tractable means of reducing tumor burden and abrogating the growth of tumors driven by *RIT1* mutations and amplifications.

Development of a RIT1-specific inhibitor is unlikely to succeed due to the structure of RIT1 as a GTPase. In 2013, groundbreaking work on KRAS resulted in the development of the first mutant-specific inhibitors, which represents a major advance in this field and for patient care. Such an approach for RIT1, however, would be quite difficult due to the resources required and our lack of knowledge pertaining to RIT1 biology and oncogenic mechanisms. Because of this, innovative approaches are needed to understand RIT1 genetic dependencies and uncover druggable targets.

The Berger Lab developed a CRISPR screening approach to discover genes required for *RIT1*-driven cellular transformation. From this work, we found that *RIT1*-mutant cells are uniquely dependent on genes associated with the Spindle Assembly Checkpoint (SAC), including Aurora kinases A and B. *RIT1*-mutant cells are more sensitive than *KRAS*-mutant cells to alisertib (an Aurora kinase A inhibitor) and barasertib (an Aurora kinase B inhibitor). Expression of mutant *RIT1* weakens the SAC, prompting cells to prematurely exit mitosis and accumulate mitotic abnormalities. In addition to the SAC vulnerability, we identified the deubiquitinase *USP9X* as a top essential gene in *RIT1*-mutant cells. This was particularly intriguing given that previous work has suggested that the protein abundance of RIT1 is important for its function. Indeed, although RIT1 shows high sequence homology to KRAS, RIT1 does not appear to be regulated in a similar manner (i.e. at the level of GAP resistance). Instead, RIT1 appears to be regulated at the level of protein abundance.

Here, I explore the hypothesis that RIT1 is a substrate of USP9X and found that USP9X binds to and deubiquitinates RIT1. I find that USP9X depletion decreases RIT1 protein abundance and stability, and loss of USP9X abrogates *RIT1*-driven cell growth and proliferation.

These findings increase our understanding of RIT1 biology and oncogenic mechanisms and nominate USP9X as a therapeutic target for the treatment of *RIT1*-driven diseases.

TABLE OF CONTENTS

LIST OF FIGURES

LIST OF TABLES

ACKNOWLEDGEMENTS

I want to thank current and former members of the Berger Lab for helping me design this project, conceive of and carry out experiments, and interpret the analyses presented in this dissertation. I first met Dr. Alice Berger during the interview weekend for the MCB program, and I was inspired by her enthusiasm and excitement for lung cancer genomics. Throughout my PhD, Alice's support and guidance has helped me become a better scientist. When I entered graduate school, I didn't have many lab skills beyond tissue culture, and being in Alice's lab provided me with opportunities to learn an incredible array of techniques and skills. I also want to thank a former postdoc in the lab—Dr. Athea Vichas—who mentored me during my rotation and provided many useful reagents and cell lines for the USP9X experiments.

Thank you to my former mentors—Dr. Marten Edwards, Dr. Amy Hark, and Dr. Elizabeth McCain—from Muhlenberg College, who guided me throughout my undergraduate training. The foundational knowledge that I obtained in biology helped me build upon this knowledge in graduate school. Thank you to Dr. Cyril Benes for being a wonderful PI while I was a research technician at the Massachusetts General Hospital in Boston. In his lab, I discovered my interest in cancer research, and I gained so much valuable insight about how science is done in this field.

Thank you to the MCB program, particularly Maia Low, for their unwavering support and for responding so promptly to all of my emails over the years. Also thank you to all of the admins and IT support at Fred Hutch, especially Luna Yu for fixing nearly all of my computer troubles throughout graduate school.

Finally, thank you to all of my incredible friends and partners. I could not have completed this PhD without your love and support.

Chapter 1. INTRODUCTION

A version of this chapter will be submitted in 2024 as a review article to the journal *Oncogene*.

1.1 CURRENT STATE OF LUNG CANCER RESEARCH

Lung cancer is the most common cause of cancer-related deaths worldwide (1). Approximately 75% of lung cancer cases are caused by mutations in the Receptor Tyrosine Kinase (RTK)/RAS signaling pathway (2). Mutations within this pathway—in genes such as *EGFR* (epidermal growth factor receptor) and *KRAS*—are mutually exclusive, meaning that tumors are often driven by one key oncogene (2). In the past decade, targeted therapies have revolutionized cancer treatment by offering a means to kill cancer cells that harbor specific oncogenic mutations. Targeted therapies are more effective and less toxic than non-selective, cytotoxic chemotherapy. Despite this progress, however, there are still oncogenes that cannot be targeted with currently available inhibitors.

1.2 RIT1 IN CANCER

Over the past 40 years, Ras guanosine triphosphate hydrolases (GTPases) have been characterized as potent oncogenes through their perturbation of the mitogen activated protein kinase (MAPK) signaling pathway (3–6). In addition to classical RAS proteins such as KRAS and NRAS, many other RAS-related proteins have been identified, including RIT1 (Ras-like in all tissues) (7–9). *RIT1* was first discovered in a study of gene expression from mouse retinas (8). As its name implies, *RIT1* is expressed across all tissues in embryos and adults, although it is more highly expressed in adult animals (8). In 2014, *RIT1* was identified as an oncogene in lung adenocarcinoma, and to date *RIT1* mutations and amplifications have been linked to several other

cancer types, including myeloid malignancies and endometrial cancer (9–11). In the context of lung cancer, *RIT1* is considered to be a "rare" oncogene since it occurs in ≤5% of cases (12). Given that close to 240,000 people will be diagnosed with lung cancer in 2023, even rare subtypes affect thousands of patients (13). Because of this and given the prevalence of RIT1 in other cancer types, further understanding RIT1 biology and oncogenic mechanisms is crucial for improving treatment options and patient outcomes.

1.3 Comparison of RIT1 to other RAS proteins

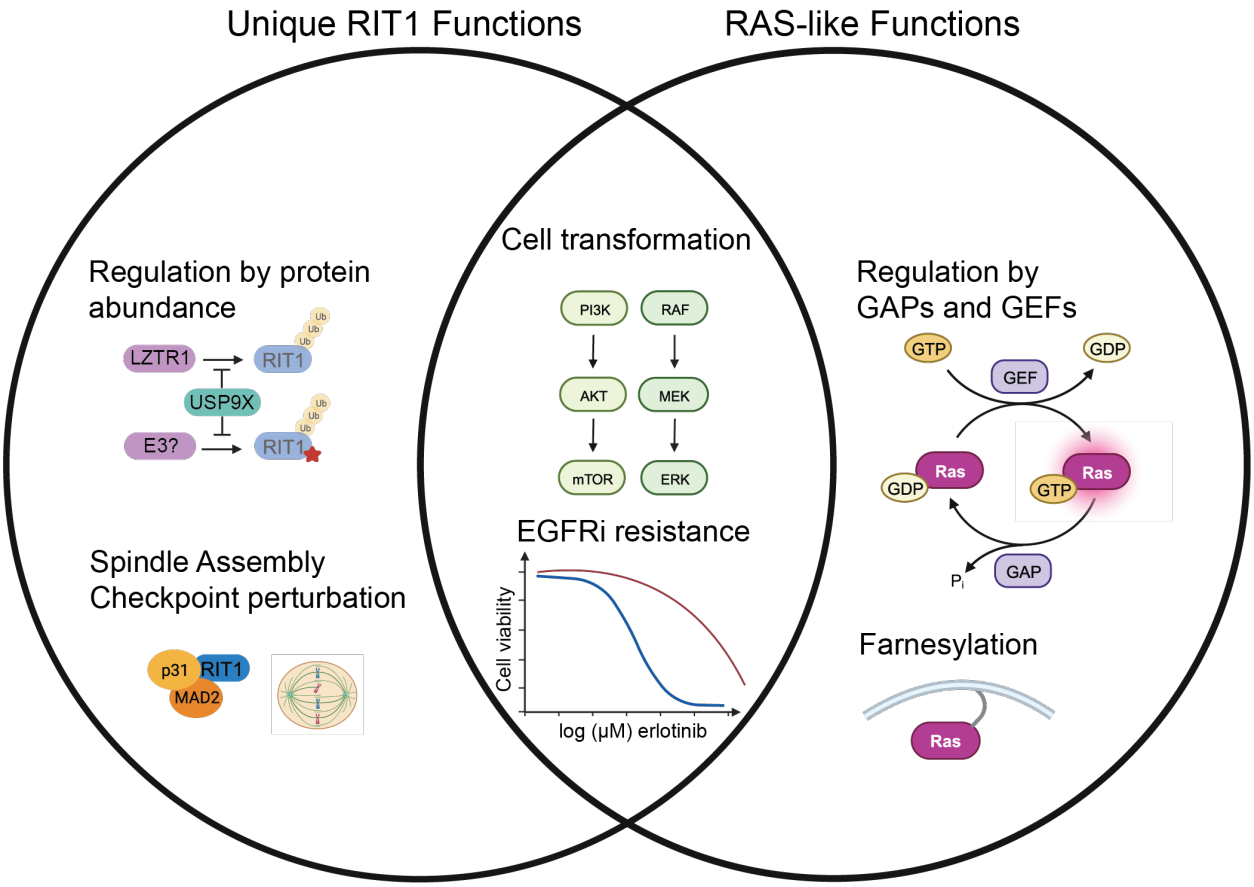

Figure 1.1. Venn diagram illustrating RIT1 functions that are similar to RAS and those that are unique to RIT1.

Figure created with Biorender.com

RIT1 shows high sequence homology to other RAS proteins such as KRAS, NRAS, and HRAS (14). Expression of mutant *RIT1* (9) and mutant *RAS* (15–17) transforms cells, primarily via activation of PI3K/MAPK signaling to promote cell proliferation (9,18–21). Furthermore, *RIT1* and *KRAS* mutants both confer resistance to EGFR tyrosine kinase inhibitors such as erlotinib and osimertinib (18,22). This suggests that RIT1 functions within the MAPK signaling pathway, but the exact role of RIT1 within this pathway appears to be cell-type and context-dependent.

In *RIT1*-mutant NCI-H2110 cells, knockdown of *RIT1* reduces phosphorylation of AKT, MEK, and ERK, thereby suggesting that RIT1 plays an important role in the PI3K and MEK pathways in these cells (9). Similarly, in HEK293T cells, expression of *RIT1* mutants increases activation of ERK1/2 (23). Expressing $RIT1^{M90I}$ in immortalized lung epithelial cells increases MEK phosphorylation in some, but not all, cell lines (9). Some groups have found that expression of mutant *RIT1* in NIH3T3 cells does not induce phosphorylation of AKT, MEK, or ERK (18,24). Interestingly, co-expression of RIT1 and RIN (a neuron-specific form of RIT1) induces colony formation in NIH3T3 cells, but the exact mechanism of this is not fully understood (8,25). Given this variability, there is a clear need to further study RIT1 and understand the context- and cell-line dependent factors that govern its function.

Similarly to RAS proteins, RIT1 binds GDP and GTP to cycle between inactive and active forms, respectively (7). In cells not stimulated with mitogenic signals, most cellular RIT1 is bound to GTP (26). This is in contrast to KRAS, which is predominantly bound to GDP in cells not stimulated with growth factors (3). High abundance of GDP-bound KRAS is mediated through the action of GAPs (GTPase-activating proteins) (3), but GAPs and GEFs (guanine nucleotide exchange factors) that regulate RIT1 have yet to be identified. RIT1 mutants have

similar or increased GTP loading compared to wild-type RIT1, but there is not a clear connection between the GTP-loaded state of RIT1 and its oncogenic function (26). This is in contrast to KRAS mutations, which tend to occur in GTP-binding regions of the protein, thereby blocking GAP activity and increasing the GTP-to-GDP ratio (3). RIT1 mutations, however, cluster in the switch II domain of the protein, which is important for protein-protein interactions (9).

Over 90% of oncogenic RAS mutations occur in "hot-spot" regions, defined at Gly^{12}, Gly^{13}, and Gln^{61} (27). These mutants confer GAP resistance, meaning that GTP hydrolysis is prevented and RAS remains in the active GTP-bound state (28,29). The RAS Q61 site is homologous to Q79 in RIT1 (7). Experimentally engineered RIT1 Q79L transforms NIH3T3 cells (30) and activates MAPK signaling (31,32). However, Q79L is not observed in patient tumors because the Q79 codon occurs at a splice site, so the mutation would disrupt the splice site (9). G12 and G13 of RAS are homologous to G30 and G31 in RIT1, but to date no G30 or G31 *RIT1* mutations have been found in cancer. Ectopic expression of G31R activates MAPK signaling in HEK293T cells, as does the G30V mutation, but to a lesser extent (23,33).

Of the currently identified *RIT1* mutations, the M90I variant ($RIT1^{M90I}$) is the most recurrent RIT1 variant in cancer (9). Instead of GAP resistance, mutant RIT1 appears to alter RIT1 regulation via dysregulation of RIT1 protein abundance (26,34,35). Wild-type RIT1 is subject to polyubiquitination and proteasomal degradation by the cullin 3 RING E3 ubiquitin ligase (CUL3) and the adaptor protein LZTR1 (leucine zipper-like transcription regulator 1) (26). Mutant forms of RIT1 evade this regulation, thereby increasing the protein abundance of RIT1 (26). Increased RIT1 protein abundance has been linked to Noonan syndrome (26) and blood cancers (34). The importance of protein abundance, as opposed to GAP resistance, appears to be a key difference in RIT1 and RAS and likely partially explains why GAPs and GEFs that

regulate RIT1 have not been identified. The link between RIT1 protein abundance and oncogenic phenotypes is further discussed in **Section 1.7.1**.

The G domain of RIT1 and RAS share 51% sequence homology, suggesting that RIT1 and RAS could interact with similar effector proteins (36). RAS family members show varying degrees of binding affinity to RASSF (RAS association domain family) proteins, which are involved in many different signaling pathways, including cytoskeleton dynamics and cell cycle progression (37,38). RASSF1 and RASSF5 show high affinity interactions with RAS, but not with RIT1 (39). Instead, RIT1 preferentially binds to RASSF7 and RASSF9 (39).

Of the currently identified RAS effector proteins, RAF kinases—and their effects on downstream signaling—have been extensively studied (40,41). At the plasma membrane, it is well-known that KRAS interacts with RAF kinases to mediate downstream signaling (42). RAF proteins (ARAF, BRAF, and CRAF/RAF1) contain a high-affinity RAS-binding domain (RBD) that is essential for interaction with RAS and activation of downstream signaling (40,41). Unlike other RAS proteins, RIT1 lacks a carboxy-terminal CAAX prenylation motif that is used by RAS for plasma membrane tethering (8). Despite this, the C-terminal hypervariable region (HVR) of RIT1 mediates plasma membrane localization through charge complementarity (8,43–46). Deletion of the C terminus–but not the N terminus–disrupts this plasma membrane interaction (44). Previous work suggested that RIT1 was unable to bind RAF proteins (7,39), but others have found that RIT1-GTP can weakly bind BRAF (26,31,47). Comprehensive characterization of RIT1 and RAF kinases revealed that RIT1 preferentially binds to CRAF (RAF1) over ARAF or BRAF (44). The C terminus of RIT1 is essential its interaction with CRAF (44).

Mutant forms of RIT1 accumulate at the plasma membrane, which promotes recruitment of RAF kinases and stimulates MAPK signaling (26,44). Pharmacological inhibition of RAF

abrogates this RIT1-driven MAPK signaling (44). Even the constitutively active $RIT1^{Q79L}$ mutant–structurally analogous to RAS^{Q61L}–is unable to activate MAPK signaling in the absence of RAF binding (44). This suggests that RIT1-RAF binding is essential for downstream mitogenic signaling. Furthermore, RIT1 is unable to activate MAPK in the absence of RAS (44). These data suggest a model whereby RIT1-RAF binding drives RAS-RAF interactions and activates RAS signaling (44). Together, these findings suggest that RIT1 and RAS signaling is highly intertwined.

The Berger Lab has employed methods to systematically compare and contrast the biology of *KRAS*-driven versus *RIT1*-driven lung adenocarcinoma in cell line models (48). Using human lung epithelial cells expressing *KRAS* and *RIT1* variants, we profiled the transcriptome, proteome, and phosphoproteome (48). As expected, *KRAS*- and *RIT1*-mutant cells exhibited increased phosphorylation of RAS/MAPK signaling effectors, including MEK and ERK (48). Overall, the global proteome in *KRAS*- and *RIT1*-mutant cells were largely similar (48). However, *KRAS*-mutant cells showed decreased phosphorylation of splicing factor proteins, whereas these proteins were largely unchanged in *RIT1*-mutant cells (49). Interestingly, over-expression of wild-type *RIT1* phenocopied mutant *RIT1*, whereas over-expression of wild-type *KRAS* was not phenotypically similar to mutant *KRAS* (48). This suggests that wild-type *RIT1* amplification and overexpression could result in a similar phenotype to mutant *RIT1* expression.

In addition to the transcriptome and proteome analyses described above, the Berger Lab has employed genomics methods to compare genetic dependencies of *RIT1*- and *KRAS*-mutant cells. Genome-wide CRISPR screening in *KRAS*- and *RIT1*-mutant isogenic lung adenocarcinoma cells revealed that *RIT1*-mutant cells–but not *KRAS*-mutant cells–are dependent on genes involved in the Spindle Assembly Checkpoint (SAC), such as Aurora kinase A

(AURKA) and Aurora kinase B (AURKB) (18). This dependency renders *RIT1*-mutant cells uniquely sensitive to Aurora kinase inhibitors (18). Many of the SAC genes were not significant dependencies in *KRAS*-mutant cells, and *KRAS*-mutant cells were not as sensitive to AURKA and AURKB inhibition (18). I was involved in analysis of the CRISPR screen data and performed experiments to explore RIT1's perturbation of mitosis and dependency on SAC genes. These efforts and my contributions are further discussed in **Section 2.2**.

In summary, RIT1 and RAS are GTPase proteins with some overlapping functions in terms of effector molecules and activation of downstream signaling pathways (**Figure 1.1**). However, the mutational landscape of RIT1 and RAS are unique and likely reflect key differences in functional outcomes. RAS is regulated at the level of GAP resistance, whereas the protein abundance of RIT1 appears to be important for its function. As we gain more knowledge about RIT1 regulation, we are uncovering new genetic vulnerabilities and nominating druggable genes for the development of targeted therapies.

1.4 Approaches to studying RIT1

Studying the role of RIT1 in cancer has become an important question, not only to understand the biology underlying *RIT1*-driven oncogenesis but also to identify better treatment options. Answering these questions, however, poses a major challenge due to the lack of cell line and mouse models. Out of all commercially available lung adenocarcinoma cell lines, only one—NCI-H2110—harbors an endogenous RIT1^{M90I} mutation (9). Because of this, innovative approaches are needed to better understand RIT1 biology and oncogenic mechanisms.

The Berger Lab developed a unique genome-wide screening approach to identify genes required for RIT1 function (18,50). This screen took advantage of the observation that expression of RIT1^{M90I} confers resistance to EGFR inhibitors in PC9 lung adenocarcinoma cells

(18,22). PC9 cells harbor an *EGFR* mutation that renders them dependent on EGFR for survival and thus sensitive to EGFR tyrosine kinase inhibitors such as erlotinib and osimertinib (51,52). In this system, the drug resistance phenotype is directed related to RIT1 function, thus facilitating the discovery of essential genes and cooperating factors in *RIT1*-mutant cells. This method is robust, but there are some notable drawbacks. *RIT1* mutations are almost always mutually exclusive with other mutations in the RTK/RAS pathway, including *EGFR* (2). Because of this, the physiological relevance of the *EGFR*-mutant PC9 system might be questioned. However, it is important to note that this PC9 system is similar to the widely used Ba/F3 model system (53). Ba/F3 cells are a mouse pro-B cell line dependent on interleukin 3 (IL-3) for survival (53). Expression of a driver oncogenic mutation—such as *EGFR*—renders Ba/F3 cells IL-3 independent (53). This system has been used since the late 1980s to understand the biology of driver genes and test sensitivity to targeted therapies (54). The Berger Lab's PC9-based system is analogous to the Ba/F3 model since expression of oncogenes renders PC9 cells resistance to EGFR inhibitors. PC9 cells, however, are a human lung cell line and thus more physiologically relevant than the mouse-based Ba/F3 system. As such, the PC9 system is a useful and valuable system for understanding RIT1 genetic dependencies.

Another challenge to studying RIT1 has been the lack of mouse models. Substantial progress was made in 2019, when a RIT1^{M90I}-mutant mouse model was generated via germline knock-in of the mutant allele (26). Heterozygous RIT1^{M90I}-mutant mice showed phenotypes resembling Noonan syndrome, including craniofacial abnormalities and increased heart weight-to-body weight ratios (26). In mouse embryonic fibroblast (MEF) cell lines established from these mice, RIT1^{M90I}-mutant cells stimulated with fetal bovine serum showed increased phosphorylation of MEK1/2 and ERK1/2, as well as increased mRNA expression of MAPK-

related transcription factors *Dusp6* and *Spry2* (26). The establishment of this mouse model provided key insight into RIT1 disease mechanisms in the context of Noonan syndrome.

In 2022, a leukemia mouse model was established to investigate the mechanisms of *LZTR1* and *RIT1* mutations in hematological malignancies (11,34,55). In embryos with complete loss of LZTR1, death occurred between embryonic day 17.5 (E17.5) and birth (34). Cells derived from E14.5 *LZTR1* knockout (KO) liver cells showed increased expression of RIT1 and RAS proteins, including KRAS (34). Upon transplantation of hematopoietic *LZTR1* KO cells into animals expressing wild-type *LZTR1*, the KO cells eventually out-competed WT cells, and animals developed hematologic malignancies, including myeloproliferative neoplasms (MPN) (34). Expression of $RIT1^{M90I}$ in hematopoietic cells phenocopies what is observed upon NRAS- and KRAS-expression, notably enhanced granulocyte-macrophage colony-stimulating factor (GM-CSF) colony formation (26,56,57). Both loss of LZTR1 and expression of $RIT1^{M90I}$ increased the proliferation of hematopoietic stem/progenitor cells (HSPC) (34). In myeloid cells derived from this mouse model, *LZTR1* deletion and $RIT1^{M90I}$ expression resulted in similar gene expression profiles and reduced expression of many tumor suppressor genes such as *EZH2* (34). After six weeks, induction of $RIT1^{M90I}$ caused MPN and other myeloid neoplasms (34). This mouse model represents the first *in vivo* model to study *RIT1*-induced transformation.

The Noonan syndrome and leukemia mouse models described above represent major advances in our understanding of RIT1 disease mechanisms *in vivo*. More models such as these are needed to understand the mechanism(s) of RIT1 in other cancer types, such as non-small cell lung cancer. There is a need to study both the effects of *RIT1* amplifications and mutations in murine models. With a lung cancer model of *RIT1*-driven cancer, we would be able to test genetic dependencies found *in vitro* and assess the efficacy of proposed targeted therapies.

1.5 RIT1 MUTATIONS IN CANCER

When *RIT1* mutations were first discovered, they were primarily studied in the context of the developmental disease Noonan syndrome (NS). In NS patients, germline *RIT1* mutations generally do not increase an individual's risk of developing cancer (58). In rare cases, juvenile myelomonocytic leukemia has been reported in patients with *RIT1*-associated NS (58). Beyond NS, most of our knowledge pertaining to *RIT1* mutations in adult cancers has come from tumor sequencing studies from the past decade.

Whole-exome sequencing of lung adenocarcinoma (LUAD) tumors in The Cancer Genome Atlas Research Network (TCGA) study revealed that *RIT1* was mutated in 2.2% of tumors (2). These alterations did not co-occur with other common LUAD driver genes such as *KRAS*, suggesting that *RIT1* itself drives oncogenesis (2). A follow-up study found that expression of mutant *RIT1* transforms cells, and injection of *RIT1*-mutant cells in mice induces tumor formation (9). This study marked the first in-depth analysis of *RIT1* as an oncogene. Since then, *RIT1* mutations have been studied in several different cancer types.

RIT1 mutations have been found in numerous types of myeloid malignancies (11,34,59). This was first discovered in a next-generation sequencing study of patients with myelodysplastic/myeloproliferative neoplasms (MDS/MPN), including chronic myelomonocytic leukemia (CMML) (11). *RIT1* mutations (predominantly at the F82 locus, but also at M90 and E81) were found in 7% of cases (11). In a retrospective sequencing study of patients with myeloid neoplasms, *RIT1* mutations were detected in approximately 15% of MDS/MPN cases (59). Treatment options for these disorders are currently very limited and primarily focused on symptom management (60).

In rare cases, *RIT1* mutations have been found in the context of resistance to tyrosine kinase inhibitors (61). In an analysis of *ALK*-positive tumors in patients that had progressed on ALK inhibitor therapy, an acquired RIT1 K139N mutation was detected in one patient (61). This mutation has not yet been characterized, and it is unclear how it may affect RIT1 activity.

In parallel with the identification of *RIT1* mutations, many studies have also observed *RIT1* amplifications (**Figure 1.2**). In a study of endometrial cancer, *RIT1* mutations (including missense mutations and in-frame mutations) were found in ~1% of cases, while *RIT1* amplifications were documented in 10% of cases (10). In the TCGA cohort, *RIT1* amplifications were found in 14% of NSCLC tumors (2). In the leukemia study described above, *RIT1* amplifications were found in 4% of cases (11). In the cohort of ALK inhibitor-resistant tumors, one sample showed increased copy number variation of *RIT1* (61). Cases of *RIT1* amplifications are not confined to these specific studies; instead, there is a growing understanding that *RIT1* copy number changes are likely oncogenic.

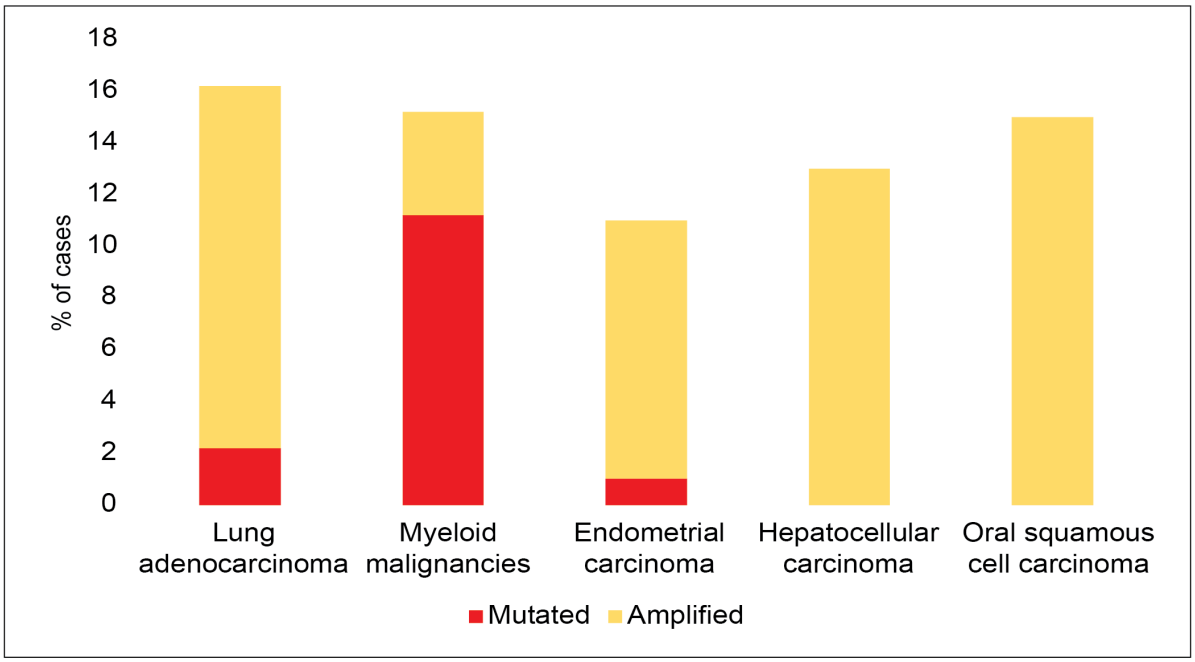

Figure 1.2. Landscape of *RIT1* alterations in cancer.
Approximate prevalence of *RIT1* mutations and amplifications across several different cancer types. Percentages are based on genome sequencing studies (2,10,11,62–64).

1.6 RIT1 AMPLIFICATIONS IN CANCER

RIT1 is overexpressed in several cancer types, including adrenocortical carcinoma, hepatocellular carcinoma, glioblastoma, and myeloid malignancies (11,62,63,65,66). Tumors with elevated *RIT1* expression show increased activation of RAS/MAPK pathway genes (62,67). In studies of hepatocellular carcinoma, copy number amplification of *RIT1* was found in 13% of patients, which is a higher frequency than any other RAS family member in this cancer type (62). Studies in patients with oral squamous cell carcinoma revealed that upregulation of *RIT1* was found in 15% of patients who smoked tobacco products (64). In cases of *RIT1* amplification, both *RIT1* mRNA and protein abundance are upregulated (10,62).

In most cases, high expression of *RIT1* is associated with poor prognosis (10,64–66,68). Overexpression of *RIT1* in glioblastoma cell lines caused increased proliferation, invasion, and colony formation compared to control groups (67). Furthermore, *RIT1* expression is associated with poor survival in lower grade gliomas (68). Subcutaneous injection of *RIT1*-depleted glioblastoma cells abrogated tumor formation in nude mice, suggesting that RIT1 is important for driving tumor growth in these cells (67). Conversely, in kidney renal clear cell carcinoma, *RIT1* expression is correlated with better overall survival (68). In esophageal squamous cell carcinoma, *RIT1* expression is associated with lower levels of MAPK signaling and better prognosis (69). To date, these two studies are the only instances of *RIT1* acting as a tumor suppressor.

In the field of RIT1 biology, we are beginning to appreciate that *RIT1* amplifications, similarly to *RIT1* mutations, are oncogenic. Global proteome and phosphoproteome analyses revealed that overexpression of $RIT1^{WT}$ and expression of $RIT1^{M90I}$ phenocopied each other in terms of down- and up-regulated proteins (48). Conversely, over-expression of wild-type *KRAS* did not phenocopy mutant *KRAS* (48). As such, this suggests that the abundance of RIT1 protein is related to unique mechanisms of RIT1 oncogenesis. The relevance and data supporting this hypothesis are further discussed in **Section 1.7.1**.

1.7 RIT1 ONCOGENIC MECHANISMS

The studies discussed above support an oncogenic role for RIT1, but the exact mechanisms that lead to transformation and tumor growth are not clear. Despite this, recurrent themes have been emerging. Note that the mechanisms discussed in this section could occur simultaneously or only in certain cellular contexts, and future work is needed to understand context-specific states.

1.7.1 *Role of protein abundance*

In 2019, evidence emerged that the protein abundance of RIT1 appeared to be crucial for its function (26). This study found that wild-type RIT1 binds to leucine zipper-like transcription regulator 1 (LZTR1), an adaptor for the cullin 3 RING E3 ligase (70). This binding promotes polyubiquitination and degradation of wild-type RIT1 through the ubiquitin-proteasome system (26). Mutations in *LZTR1* and in *RIT1*, including RIT1^{M90I}, disrupt interaction with LZTR1, thereby preventing RIT1 degradation (26). In addition to targeting RIT1, LZTR1 has been shown to bind other RAS proteins, including KRAS (71–73). However, LZTR1 preferentially binds RIT1 over other RAS proteins (35). In primary skin fibroblasts derived from children with homozygous *LZTR1* mutations and diagnosed Noonan syndrome, RIT1 protein abundance was markedly increased compared to fibroblasts with heterozygous *LZTR1* mutations (26). This was the first study to link the protein abundance of RIT1 to a disease state.

Beyond Noonan syndrome, the protein abundance of RIT1 has also been implicated in driving tumor growth. In human myeloid leukemia cells, expression of mutant *RIT1* (including the M90I variant) resulted in increased RIT1 protein abundance—via evasion of LZTR1-mediated degradation—and increased phosphorylation of MEK1/2 and ERK1/2 (34). Pathogenic levels of RIT1 are thus important for maintaining and perhaps initiating disease states. Given the prevalence of *RIT1* mutations in lung adenocarcinoma, it is also important to understand how RIT1 oncoproteins are regulated in lung cancer cells.

In analyzing data from the PC9 lung adenocarcinoma cell-based CRISPR screen, I found that the deubiquitinase *USP9X* emerged as a top genetic dependency in *RIT1*-mutant cells (18). This was an intriguing finding and suggested that RIT1 could be a substrate of USP9X. To follow up on this hypothesis, a recent preprint from the Berger Lab investigated the role of

USP9X in *RIT1*-mutant cancers (74). This study is a key component of this dissertation and is further discussed in **Chapter 3**. In brief, loss of *USP9X* abrogated proliferation and anchorage-independent growth of *RIT1*-mutant cells and resensitized these cells to EGFR inhibition (74). *USP9X* knockout reduced the abundance of both wild-type and mutant RIT1, suggesting that USP9X targets multiple forms of RIT1 (74). This work suggests that USP9X and LZTR1 are opposing the action of one another on the regulation of wild-type RIT1, while USP9X and a currently unknown E3 ligase are targeting mutant RIT1 (74). Based on these findings and the importance of protein abundance for RIT1 oncogenesis, USP9X could be a promising therapeutic target in *RIT1*-driven diseases. Future work is needed to assess the preclinical utility of USP9X inhibitors in NSCLC and other cancers characterized by *RIT1* mutations and amplifications.

1.7.2 *Perturbation of mitosis*

Although genome instability is considered to be a hallmark of cancer (75), it is not completely clear how genomic changes such as aneuploidy contribute to oncogenesis. Chromosome and whole genome duplications acquired during aberrant cell division can hinder cell growth due to accumulation of deleterious mutations; however, these mutations can also promote cell growth and oncogenic mechanisms (76–79). In the context of *RIT1*-mutant cancers, several groups have found that RIT1 perturbs mitosis (18,80,81), but the exact contribution of this to oncogenesis has yet to be elucidated.

The Berger Lab's CRISPR screen revealed that RIT1^{M90I}-mutant cells are uniquely dependent on cell cycle genes, including Aurora kinase A (*AURKA*) and Aurora kinase B (*AURKB*) (18). Genetic knockout of *AURKA* or *AURKB* in *RIT1*-mutant–but not *KRAS*-mutant–lung adenocarcinoma cells hindered proliferation and anchorage-independent growth (18).

Furthermore, *RIT1*-mutant cells were significantly more sensitive to alisertib (an AURKA inhibitor) and barasertib (an AURKB inhibitor) compared to *KRAS*-mutant cells (18). Expression of $RIT1^{M90I}$ in HeLa cells resulted in faster progression through mitosis and increased chromosomal abnormalities, suggesting that cells were bypassing the Spindle Assembly Checkpoint (SAC) (18). Based on these results, it appears as though $RIT1^{M90I}$ weakens the SAC, allowing cells to aberrantly pass through this checkpoint. Because of this, it has been hypothesized that $RIT1^{M90I}$-mutant cells are dependent on AURKA and AURKB to maintain sufficient mitotic fidelity, thereby resulting in heightened vulnerability to Aurora kinase inhibitors (18). Specific data pertaining to these results are further discussed in **Section 2.2**.

In parallel with the Berger Lab's findings, Dr. Frank McCormick's group also demonstrated that RIT1 weakens the SAC (80). Comprehensive biochemical analyses revealed that RIT1 physically interacts with MAD2 and $p31^{comet}$, components of the Spindle Assembly Checkpoint (80). During mitosis, MAD2 amplifies the signal at unattached kinetochores to promote formation of the Mitotic Checkpoint Complex (MCC) (82). The MCC inhibits the anaphase-promoting complex/cyclosome (APC/C) to prevent cells from progressing through mitosis before all chromosomes are properly aligned (83). $P31^{comet}$ promotes the removal of MAD2 from kinetochores and dissociation of the MCC (84). It is thought that this RIT1-MAD2 binding sequesters MAD2 away from its role in the MCC and accelerates progression through mitosis (80). The physical interaction of RIT1 with MAD2 and $p31^{comet}$ is not affected by the GTP-loaded state or mutational status of RIT1 (80). Importantly, these interactions are unique to RIT1 and are not observed with other RAS proteins (80).

As cells enter mitosis, RIT1 diffuses into the cytoplasm and is phosphorylated by CDK1, which prevents interaction with $p31^{comet}$ and MAD2 (80). However, when RIT1 is expressed at

pathogenic levels, CDK1 is not able to phosphorylate all RIT1 molecules present, and complexes of RIT1/MAD2/p31^{comet} are formed (80). This mechanism provides additional, important context for further understanding how the protein abundance of RIT1 contributes to its pathogenic function. This was first explored in the context of lung adenocarcinoma, but RIT1's perturbation of mitosis has also been observed in other cancer types.

In hepatocellular carcinoma (HCC) cells, RIT1 localizes to chromosomes during mitosis (81). Interestingly, in these cells, evidence for physical interaction of RIT1 and MAD2 has not been detected (81). Instead, RIT1 was found to interact with other proteins important for chromosome separation, including SMC3 (structural maintenance of chromosome 3) (81). SMC3 must be acetylated in order to ensure proper progression through mitosis (85). During mitosis, RIT1 interacts with PDS5 (precocious dissociation of sisters 5), which maintains SMC5 acetylation (81,86). RIT1's interaction with SMC3 appears to be vital to proper progression through mitosis, for *RIT1* knockdown arrests HCC cells in G2/M and causes mitotic abnormalities (81). Based on these studies, RIT1's regulation of mitosis may be context and cell-type dependent. Future work is needed to understand how RIT1 affects the cell cycle in various disease states.

Although it is not exactly clear how RIT1's perturbation of mitosis is linked to oncogenesis, it has been hypothesized that this could be related to other work pointing towards RIT1's ability to evade the cellular stress response, as discussed in **Section 1.7.3**.

1.7.3 *Oxidative stress response*

Increased oxidative stress, due to excessive reactive oxygen species (ROS), can cause cellular damage that promotes or maintains disease states (87). In response to ROS, signaling pathways can lead to cell survival or cell death (88). MEFs derived from *RIT1* knockout mice

showed increased apoptosis in response to ROS accumulation (89). Notably, treatment with a MEK/ERK inhibitor did not affect the survival of *RIT1*-mutant cells exposed to hydrogen peroxide, but these cells were potently sensitive to a p38 inhibitor (89). This suggests that the p38 cascade is important in *RIT1*-driven oxidative stress response and survival.

P38 is known to activate pro-survival signaling through numerous pathways, including via AKT (90–92). *RIT1*-driven AKT activation can occur via RIT1's interaction with mTORC2 (mammalian target of rapamycin) (93). Knockdown of mTORC2 blocks AKT phosphorylation in *RIT1*-mutant cells, rendering cells more vulnerable to ROS-induced cell death (93). Although other RAS proteins are known to signal through AKT, ROS-related RAS signaling appears to be PI3K-dependent (94,95). In contrast, RIT1-mediated AKT signaling in the stress response appears to uniquely occur through p38 (93,96). This work suggests that p38 inhibitors may be a viable treatment option for patients with *RIT1*-driven cancers, but future work is needed to understand the risks and benefits of such a treatment regimen (96).

The involvement of RIT1 in the p38 signaling cascade is not unique to human cells. In mouse hippocampal neurons, mutant *RIT1* expression improves cell survival upon exposure to hydrogen peroxide, which is consistent with what has been observed in human cell lines as discussed above (97). This group also found that p38 inhibitors, but not MEK/ERK inhibitors, promoted ROS-induced cell death in *RIT1*-mutant cells (97). Together, these results suggest that RIT1 regulates the oxidative stress response in numerous cellular contexts.

The connection between RIT1-mediated oxidative stress response and oncogenesis is not completely clear, but it may be related to the mitotic phenotypes described in **Section 1.7.2**. RIT1's ability to promote progression through the SAC (18,80) could be important for promoting cell survival, even in the presence of oxidative stress. Interestingly, Aurora kinase A can become

hyperphosphorylated and inactivated by ROS, which negatively affects spindle assembly and can cause mitotic delay (98). This suggests a model in which perhaps ROS accumulation inactivates a portion of Aurora kinase A molecules within the cell, so *RIT1*-mutant cells are more dependent on the active Aurora kinase A still present. This hypothesis, and the role of Aurora kinase B in this model, requires future experimentation.

1.7.4 *Cellular invasion & epithelial-to-mesenchymal transition*

Inducing vasculature formation is a well-known hallmark of cancer, and there is evidence that RIT1 can affect this process (75). BALB/C mice injected with *RIT1*-overexpressing liver cells showed higher density of capillaries compared to control conditions (65). Additional experiments in this HCC mouse model revealed that RIT1 was able to regulate tumor vasculature and promote metastasis through activation of VEGFA (vascular endothelial growth factor A) (62). Evidence for *RIT1*-driven regulation of vasculature has also been found in endometrial cancer, where high *RIT1* expression is associated with increased vascular invasion (10).

Analysis of the global proteome of *RIT1*-mutant cells revealed that epithelial-to-mesenchymal transition (EMT) pathway genes were the most significantly up-regulated pathways compared to parental cells (48). Both $RIT1^{WT}$- and $RIT1^{M90I}$-overexpressing lung epithelial cells showed heightened migration capacity in scratch assays (48). This is consistent with work showing that RIT1-induced MEK/ERK signaling promoted migration and outgrowth of human neuronal cells (99). In liver cancer cells, *RIT1* overexpression promoted cell migration and invasion (100). In A549 lung cancer cells, knockout of *LZTR1* promoted cell invasion, while *RIT1* knockdown suppressed invasion (101). Together, these studies suggest that increased RIT1 protein abundance is important for promoting and modulating EMT phenotypes.

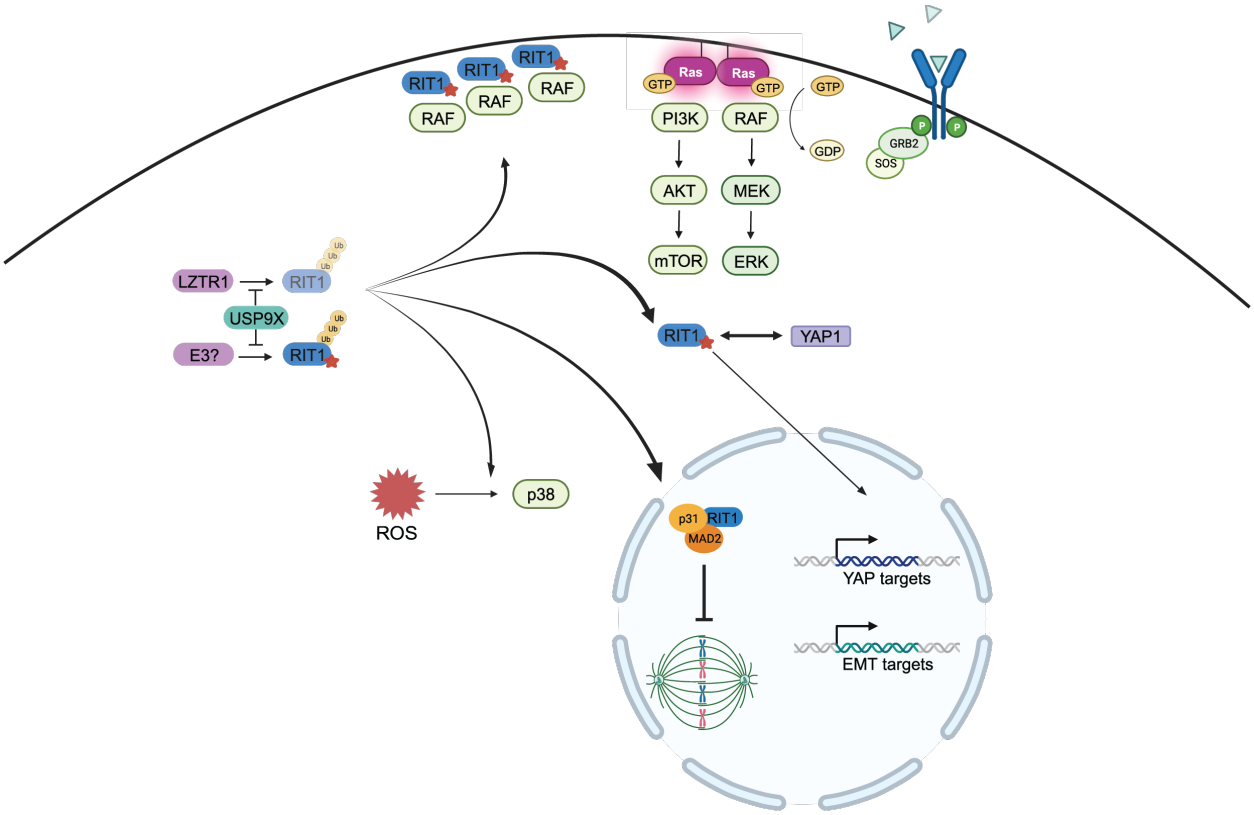

Figure 1.3. Summary of currently known and proposed RIT1 oncogenic mechanisms. Figure created with Biorender.com.

1.7.5 *RIT1/YAP synergy*

In addition to understanding genetic dependencies, the Berger Lab's CRISPR screening approach identified unique synergies in *RIT1*-driven lung adenocarcinoma cells. Most strikingly, activation of YAP1 (yes-associated protein 1) or loss of components of the Hippo signaling pathway synergized with RIT1^{M90I} to promote proliferation and xenograft tumor formation (18). Hippo signaling is a well-studied tumor suppressive pathway, but it had not previously been linked to RIT1 biology (102). Analysis of TCGA data revealed that *RIT1* alterations co-occurred with loss of at least one Hippo pathway gene in 75% of cases (18). Additionally, immunohistochemistry analysis of *YAP1* expression in patient tumors revealed that *RIT1*-mutant

tumors had significantly more nuclear-localized (i.e. activated) YAP1 (18). The mechanisms underlying this RIT1/YAP synergy is an area of ongoing research, but this holds significant promise for the potential use of YAP inhibitors for the treatment of *RIT1*-driven diseases.

1.8 ATTEMPTS TO IDENTIFY DRUGGABLE TARGETS

To date, no RIT1 inhibitors have been developed. This is due in part to the structure of RIT1, which–as a GTPase–is difficult to drug due to the lack of ATP binding pockets (103). Breakthrough developments have been made to target $KRAS^{G12C}$ via covalent reactions with the cysteine residue of G12C (104,105). Innovative approaches to directly targeting RIT1 might be possible, but a more promising and informative approach is to identify RIT1 genetic dependencies that could also serve as viable drug targets.

In cellular models of hepatocellular carcinoma, *RIT1*-expressing cells are more sensitive than *RIT1* knockout cells to the multi-kinase inhibitor sorafenib (62). This drug targets BRAF, VEGFR and other kinases in the RAS/RTK pathway (106). Sorafenib treatment suppressed ERK activation in *RIT1*-mutant cells; however, AKT levels were not affected (62). Given that RIT1 induces AKT activation in multiple different cellular contexts, the combination of sorafenib with the AKT inhibitor MK226 was tested in HCC mouse models (62). In this model, the combination treatment resulted in almost complete abrogation of tumor burden (62).

These findings in HCC are consistent with other attempts to block *RIT1*-driven oncogenesis via targeting RAS/MAPK pathway members. In PC6 pheochromocytoma cells expressing mutant *RIT1*, phosphorylation of MEK, ERK, and AKT were higher relative to control cells (9). Treating these cells with the MEK inhibitor PD98059 or the PI3K/mTOR inhibitor LY294002 reduced ERK and AKT phosphorylation, respectively (9). These findings are consistent with results in *RIT1*-mutant NCI-H2110 cells: knockdown of *RIT1* reduced MEK,

ERK, and AKT phosphorylation (9). In mice injected with NCI-H2110 cells, treatment with the PI3K/mTOR inhibitor GDC-0941 significantly reduced tumor growth (9). This work suggests that inhibition of PI3K and MEK could be viable treatment options for *RIT1*-driven lung cancer.

Another approach to treating *RIT1*-driven diseases could focus on decreasing the protein abundance of RIT1. In NSCLC, *USP9X* knockout reduces the abundance of wild-type and mutant RIT1 (74), suggesting that USP9X inhibitors could be effective in treating diseases characterized by *RIT1* amplifications and mutations. This is further discussed in **Chapter 3**.

1.9 WHERE DO WE GO FROM HERE?

In the past five years, our knowledge of RIT1 biology and oncogenic mechanisms has greatly expanded. While initially *RIT1* alterations were studied in the context of the developmental disease Noonan syndrome, we now understand that *RIT1* mutations and amplifications underlie many different cancer types. We have begun to uncover the molecular mechanisms that contribute to RIT1 oncogenesis, and this remains an area of important and active research.

The Berger Lab's genome-wide CRISPR screen in PC9 lung adenocarcinoma cells provided key insight pertaining to RIT1 genetic dependencies. This screen revealed that *RIT1*-mutant cells are uniquely dependent on components of the Spindle Assembly Checkpoint (SAC). Other groups have independently demonstrated that RIT1 weakens the SAC, but it is currently not clear if this is a side-effect or a direct mechanism of RIT1 oncogenesis. Furthermore, although Aurora kinase inhibitors are available, none are currently approved for cancer treatment. As such, RIT1's mitotic perturbation is an intriguing mechanism of RIT1 biology but may not represent the most promising avenue for targeted therapies.

There is a growing understanding that disrupting the protein abundance of RIT1 may be a means of abrogating tumor growth. Several groups have published work to support the hypothesis that the protein abundance of RIT1 is important for its function. One of the current hypotheses is that mutant RIT1 accumulates at the plasma membrane and recruits RAF kinases, which then activates RAS proteins in the vicinity and activates downstream MAPK signaling. This is an intriguing model, and future work is required to understand if this mechanism is occurring across different cell types and cancer contexts.

The model of *RIT1*-driven oncogenesis is gradually being filled in, and pieces are coming together. Despite this progress, there is a need to understand how these oncogenic mechanisms intersect or are unique across cancer types. Evidence suggests that RIT1 weakens the SAC, synergizes with YAP, and promotes EMT. Are these mechanisms happening concurrently, and are some or all of them facilitated by increased RIT1 protein abundance? Does mutant RIT1 and over-expression of wild-type RIT1 activate these pathways? My thesis work has provided key insight into understanding the protein-level regulation of both wild-type and mutant RIT1, as well as implications for future treatment options.

In Chapter 2, I further discuss the Berger Lab's CRISPR screening system in PC9 lung adenocarcinoma cells and present data I generated to explore the mechanism of RIT1's mitotic perturbation. I also present the finding of USP9X as a genetic dependency in *RIT1*-mutant cells. In Chapter 3, I share my work demonstrating that wild-type and mutant RIT1 are substrates of the deubiquitinase USP9X. Overall, this work identifies USP9X as a novel regulator of RIT1 protein abundance and reveals USP9X as a potential druggable target in diseases characterized by *RIT1* mutations and amplifications. This work can inspire future studies on USP9X inhibitors to address the major unmet clinical need for targeted therapies in *RIT1*-driven cancers.

Chapter 2. IDENTIFICATION OF RIT1 GENETIC DEPENDENCIES

A version of this chapter has been published based on content in the following peer-reviewed manuscripts:

Riley, A. K. & Berger, A. H. (2021). Genome-wide CRISPR screening reveals novel therapeutic targets in RIT1-driven lung cancer. *Mol Cell Oncol,* 8(6). http://doi.org/10.1080/23723556.2021.2000318

I wrote the manuscript cited above and generated all associated figures.

Vichas, A., Riley, A. K., Nkinsi, N. T., Kamlapurkar, S., Parrish, P. C. R., Lo, A., Duke, F., Chen J., Fung, I., Watson, J., Rees, M., Gabel, A. M., Thomas, J. D., Bradley, R. K., Lee, J. K., Hatch, E. M., Baine, M. K., Rekhtman, N., Ladanyi, M., Piccioni, F., & Berger, A. H. (2021). Integrative oncogene-dependency mapping identifies RIT1 vulnerabilities and synergies in lung cancer. *Nat Comm* 12(4789). https://doi.org/10.1038/s41467-021-24841-y

For the manuscript cited above, I performed mitotic timing assays, contributed methods, and helped with revision experiments. I assembled the final revised manuscript for re-submission. Portions of this manuscript are presented in **Section 2.2**.

2.1 PC9 SYSTEM FOR UNCOVERING RIT1 ESSENTIAL GENES

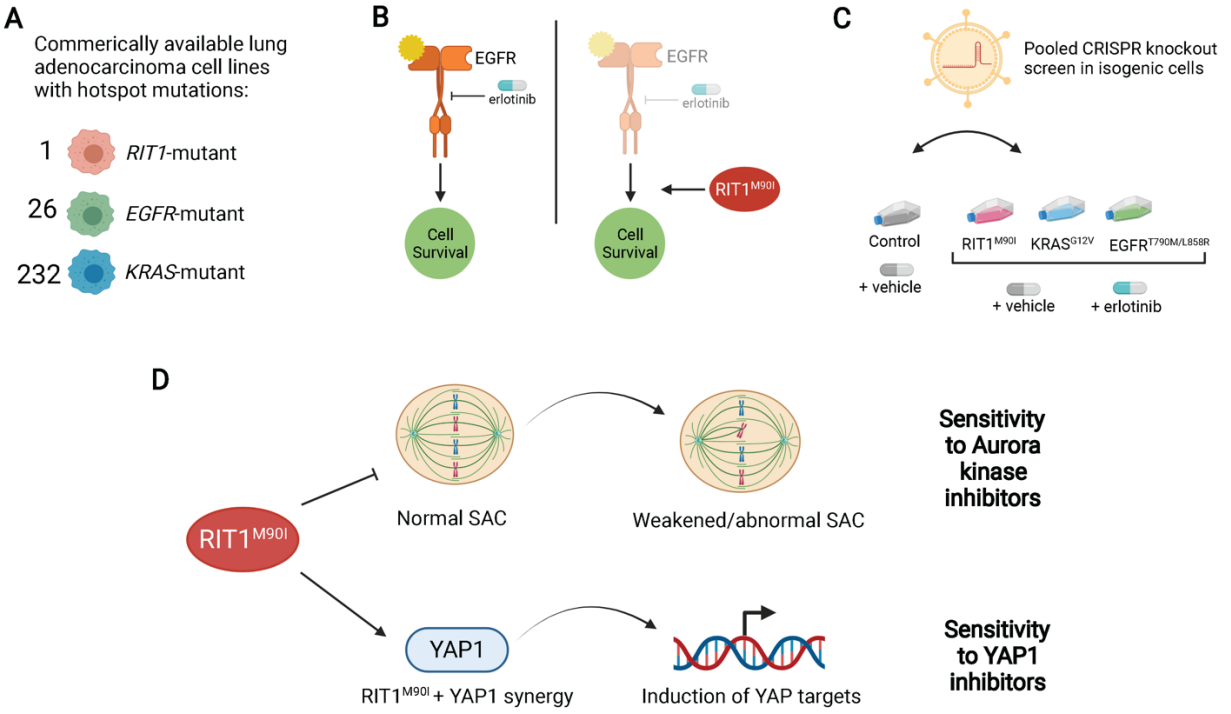

Figure 2.1. Isogenic CRISPR screening identifies genetic vulnerabilities in *RIT1*-driven lung cancer.

A) Only one *RIT1(Ras-like in all tissues)*-mutant lung cancer cell line is commercially available, thereby making *RIT1* mutations difficult to study. Cell line numbers obtained from the Dependency Map (DepMap) portal.

B) Left, in PC9 lung adenocarcinoma cells, a mutation in *EGFR* (epidermal growth factor receptor) renders cells sensitive to the EGFR inhibitor erlotinib. Right, expression of $RIT1^{M90I}$ in PC9 cells confers erlotinib resistance and restores cell survival.

C) This erlotinib resistance phenotype was used to perform CRISPR/Cas9 screens in isogenic PC9 cells expressing lung cancer driver oncogenes, including $RIT1^{M90I}$.

D) From these CRISPR screens, we found that $RIT1^{M90I}$ weakens the Spindle Assembly Checkpoint (SAC), rendering cells vulnerable to inhibitors of SAC components such as the Aurora kinases. We also found that $RIT1^{M90I}$ synergizes with YAP1 (yes-associated protein 1) to induce transcription of YAP1 targets, suggesting that YAP1 inhibitors should be investigated for the treatment of diseases caused by mutation of *RIT1*. Figure created with Biorender.com.

As introduced in **Section 1.4**, the Berger Lab implemented a unique CRISPR-screening approach to assess genetic dependencies and synergies in *RIT1*-mutant lung cancer. We performed genome-wide CRISPR/Cas9 knockout screens in PC9 lung adenocarcinoma cells stably expressing a lung cancer oncogene ($RIT1^{M90I}$, $KRAS^{G12V}$, or $EGFR^{T790M/L858R}$) (18). These screens took advantage of the observation that each introduced oncogene confers resistance to EGFR inhibition (**Figure 2.1B-C**) (9,18,22). We used this drug resistance phenotype to probe the requirements for oncogene-driven survival. We computationally analyzed the screen data to identify genetic dependencies (genes that, when knocked out, confer a growth disadvantage) and cooperating factors (genes that, when knocked out, confer a growth advantage). We found that *RIT1*-mutant cells were more dependent than *KRAS*-mutant cells on several genes implicated in the Spindle Assembly Checkpoint (SAC) (18). To further investigate this, we conducted experiments to investigate the effects of $RIT1^{M90I}$ on mitotic progression and SAC integrity.

2.2 Spindle Assembly Checkpoint (SAC) vulnerability

Altering the SAC in normal cells accelerates mitotic timing (107), and in conditions of mitotic stress can either promote mitotic cell death or result in mitotic slippage (the exit from mitosis before proper chromosome alignment is complete) (108). Given that many of the *RIT1* dependencies identified in the CRISPR screen were components of the SAC, we hypothesized that $RIT1^{M90I}$ might weaken the SAC, enhancing the vulnerability of the cells to further loss of SAC activity. To test this hypothesis, we adapted a model system commonly used for mitotic timing experiments (109): HeLa cells expressing a nuclear H2B-GFP fusion protein (110) (**Figure 2.2a**). We used live cell fluorescence microscopy to time the duration of mitosis from nuclear envelope breakdown (NEBD) to anaphase onset (107) (**Figure 2.2b**). In parental H2B-GFP cells the median duration of mitosis was 70.5 min (95% CI= 63 – 82 min), while in

RIT1^{M90I}-mutant cells the median duration of mitosis was reduced to 48 min (95% CI=45 – 51 min) (**Figure 2.2c,d**). Overall mitotic index was unaffected, suggesting that mitotic entry is not regulated by RIT1^{M90I} (**Figure 2.2e**). The difference in mitotic timing between RIT1^{M90I}-mutant cells and parental cells was eliminated by treatment with reversine, an inhibitor of the MPS1 kinase involved in establishing the SAC kinetochore signal (111), demonstrating that RIT1^{M90I} perturbs mitotic timing at the level of the SAC (**Figure 2.2c,d**). A weakened SAC has been associated with mitotic errors including misaligned chromosomes, chromosome bridges, micronuclei formation, and aneuploidy (112–115). Consistent with RIT1^{M90I} suppression of the SAC, *RIT1*-mutant cells showed significantly higher prevalence of chromosomal abnormalities compared to parental cells (**Figure 2.2f,g**).

The vulnerability of *RIT1*-mutant cells to Aurora kinase A inhibition and RIT1's ability to weaken the SAC led us to hypothesize that Aurora kinase A inhibition may be able to overcome the mitotic phenotype induced by RIT1^{M90I}. To test this hypothesis, we performed mitotic timing analysis in HeLa H2B-GFP cells treated with the Aurora kinase A inhibitor alisertib. Whereas RIT1^{M90I} alone accelerated mitosis compared to parental cells, mitotic timing in RIT1^{M90I} cells was increased compared to parental cells in the setting of alisertib (**Figure 2.2h**). RIT1^{M90I}-mutant cells accumulated more mitotic errors than parental cells in alisertib (**Figure 2.1f**). Taken together, these data indicate that oncogenic RIT1 weakens the SAC, creating a vulnerability to Aurora kinase inhibitors. Because Aurora kinases are required for full activation of the SAC (116–118), we propose a working model by which combined RIT1^{M90I} and Aurora kinase A inhibition leads to cellular toxicity and cell death (**Figure 2.2i**).

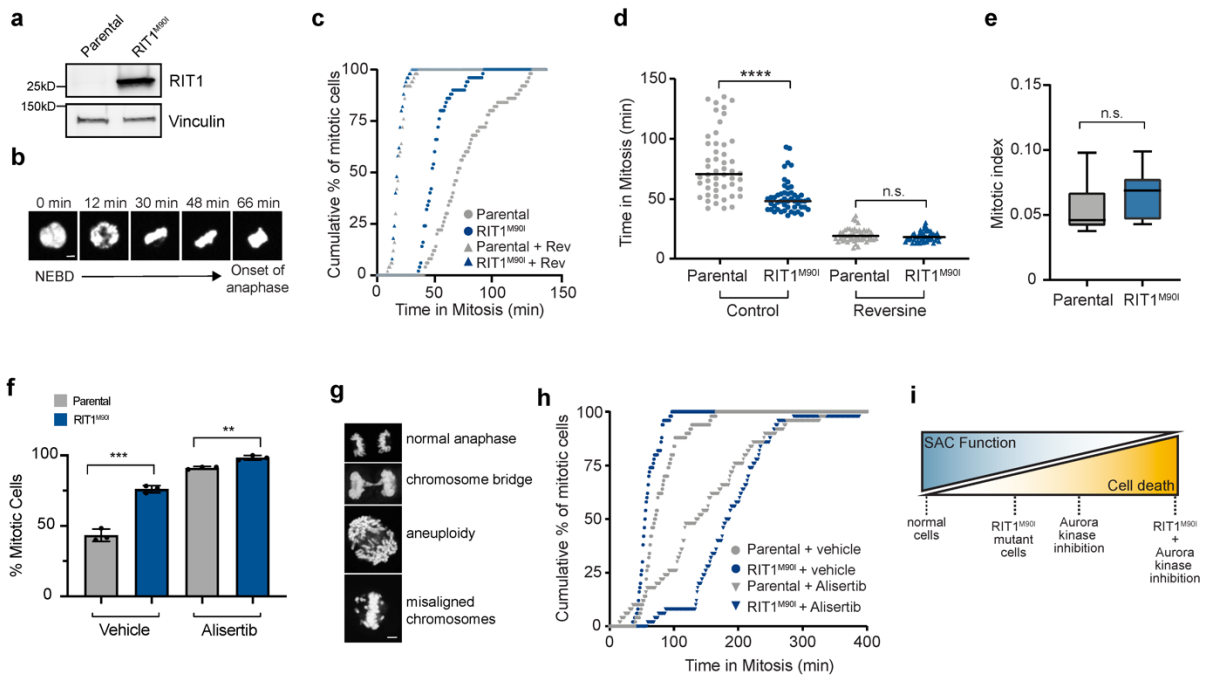

Figure 2.2. RIT1^{M90I} weakens the spindle assembly checkpoint.

a) Western blot of RIT1 expression in parental and RIT1^{M90I}-expressing HeLa H2B-GFP cells. Vinculin was used as a loading control.

b) Duration of mitosis was measured as time from nuclear envelope breakdown (NEBD) to the onset of anaphase. Each frame represents movie stills from time-lapse live-cell imaging of parental HeLa H2B-GFP cells undergoing mitosis, scale bar = 5µm.

c) Time-lapse fluorescence microscopy of time in mitosis in asynchronous parental and RIT1^{M90I}-expressing HeLa H2B-GFP cells in normal media conditions (control) or treated with 0.5 µM reversine (Rev) two hours before imaging. n = 50 cells per condition. Mitotic timing was measured from time of NEBD to anaphase onset.

d) Alternative representation of data from (c). Data shown is the mean and individual data points of each condition. ****p = 9.06e^{-9}, n.s., p = 0.1754 by unpaired two-tailed t-test.

e) Mitotic index calculated as the percentage of mitotic cells in a frame at a chosen time point. Box plots show the median (center line), first and third quartiles (box edges), and the min and max range (whiskers). n = 2 biological replicates, 6 time points per condition, n.s., p = 0.3587 by unpaired two-tailed t-test.

f) Comparison of mitotic error rates in HeLa H2B-GFP cells expressing RIT1^{M90I} compared to parental HeLa H2B-GFP cells in vehicle (DMSO)-treated and alisertib-treated (1 µM) conditions. n = 3 biological replicates, error bars indicate s.d., ***p = 0.0004, **p = 0.0029 by unpaired two-tailed t-test.

g) Representative images of mitotic errors from HeLa cells expressing RIT1^{M90I} and quantified in (f), scale bar = 5µm.

h) Time-lapse fluorescence microscopy of time in mitosis in asynchronous parental and RIT1^{M90I}-expressing HeLa H2B-GFP cells in normal media conditions (control) or treated with 1 μM alisertib two hours before imaging. n = 50 cells per condition.

i) Proposed model explaining enhanced efficacy of Aurora kinase inhibitors in RIT1^{M90I}-mutant cells.

2.3 MATERIALS AND METHODS

2.3.1 *Genome-wide CRISPR knockout screen*

The human CRISPR Brunello lentiviral pool was obtained from the Broad Institute Genetic Perturbation Platform and is also available from Addgene (73179-LV). The library contains 76,441 sgRNAs targeting 19,114 protein-coding genes and 1,000 non-targeting control sgRNAs. For genome-wide CRISPR screening, 320 million PC9-Cas9-Luciferase, PC9-Cas9-RIT1^{M90I}, PC9-Cas9-KRAS^{G12V}, or PC9-Cas9-EGFR$^{T790M/L858R}$ cells were infected with the Brunello Library lentivirus (119) at a low MOI (<0.3). At 24 h after infection, the medium was replaced with fresh media containing 1 μg/mL puromycin (Sigma). After selection on day 7, cells were split into 2 replicates containing 40 million cells each and treated with either DMSO (Sigma-Aldrich) or 40 nM erlotinib (Selleckchem). Cells were then passaged every 3 days and maintained at 500-fold coverage. For early time point analysis (day 7) an initial pool of 60 million cells was harvested for genomic DNA extraction from each of the cell lines. After ~12 doublings, a final pool of 60 million cells was harvested in ice-cold PBS and stored at -80°.

Genomic DNA was extracted using the QIAamp DNA Blood Maxi Kit (QIAGEN) and the sgRNAs from each sample were PCR amplified by dividing gDNA into multiple 100 μl reactions containing a maximum of 10 μg gDNA (as recommended by Broad Institute standard protocols). Per 96-well plate, a master mix consisted of 150 μl ExTaq polymerase (Takara Bio), 1,000 μl of 10x ExTaq buffer (Takara Bio), 800 μl of dNTP (Takara Bio), 50 μl of P5 primer

(stock at 100 µM concentration), and 2,075 µl water. Each well consisted of 50 µl gDNA plus water, 40 µl PCR master mix, and 10 µl of P7 primer (stock at 5 µM concentration). PCR cycling conditions: an initial 5 min at 95 °C; followed by 30 s at 95 °C, 30 s at 53 °C, 20 s at 72 °C, for 28 cycles; and a final 10 min extension at 72 °C. PCR samples were purified with Agencourt AMPure XP SPRI beads (Beckman Coulter). Samples were sequenced on a HiSeq 2500 (Illumina). Raw FASTQ files were demultiplexed and sgRNA counts were calculated using PoolQ v2.2.0.

2.3.2 *Mitotic timing and chromosomal aberration analysis*

RIT1^{M90I}-expressing HeLa H2B-GFP cells were generated by transduction with a pLX303-RIT1^{M90I} lentivirus and selection with puromycin. Protein expression was confirmed by Western blotting. One day before imaging, cells were seeded at a density of 30,000 cells per well of an 8-well Ibidi glass-bottomed plate. For drug-treated populations, 0.5 µM Reversine (Selleckchem) was added two hours before imaging. Live-cell imaging was performed using a 20×/0.70 Plan Apo Leica objective on an automated Leica DMi8 microscope outfitted with an Andor CSU spinning disk unit equipped with Borealis illumination, an ASI automated stage with Piezo Z-axis top plate, and an Okolab controlled environment chamber (humidified at 37°C with 5% CO2). Long term automated imaging was driven by MetaMorph software (v7.10.0.119). Images were captured with an Andor iXon Ultra 888 EMCCD camera. Images were captured every minute for 18 hours. Time in mitosis was measured as time from nuclear envelope breakdown to the onset of anaphase. Imaging experiment was repeated four times with distinct biological replicates and 50 cells were analyzed per cell line per condition.

Mitotic index was calculated from one time point selected from live-imaging experiments in HeLa H2B-GFP parental and HeLa H2B-GFP-RIT1^{M90I} cells described above. At each time-point, three independent, representative images were collected and the mitotic index was calculated based on the number of cells undergoing mitosis (in any phase between prometaphase to telophase) divided by the total number of cells. The same time point was analyzed in two independent experiments for a total of six total mitotic index analyses per cell line.

For the mitotic abnormality analysis, HeLa H2B-GFP cells were plated in a 4-well Nunc^{TM} Lab-Tek^{TM}chamber slide (ThermoFisher Scientific) at a density of 80,000 cells per well. The next day, cells were treated with either DMSO vehicle or 1 μM alisertib for 6 hours prior to being washed with 1X PBS and fixed with 4% paraformaldehyde (from 16% paraformaldehyde [wt/vol]) in 1X PBS for 30 minutes at RT. Coverslips were mounted with Vectashield antifade mounting medium with 1.5 μg/mL DAPI (Vector Laboratories). Slides were analyzed using a 40x/1.25 Oil PL Apo Leica objective on a Leica DMi8 outfitted with a TCS SPE scan head with spectral detection. Cells were visualized using the LAS X software platform (v3.5.7.23225). Representative images were captured using a 40×/1.30 Plan Apo Leica objective on a Leica DMi8 outfitted with a TCS SPE scan head with spectral detection. Images were acquired using the LAS X software platform (v3.5.5.19976). Images were corrected for brightness and contrast using FIJI (v2.1.0/1.53c). Images are single sections. For each biological replicate, 60 cells were analyzed per cell line. The prevalence of chromosome bridges, lagging and chromosome misalignment, micronuclei, aneuploidy (i.e. notable, unequal separation of chromosomes), polyploidy (i.e. evidence of unsuccessful cytokinesis) and normal separation of chromosomes were recorded.

2.1 ACKNOWLEDGMENTS

The mitotic timing analysis was included as part of a larger published manuscript (18). I completed the experiments presented in **Figure 2.2**. I would like to thank all the co-authors on this paper, particularly Dr. Athea Vichas who completed many of the other experiments for this manuscript. All the authors and I thank Amy Goodale (Broad Institute) for technical assistance in the design and synthesis of the targeted validation screening library and Dr. Daphne Avgousti (Fred Hutchinson Cancer Center) for providing HeLa H2B-GFP cells. We thank the Broad Institute Genetic Perturbation Platform for technical assistance and advice and the Fred Hutch Genomics Shared Resource and Comparative Medicine Shared Resource (supported by NIH/NCI Cancer Center Support Grant P30 CA015704) and the Northwest Genomics Center. We thank the Fred Hutch Cellular Imaging Shared Resource (supported by the Fred Hutch/University of Washington Cancer Consortium P30 CA015704) for assistance with microscopy and image analysis.

2.1.1 *Funding*

This research was funded in part through NCI R00CA197762 and R37CA252050 to A.H.B, donations from the Smith family to A.H.B., NIH/NCI Cancer Center Support Grant P30 CA015704 New Investigator support to A.H.B., a Lung Cancer Research Foundation Research Grant to A.V., and the Hutch United postdoctoral fellowship to A.V. A.R. was supported in part by PHS NRSA T32GM007270 from NIGMS. P.C.R.P. was supported in part by NSF DGE-1762114 and E.M.H was supported by NIGMS grant R35GM124766.

2.1.2 *Author contributions*

A.H.B. conceived of the project. A.H.B., R.K.B., E.M.H., and M.L. supervised the project. A.V., F.P., E.M.H., M.L., and A.H.B. designed experiments. A.V., N.T.N., A.K.R., P.C.R.P., A.L., M.K.B., A.G., and A.H.B. analyzed the data. A.V., N.N., A.K.R., P.C.R.P., S.K., I.F., J.D.T., J.K.L., F.D., J.C., J.W., M.R., N.R., M.K.B., A.G., J.D.T and A.H.B. conducted experiments. A.V. and A.H.B. wrote the manuscript. All the authors critically reviewed the manuscript and approved the final version.

2.1.3 *Competing interests*

F.P. is a current employee of Merck Research Laboratories and A.V. is a current employee of Bristol Myers Squibb. All other authors declare no competing interests.

2.2 CONCLUSION

The Berger Lab's genome-wide CRISPR/Cas9 screen revealed novel mechanisms of *RIT1*-driven cell survival. Beyond classic RTK-RAS signaling components, we uncovered a surprising vulnerability of *RIT1*-mutant cells to perturbation of mitotic regulators, particularly components of the spindle assembly checkpoint. We found that *RIT1*-mutant cells showed heightened sensitivity to loss of mitotic regulators such as *AURKA, USP9X, MAD2L1BP,* and *PLK1*, whether by genetic inactivation or small molecule inhibition, despite no differences in cell proliferation or mitotic index. We showed that RIT1^{M90I} weakens the spindle assembly checkpoint, leaving cells vulnerable to Aurora kinase inhibitors. When our manuscript was published, another group published work showing discovery of RIT1 as a MAD2-binding protein that inhibits the mitotic checkpoint complex to accelerate mitotic timing (80). Using a similar mitotic timing assay, they showed that oncogenic RIT1^{M90I} accelerates mitosis in U2-OS and

HeLa cells (80). One difference was that the assay was performed in nocodazole; otherwise the result is nearly identical to the data we show in HeLa cells, suggesting that regulation of mitotic timing and induction of mitotic errors are a general function of oncogenic RIT1. They also showed that wild-type RIT1 participates in the spindle assembly checkpoint and that knockout of endogenous *RIT1* extends mitotic timing in multiple cell types. Therefore, RIT1 normally participates in the spindle assembly checkpoint and pathogenic levels of $RIT1^{M90I}$ alter this normal regulation. The results of our study further imply that this mitotic phenotype confers a targetable vulnerability to *RIT1*-mutant cells. Future genotype-directed clinical trials could determine if patients with *RIT1*-mutant tumors would uniquely benefit from treatment with Aurora kinase inhibitors or other modulators of mitosis. Interestingly, Aurora A activation has been found to drive resistance to the third-generation EGFR inhibitor osimertinib (120). It is possible that $RIT1^{M90I}$ is harnessing this same mechanism to drive erlotinib resistance and cellular transformation.

2.3 Exploring the hypothesis of USP9X-mediated RIT1 regulation

Upon publication of the CRISPR screen and SAC vulnerability data, the question of USP9X's role in *RIT1*-mutant cells remained. When we first identified USP9X in the CRISPR screen, we classified it as a mitotic regulator given that USP9X is known to strengthen the SAC by stabilizing CDC20 (118). CDC20 is a component of the MCC (mitotic checkpoint complex), which is formed when chromosomes are not properly aligned during metaphase (121,122). The MCC inhibits the APC/C (anaphase-promoting complex/cyclosome) until proper chromosome alignment is achieved (121,122). In human osteosarcoma U2-OS cells, loss of *USP9X* accelerates progression through mitosis and increases the abundance of chromosomal abnormalities (118). In this way, USP9X protects cells against excessive chromosomal

instability. Because of this, it is possible that loss of *USP9X* in *RIT1*-mutant cells has a similar effect as loss of Aurora kinase A and Aurora kinase B, i.e. accumulation of chromosomal abnormalities (**Figure 2.1f**). This may contribute to cell death given that RIT1 is already weakening the SAC and promoting the accumulation of chromosome errors (**Figure 2.2f,g,i**). This hypothesis remains to be explored. In the scope of this thesis work, given that new evidence was emerging to link the protein abundance of RIT1 to its function, the decision was made to explore the hypothesis that RIT1 is a direct substrate of USP9X. This is not in contradiction to the findings that USP9X and RIT1 function at the SAC, but it is not clear if these are overlapping or independent functions. This is further discussed in **Chapter 4.**

Chapter 3. RIT1 IS A SUBSTRATE OF THE DEUBIQUITINASE USP9X

A version of this chapter is under peer review at iScience. A pre-print is available on bioRxiv:

Riley, A. K., Grant, M., Snell A., Vichas A., Moorthi S., Urisman, A., Castel P., Wan., L., & Berger, A. H. The deubiquitinase USP9X regulates RIT1 protein abundance and oncogenic phenotypes. (2023). https://doi.org/10.1101/2023.11.30.569313

3.1 OVERVIEW OF THE UBIQUITIN-PROTEASOME SYSTEM

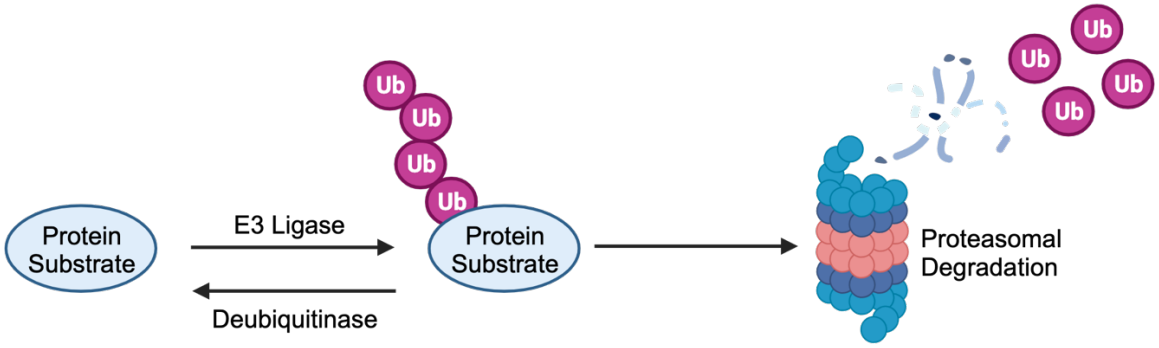

Figure 3.1. Schematic of protein degradation mediated by E3 ligases and deubiquitinases in the ubiquitin-proteasome system.
Image created with Biorender.com.

The ubiquitin-proteasome system is a well-characterized cellular process involved in regulating the intracellular abundance of protein substrates (**Figure 3.1**) (123). This system is composed of many important cellular players, including E3 ubiquitin ligases and deubiquitinases (DUBs) (123). E3 ligases catalyze the addition of ubiquitin molecules to proteins, primarily at lysine residues (124). This reaction can lead to mono-ubiquitination or poly-ubiquitination through a diverse range of ubiquitin linkages (124). Ubiquitin linkages dictate the fate of the protein substrate, with branched K48 and K11 chains associated with proteasomal degradation (124).

E3 ligases are protein complexes that can be classified into four main groups: HECT (homologous to the E6AP carboxyl terminus), RING (really interesting new gene), U-box, and RBR (RING-IBR-RING) (125). These groups are characterized based on different substrate types and structures (125). The RING E3 ligases are the largest group, and cullin-RING ligases (CRLs) are a unique subtype of RING E3 ligases that incorporate a Cullin subunit (126). CRL3 incorporates Cul3, which is known to associate with substrate-specific adaptors that contain BTB (Bric-a-brac, Tramtrack, and Broad complex) domains (126). LZTR1—the negative regulator of $RIT1^{M90I}$ discussed in **Section 1.7.1**—is a BTB-containing protein and a substrate adaptor for CRL3 (CRL^{LZTR1}) (26).

Unlike E3 ligases, DUBs do not function within a larger protein complex. Hundreds of deubiquitinase enzymes exist in human cells and there are five main DUB families: USPs (ubiquitin-specific proteases), OTUs (ovarian tumor proteases), UCHs (ubiquitin C-terminal hydrolases), Josephin, and MINDYs (motif interacting with ubiquitin-containing) (127). These families are distinguished from one another based on varying degrees of specificity for cleaving ubiquitin linkages (127). Most DUB enzymes contain a catalytic triad composed of Cystine-Histidine-Aspartic acid/Asparagine (128). USP9X is a member of the USP family and is highly conserved across evolution (129).

3.2 Mechanisms and biology of USP9X

USP9X–first discovered in fruit flies (*Drosophila melanogaster*) as the *fat facets* gene–is essential for embryogenesis in flies and mice (*Mus musculus)* (130,131). *USP9X* can replace *fat facets* during fly development (130) and shares 44% identity and 88% similarity to the fruit fly gene (132). Although USP9X's catalytic domain is consistent with DUBs in yeast, *fat facets* is the earliest *USP9X* ortholog characterized (133). From flies to mammals, *USP9X* is highly

constrained across evolution (129). Of note, orthologs of *RIT1* and *LZTR1* have been documented in fruit flies but not in less complex lab models such as *Caenorhabditis elegans* (35). This is in contrast to *KRAS*, which is highly conserved in yeast (35). Given this, it is possible that a regulatory network involving *USP9X*, *RIT1*, and *LZTR1* arose in flies and has been conserved in other more complex animals, including mammals. Rigorous evolutionary analysis is required to support this hypothesis.

Although it was initially characterized in the context of development (134,135), USP9X has been implicated in apoptosis (136–138), protein trafficking (139–142), and polarity (143–145). USP9X has been found across a wide range of cellular compartments, including the cytoplasm (142), nucleus (146,147), and mitochondria (138). This diversity highlights that USP9X function is largely dictated by cell type. As a deubiquitinase, USP9X positively maintains the abundance of proteins by removing polyubiquitin chains and preventing proteasomal degradation (138,148,149). USP9X is known to remove polyubiquitin (138,150–152) and monoubiquitin (139,153) chains. Despite these diverse functions, structural analysis of USP9X suggests that the catalytic domain preferentially binds to and cleaves polyubiquitin chains with K48- and K11-linkages (150).

In the context of cancer, *USP9X* can be upregulated or downregulated, depending on the target substrates (133). In lung adenocarcinoma, *USP9X* has been found amplified (2,154), deleted (2,154), and mutated (154–158). The exact consequences of these alterations have yet to be fully elucidated. In NSCLC, *USP9X* has been characterized as an oncogene (159–161), and high *USP9X* expression is associated with poorer overall survival (162).

Outside of cancer, *USP9X* mutations underlie X-linked developmental disability (XID) (163,164). In the neurons of individuals afflicted with XID, *USP9X* knockout causes cytoskeletal

disruptions that hinder cell growth and migration (163). RIT1 is known to regulate neuronal growth and survival (36) and can also affect actin dynamics in fibroblast-like cells via regulation of p21-activated kinase (PAK1) (23). It is possible that USP9X-mediated regulation of RIT1 is important in the context of XID, but this requires further experimentation. These findings, in combination with the observation that USP9X can cleave a diverse range of ubiquitin linkages (150), suggest that cellular context is important for determining key USP9X substrates and potential relevance in disease states.

3.3 USP9X IS AN ESSENTIAL GENE IN *RIT1*-MUTANT CELLS

In prior work, we identified genes required for $RIT1^{M90I}$ to promote resistance to the EGFR tyrosine kinase inhibitor (TKI) erlotinib in *EGFR*-mutant PC9 lung adenocarcinoma cells (18) (**Figure 3.2A**). When comparing the CRISPR scores in erlotinib-treated vs. DMSO-treated screens, *RIT1* emerged as a top essential gene, as expected (**Figure 3.2B, Figure 3.10A, and Supplementary Table 1**). Another top essential gene was the deubiquitinase *USP9X* (**Figure 3.2B, Figure 3.10A, and Supplementary Table 1**). To validate the result of the screen that USP9X is necessary for RIT1-induced resistance to EGFR inhibition, we generated pooled populations of $RIT1^{M90I}$-mutant PC9-Cas9 cells harboring a guide RNA targeting *USP9X* or *RIT1* (**Figure 3.2C**). Knockout of *USP9X* or *RIT1* resensitized cells to erlotinib and osimertinib (**Figure 3.2D-E and Figure 3.10B-C**). As an orthogonal approach to CRISPR knockout, we utilized siRNAs to knockdown *USP9X*. Knockdown of *USP9X* resensitized $RIT1^{M90I}$-mutant cells to erlotinib (**Figure 3.2F**) and osimertinib (**Figure 3.10D**). Together, these experiments show that USP9X is required for *RIT1*-driven drug resistance in $RIT1^{M90I}$-mutant PC9 cells.

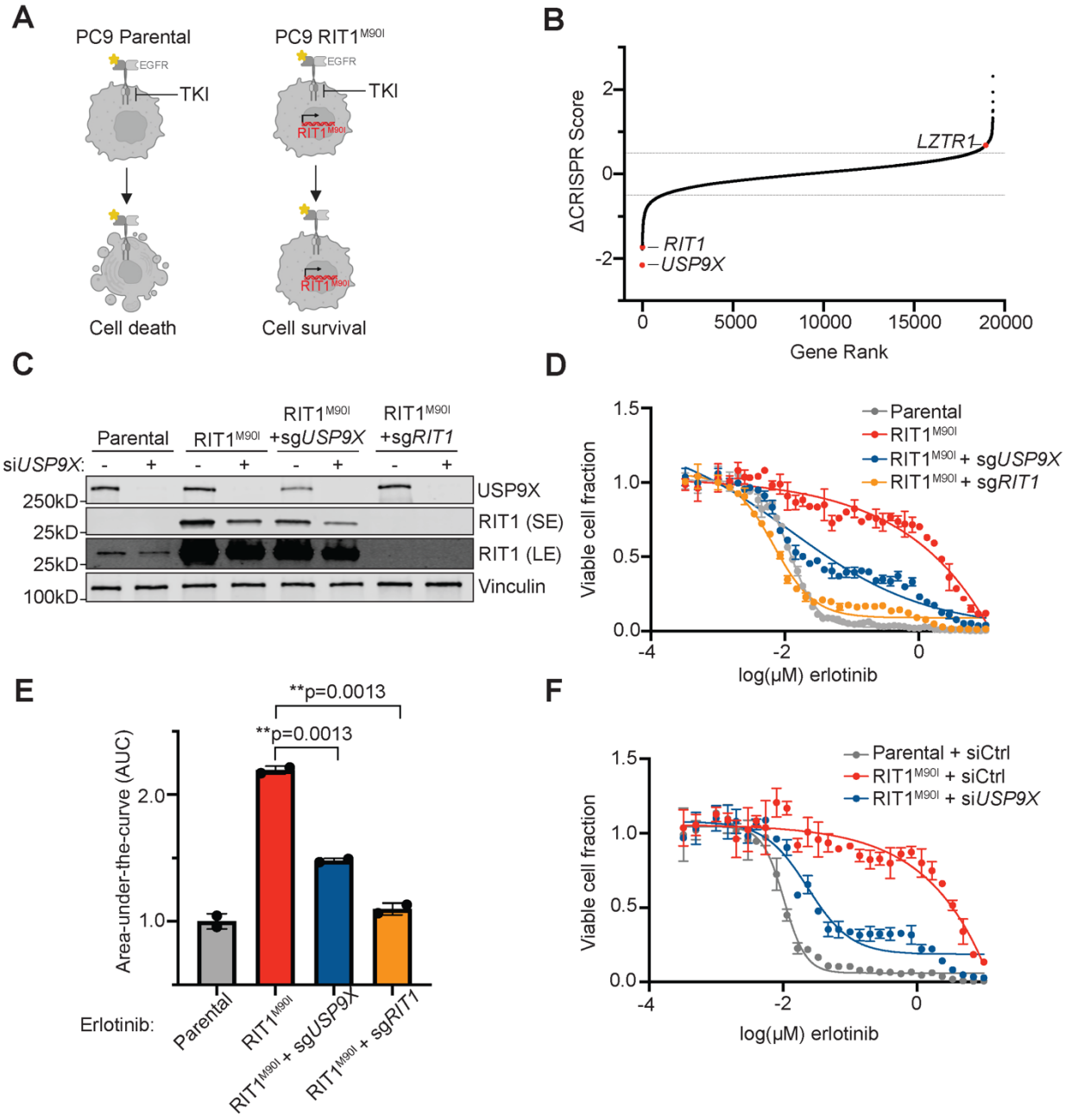

Figure 3.2. USP9X depletion reverses *RIT1*-driven erlotinib resistance.

A) Schematic of *RIT1*-driven EGFR tyrosine kinase inhibitor (TKI) resistance. Left, *EGFR*-mutant PC9 cells are sensitive to EGFR TKI's such as erlotinib. Right, expression of RIT1^{M90I} in PC9 cells confers EGFR TKI resistance. Figure created with Biorender.com.

B) Gene rank plot of previously published CRISPR/Cas9 whole-genome screen performed in RIT1^{M90I}-mutant PC9-Cas9 cells. ΔCRISPR Score is the difference between CRISPR scores in the erlotinib screen vs. CRISPR Scores in the DMSO screen.

C) Western blot of PC9-Cas9 cells treated with siCtrl or si*USP9X* for 48 hours. RIT1 bands are shown from a short exposure (SE) and long exposure (LE) to visualize both wild-type and mutant RIT1 abundance. Vinculin serves as a loading control.

D) Dose-response curves of PC9-Cas9 Parental cells and RIT1^{M90I}-mutant PC9-Cas9 cells with indicated gene knockouts (sg*RIT1* and sg*USP9X*) treated with erlotinib for 72 hours. Knockouts confirmed from Western blot in (C). CellTiterGlo was used to quantify viable cell fraction determined by normalization to DMSO control. Data shown are the mean $\pm$ s.d. of two technical replicates. Data are representative results from n = 2 independent experiments.

E) Area-under-the-curve (AUC) analysis of dose response curves shown in (D). p-values calculated by unpaired two-tailed t-tests.

F) Dose-response curves of RIT1^{M90I}-mutant PC9 cells treated with siCtrl or si*USP9X* for 48 hours, prior to treatment with erlotinib for 72 hours. Knockdowns validated by Western blot in (C). CellTiterGlo was used to quantify viable cell fraction determined by normalization to DMSO control. Data shown are the mean $\pm$ s.d. of two technical replicates. Data are representative results from n = 3 independent experiments.

Given that the protein abundance of RIT1 is known to be important for its function (26), we were intrigued to see the deubiquitinase *USP9X* as a top essential gene in *RIT1*-mutant cells (**Figure 3.2B, Figure 3.10A, and Supplementary Table 1**). We hypothesized that USP9X may be positively regulating RIT1 levels, and *USP9X* knockout would reduce RIT1 protein abundance. Indeed, *USP9X* knockout reduced $RIT1^{M90I}$ protein abundance, and complete ablation of *USP9X* with an additional siRNA resulted in further reduction of $RIT1^{M90I}$ (**Figure 3.2C**). This suggests that USP9X positively regulates RIT1 protein abundance. In addition to EGFR TKI resistance, expression of $RIT1^{M90I}$ is known to promote anchorage-independent growth (9). Given this, we investigated how USP9X regulates proliferation phenotypes in *RIT1*-mutant PC9 cells.

Under normal media conditions, genetic depletion of *RIT1* and *USP9X* did not affect the proliferation of *RIT1*-mutant cells (**Figure 3.11A**). In the context of erlotinib, PC9-Cas9-$RIT1^{M90I}$ cells depend on RIT1 for growth; therefore, genes required under erlotinib treatment are RIT1 dependency genes (**Figure 3.2A**). Because of this, we expect that the effect of *USP9X* depletion will be most pronounced when cells are treated with an EGFR inhibitor. Under erlotinib treatment, $RIT1^{M90I}$ + sg*USP9X* cells and $RIT1^{M90I}$ + sg*RIT1* cells proliferated slower than $RIT1^{M90I}$ cells (**Figure 3.3A**). In addition to 2D growth on tissue culture plates, we explored 3D growth via soft agar colony formation assays in DMSO and erlotinib (**Figure 3.3B**). After normalizing to the DMSO condition, we found that $RIT1^{M90I}$ + sg*USP9X* and $RIT1^{M90I}$ + sg*RIT1* cells formed significantly fewer colonies compared to $RIT1^{M90I}$ cells (**Figure 3.3C**).

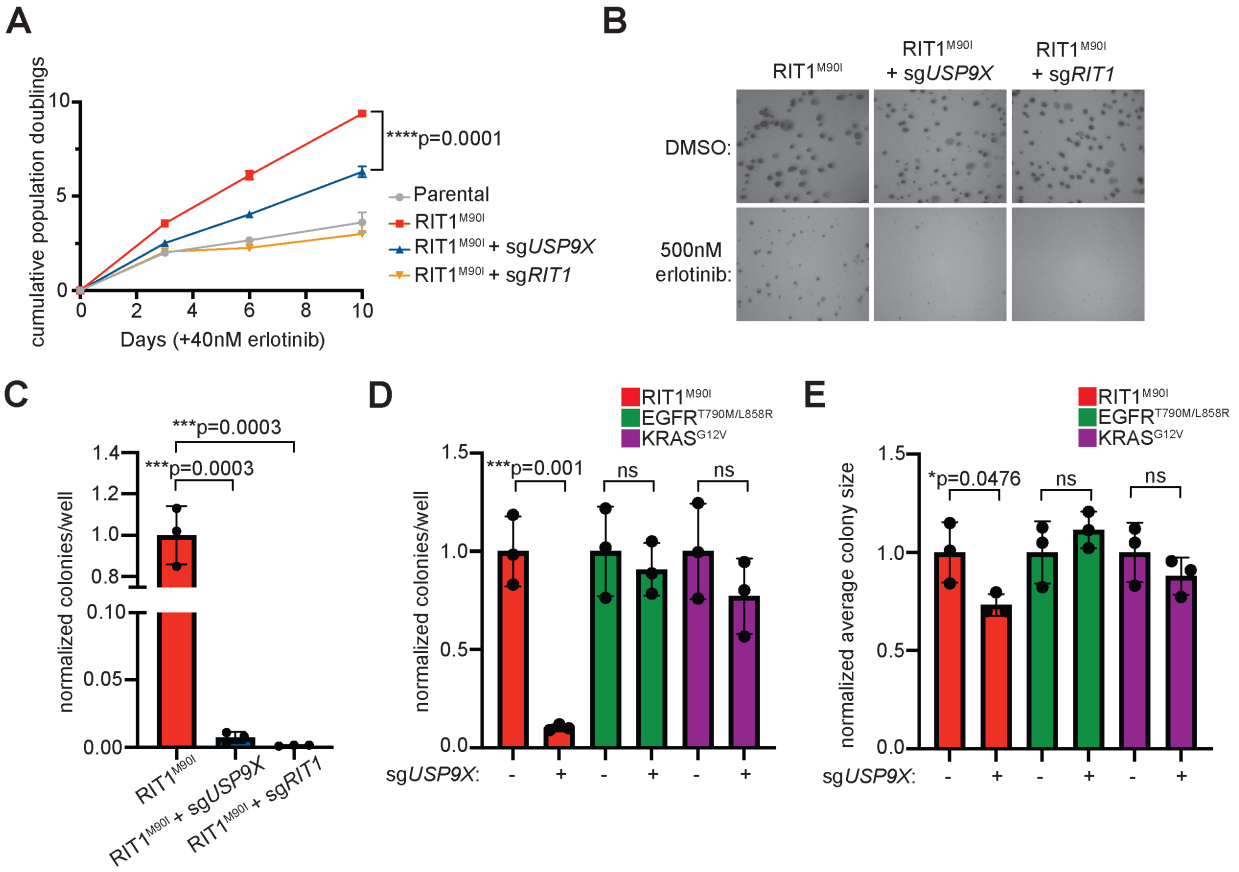

Figure 3.3. USP9X regulates *RIT1*-driven proliferation and anchorage-independent growth.

A) Proliferation of PC9-Cas9 Parental cells and RIT1^{M90I}-mutant PC9-Cas9 cells with indicated gene knockouts (sg*RIT1* and sg*USP9X*) treated with 40 nM erlotinib. Data shown are the mean ± s.d. of three technical replicates per cell line. Data are representative results from n = 2 independent experiments. p-value calculated by multiple unpaired two-tailed t-tests.

B) Representative images of soft agar colony formation assay in and RIT1^{M90I}-mutant PC9-Cas9 cells with indicated gene knockouts (sg*RIT1* and sg*USP9X*) treated with DMSO or 500 nM erlotinib. Images captured at 4X after 10 days of growth. Scale bar is 100 μM.

C) Normalized counts of colonies per well formed by indicated cell lines treated with 500nM erlotinib. All data were normalized to DMSO for each cell line, and then normalized to RIT1^{M90I}. Counts taken after 10 days of growth. Data shown are the mean ± s.d. of three technical replicates per cell line. p-values calculated by unpaired two-tailed t-tests.

D) Normalized counts of colonies per well formed by indicated PC9-Cas9 cell lines expressing RIT1^{M90I}, EGFR$^{T790M/L858R}$, or KRAS^{G12V} with or without sg*USP9X*. All data were normalized to DMSO for each cell line, and then normalized to parental (no sg*USP9X*) cell lines. Counts taken after 10 days of growth. Data shown are the mean ± s.d. of three technical replicates per cell line. p-values calculated by unpaired two-tailed t-tests.

E) Normalized average colony area of all colonies formed by indicated cell lines treated with 500 nM erlotinib for 10 days. All data were normalized to DMSO control for each cell line, and then normalized to parental (no sg*USP9X*) conditions. Data shown are the mean ± s.d. of three technical replicates per cell line. p-values calculated by unpaired two-tailed t-tests. Data in C-E are representative results from n = 2 independent experiments.

To confirm that this USP9X dependency is specific to *RIT1*-mutant cells, we performed the soft agar experiment in erlotinib-resistant *KRAS*- and *EGFR*-mutant PC9-Cas9 cells with or without sg*USP9X* (**Figure 3.11B**). As expected, *USP9X* knockout did not affect the number of colonies formed by $KRAS^{G12V}$ and $EGFR^{T790M/L858R}$-mutant cells (**Figure 3.3D**). We also assessed the size of colonies formed in erlotinib and found no difference in *USP9X* knockout *KRAS*- or *EGFR*-mutant PC9 cells, while *USP9X* knockout decreased the colony size of *RIT1*-mutant cells (**Figure 3.3E**). To further confirm that this USP9X dependency is specific to *RIT1*-mutant cells and not influenced by potential other known USP9X substrates, we confirmed that *USP9X* knockout did not affect the abundance of the pro-survival protein MCL1 in PC9 cells (**Figure 3.11C**) (138). These data demonstrate that USP9X is important for maintaining *RIT1*-driven proliferation and anchorage-independent growth.

3.4 USP9X REGULATES RIT1 ABUNDANCE AND STABILITY IN MULTIPLE CELL LINES

We hypothesized that *USP9X* knockout may reduce the abundance of RIT1, thus explaining USP9X's ability to counteract RIT1 function observed above. We already observed that *USP9X* knockout reduced RIT1 abundance in $RIT1^{M90I}$-mutant PC9 cells (**Figure 3.2C**), and we expanded upon these findings. In parental PC9 cells (which express endogenous, wild-type RIT1), si*USP9X* significantly reduced wild-type RIT1 protein abundance (**Figure 3.4A-B**). In PC9 cells expressing ectopic $RIT1^{M90I}$, CRISPR-mediated depletion of *USP9X* also significantly reduced the abundance of $RIT1^{M90I}$ (**Figure 3.4C-D**). Importantly, we found no difference in *RIT1* mRNA expression in si*USP9X*-treated parental and $RIT1^{M90I}$-mutant PC9 cells (**Figure 3.12A-B**), suggesting that differences in RIT1 protein abundance are due to post-translational modifications.

In addition to protein abundance, we explored the stability of RIT1 in the context of *USP9X* depletion. Cells were treated with cycloheximide (CHX) to inhibit protein translation, and the level of RIT1 was monitored over time by western blot. In *USP9X* knockout PC9 cells, RIT1 level decreased faster over the course of 12 hours compared to parental cells (**Figure 3.4E**). The half-life of RIT1 in parental cells was approximately 7.6 hours compared to 2.4 hours in *USP9X* knockout cells (**Figure 3.4F**). By the 6 hour time-point, we consistently found that RIT1 protein abundance was significantly lower in *USP9X* knockout cells compared to parental (**Figure 3.4G**). Together, these data show that USP9X is important for maintaining RIT1 protein abundance.

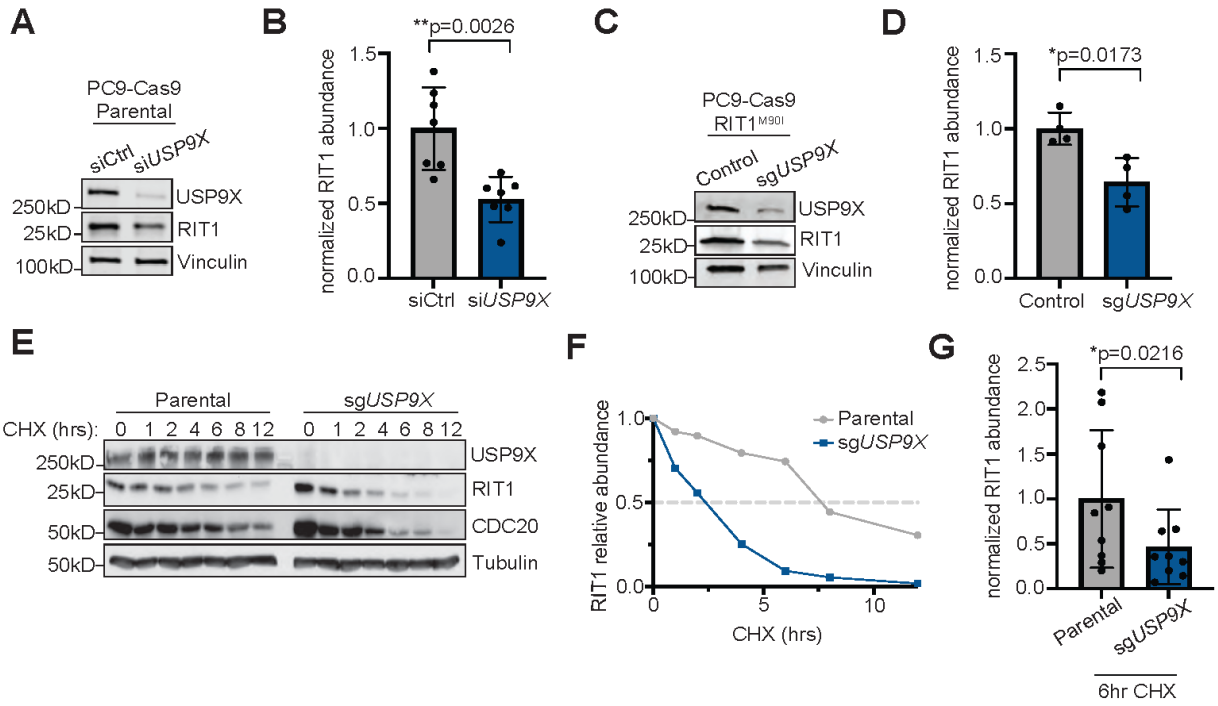

Figure 3.4. USP9X controls RIT1 abundance and stability in PC9 lung adenocarcinoma cells.

- **A)** Western blot of PC9-Cas9 Parental cells treated with indicated siRNAs for 48 hours. Vinculin serves as a loading control.
- **B)** Quantification of Western blot band intensity of RIT1 bands in (A). Data shown are the mean ± s.d. of three independent experiments with 2-3 biological replicates per condition. p-value calculated by paired two-tailed t-test.

C) Western blot of RIT1^{M90I}-mutant PC9-Cas9 cells (Control) and a CRISPR-engineered clonal *USP9X* KO (sg*USP9X*) cell line. Vinculin serves as a loading control.

D) Quantification of Western blot band intensity of RIT1 bands in (C). Data shown are the mean ± s.d. of two independent experiments with 2 biological replicates per condition. p-value calculated by paired two-tailed t-test.

E) PC9-Cas9 parental and sg*USP9X* cells treated with 100 μg/mL cycloheximide (CHX) for the indicated time periods before harvesting for Western blot. CDC20 serves as a positive control for USP9X activity. Tubulin serves as a loading control. Data are representative of n = 3 independent experiments.

F) Half-life analysis of RIT1 protein abundance over time based on RIT1 band intensity in (E).

G) Comparison of RIT1 protein abundance based on Western blot band intensity of aggregated cycloheximide-chase experiments in cells treated with CHX for 6 hours. Data shown are the mean ± s.d. of three independent experiments with 3 technical replicates per cell line. p-value calculated by paired two-tailed t-test.

To extend these findings to another cell context, we utilized NCI-H2110 cells, which is currently the only commercially available lung adenocarcinoma cell line that harbors an endogenous RIT1^{M90I} mutation (9). Similar to our results in PC9 cells, treatment with si*USP9X* significantly reduced the abundance of RIT1^{M90I} (**Figure 3.12C-D**). As orthogonal confirmation, we generated NCI-H2110 cell lines incorporating an inducible (iCas9) system where expression of Cas9 is under control of doxycycline (dox) (165). Following dox treatment and Cas9 expression, *USP9X* knockout significantly decreased RIT1 abundance (**Figure 3.12E-F**). To rule out the possibility that changes to USP9X protein abundance are due to changes in gene expression, we performed RT-qPCR. No difference in *RIT1* mRNA expression was observed in sg*USP9X* cells (**Figure 3.12G**), indicating that USP9X's regulation of RIT1 occurs post-transcriptionally and also confirming this relationship occurs in other cell contexts.

To further validate USP9X's regulation of RIT1 in other cell types, we analyzed the effects of USP9X depletion in AALE lung epithelial cells. AALE cells are an immortalized, non-transformed human lung epithelial cell line (166). We expressed FLAG-tagged RIT1^{WT} and RIT1^{M90I} in these cells and treated with si*USP9X* (**Figure 3.5A-B**). As expected, *USP9X* knockdown reduced the abundance of both wild-type and mutant RIT1. Of note, we also saw reduction of endogenous wild-type RIT1 in parental AALE cells (**Figure 3.5A-B**). Although the difference in FLAG-RIT1^{WT} abundance was not statistically significant in these experiments, the marked reduction of endogenous RIT1 in parental AALE cells suggests that USP9X is also targeting wild-type RIT1 in this system (**Figure 3.5A-B**). It is possible that the FLAG tag or other factors prevent USP9X's interaction with FLAG-RIT1^{WT}, but this requires further experimentation. Together, these data indicate that USP9X regulates RIT1 across numerous lung cancer cell types.

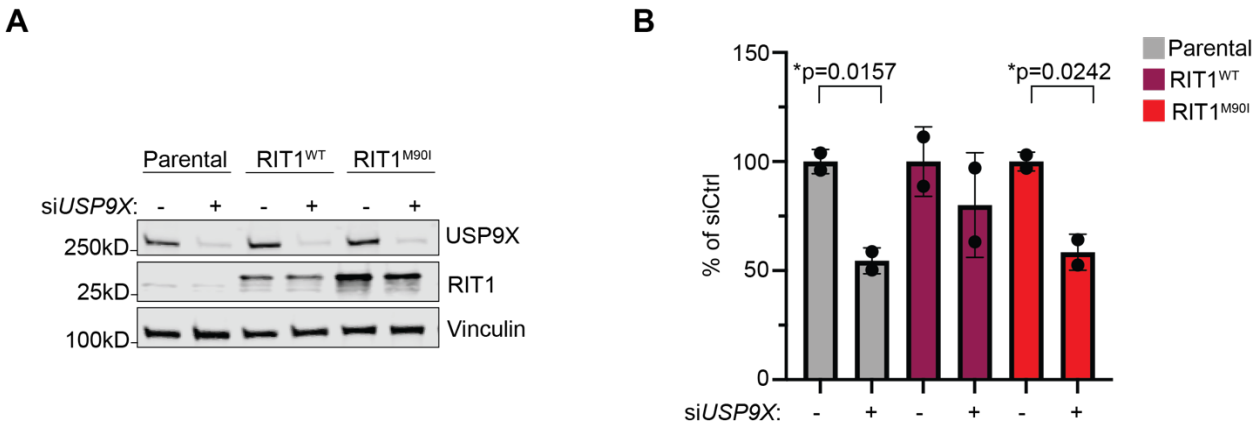

Figure 3.5. USP9X regulates RIT1 protein abundance in AALE cells.

- **A)** Western blot of AALE cells treated with siCtrl or si*USP9X* for 72 hours. FLAG-tagged RIT1 shows an upwards shift in molecular weight due to the FLAG tag. Vinculin serves as a loading control.
- **B)** Quantification of RIT1 band intensity from Western blot in (A). p-values calculated by unpaired two-tailed t-tests. Data are representative of two independent experiments.

3.5 Paired-guide approach to knockout *USP9X*

When trying to achieve knockout of *USP9X*, we employed multiple different methods, including CRISPR-mediated knockout and siRNA knockdowns. Overall, we found that most single-guide CRISPR knockouts were incomplete (**Figure 3.6A**). The siRNA method proved effective, but as a transient approach it is not always applicable for longer time-course experiments. To improve knockouts, in H2110iCas9 cells we implemented a paired-guide approach incorporating two unique guides per gene target (**Figure 3.6B-D**). We predicted that transducing cells with two guide RNAs targeting the same gene would give a better overall knockout. We compared single guide (sgRNA) and paired-guide (pgRNA) approaches (**Figure 3.6E-F**). Overall, the paired guides performed slightly better than single guide approaches. This pgRNA method for improving genetic knockouts could be useful for other difficult targets. Genetic knockdowns and knockouts remain a useful tool for understanding the role(s) of certain genes in cellular mechanisms, and improving our knockout technology will help facilitate these studies. Most genes are easily targetable with efficient guide RNAs, but other genes—such as *USP9X*—could require the implementation of multi-guide approaches to establish stable knockout cell lines.

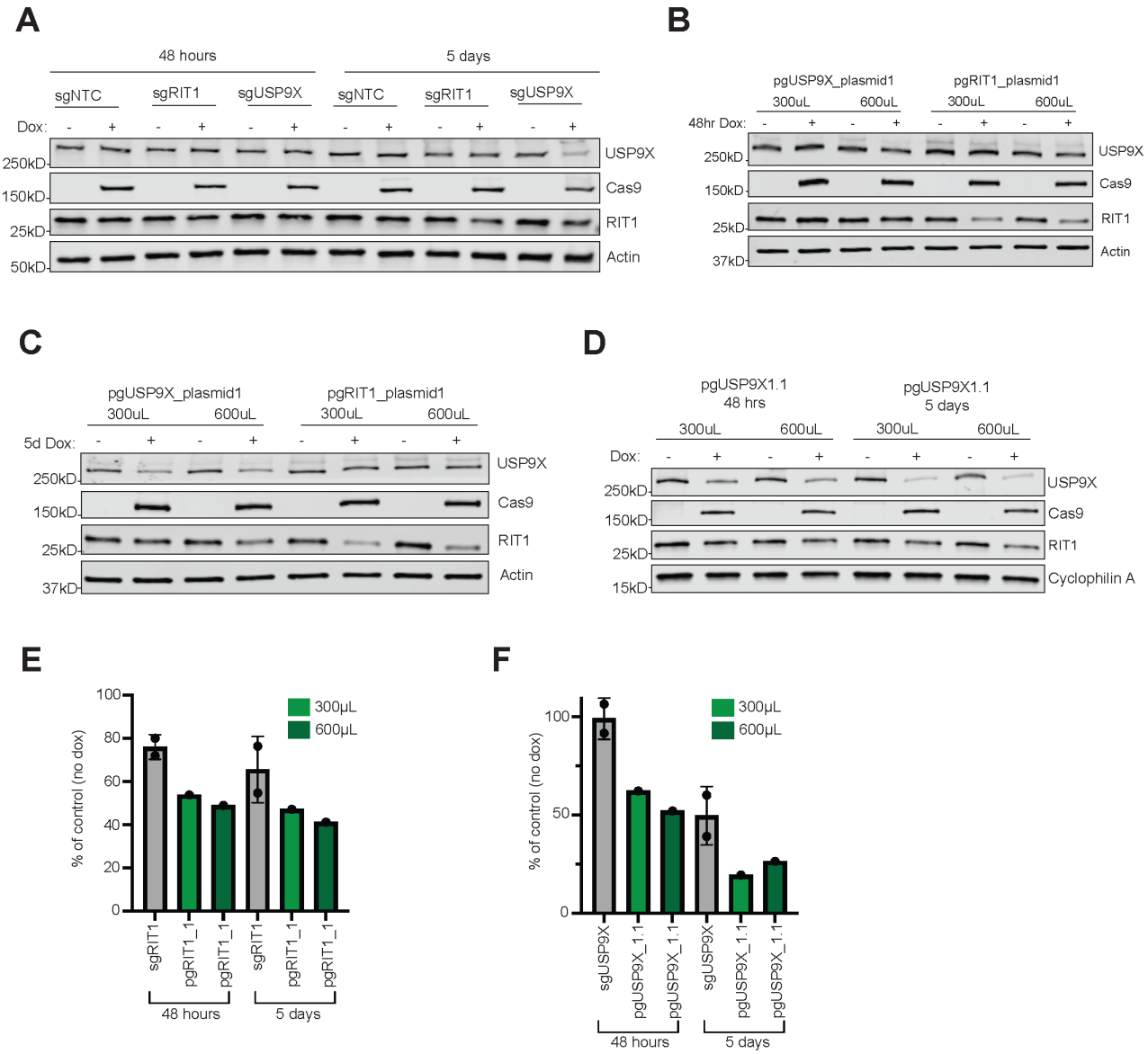

Figure 3.6. Paired-guide approach for genetic knockout.

A) Western blot of H2110iCas9 cells harboring single-gene (sg) guide RNAs targeting indicated genes. Cells were treated with doxycycline/dox (to induce Cas9 expression) for 48 hours or 5 days. Actin serves as a loading control.

B) Western blot of H2110iCas9 cells harboring paired-gene (pg) guide RNAs targeting indicated genes. Cells were transfected with either 300 µL or 600 µL of lentivirus for pgRNA delivery. Plasmid # indicates the paired-guide construct used to generate the cell line. Cells were treated with doxycycline/dox for 48 hours. Actin serves as a loading control.

C) Western blot of H2110iCas9 cells harboring paired-gene (pg) guide RNAs targeting indicated genes. Cells were transfected with either 300 µL or 600 µL of lentivirus for pgRNA delivery. Plasmid # indicates the paired-guide construct used to generate the cell

line. Cells were treated with doxycycline/dox for 5 days. Actin serves as a loading control.

D) Western blot of H2110iCas9 cells harboring paired-gene (pg) guide RNAs targeting indicated genes. Cells were transfected with either 300 µL or 600 µL of lentivirus for pgRNA delivery. Plasmid # indicates the paired-guide construct used to generate the cell line. Cells were treated with doxycycline/dox for 48 hours or 5 days. Cyclophilin A serves as a loading control.

E) Quantification of Western blot band intensity for single-guide and paired-guide approaches for RIT1 knockout from (A-C).

F) Quantification of Western blot band intensity for single-guide and paired-guide approaches for USP9X knockout from (A) and (D). Construct 1.1 was chosen due to its higher knockout efficiency.

3.6 RIT1 UBIQUITINATION IS MEDIATED BY USP9X'S CATALYTIC ACTIVITY

To identify potential DUBs of RIT1 in an unbiased manner, we fused RIT1 to a ubiquitin molecule through a flexible peptide linker to obtain a constitutively ubiquitinated form of RIT1 that we termed RIT1$^{\sim Ub}$ (**Figure 3.7A**). This construct acts as a molecular trap, by stabilizing interaction with DUBs, which are unable to cleave the peptide bond (167). Next, we undertook affinity-purification mass spectrometry in HEK293T cells using our RIT1$^{\sim Ub}$ mutant. In cells expressing RIT1$^{\sim Ub}$, we found enrichment of RIT1 and LZTR1 peptides compared to control cells transfected with empty vector (**Figure 3.7B and Figure 3.13A-C**). We also found a similar enrichment of USP9X peptides (**Figure 3.7B, Figure 3.13A and Figure 3.13D**), indicating that USP9X is physically interacting with ubiquitinated RIT1.

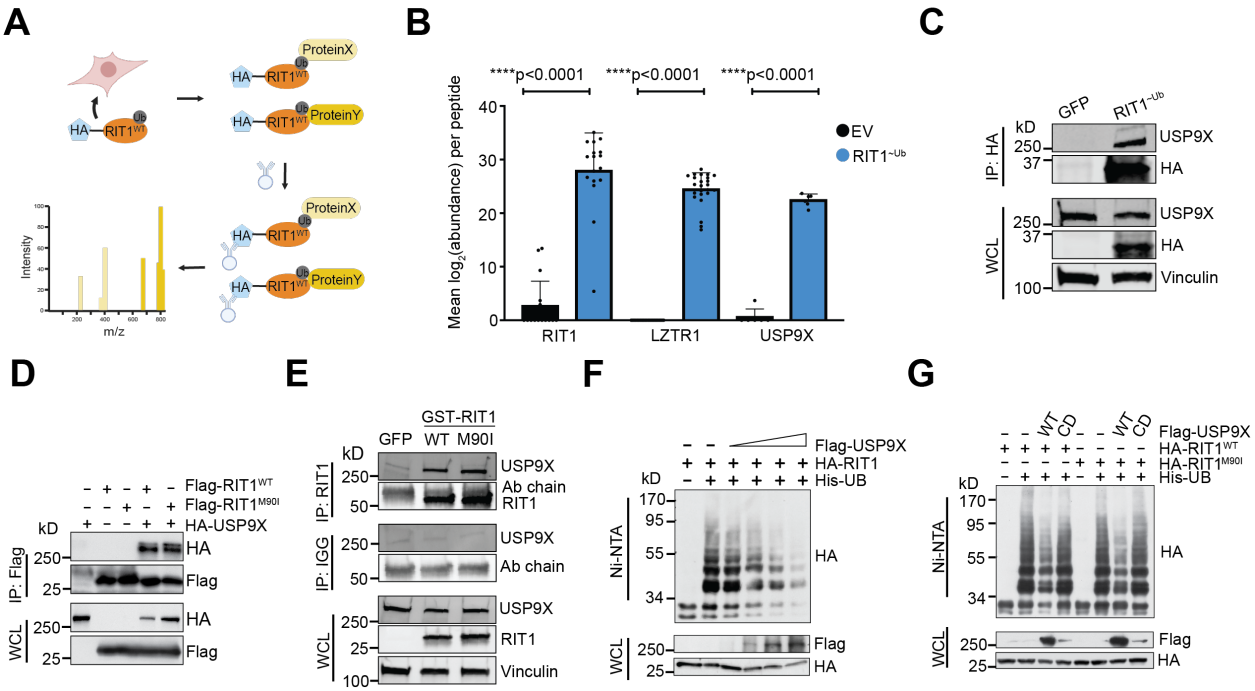

Figure 3.7. USP9X binds to and deubiquitinates RIT1.

A) Schematic of affinity-purification/mass-spectrometry (AP/MS) experiment performed in HEK293T cells transfected with RIT1$^{\sim Ub}$ vector. This experiment was designed to identify proteins that bind to ubiquitinated RIT1. Figure created with Biorender.com.

B) Mean abundance (log_2-transformed) of peptides across biological replicates (n = 7 for Empty Vector/EV and n = 4 for RIT1$^{\sim Ub}$) of affinity purification/mass spectrometry experiment. p-values calculated by paired two-tailed t-tests.

C) Co-immunoprecipitation in HEK293T cells transfected with GFP control or RIT1$^{\sim Ub}$. Vinculin serves as a loading control. Data shown is representative of n = 2 independent experiments.

D) Western blot of whole cell lysates (WCL) and anti-Flag immunoprecipitates (IP) derived from HEK293T cells transfected with Flag-RIT1^{WT} or Flag-RIT1^{M90I} together with the HA-USP9X construct. 36 hours post-transfection, cells were pretreated with 10 μM MG132 for 10 hours before harvesting. Data shown are representative of n = 4 replicates for RIT1^{WT} and n = 1 replicates for RIT1^{M90I}.

E) Co-immunoprecipitation experiment in HEK293T cells transfected with indicated GST-tagged RIT1 variants or a GFP transfection control. Vinculin serves as a loading control. Data shown are representative of n = 2 independent experiments.

F) Western Blot of WCL and subsequent His-tag pull-down in 6 M guanine-HCl containing buffer derived from HEK293T cells transfected with the indicated plasmids. Cells were pretreated with 10 μM MG132 for 16 hours to block the proteasome pathway before harvesting. Data shown are representative of n = 3 independent experiments.

G) Ubiquitination experiment as described in (F) in HEK293T cells transfected with RIT1^{WT} and RIT1^{M90I}, as well as wild-type or catalytically dead (CD) USP9X. Data shown are representative of n = 3 independent experiments.

To further validate the physical interaction of USP9X and RIT1, we performed co-immunoprecipitation experiments in HEK293T cells expressing FLAG-tagged RIT1 (wild-type and $RIT1^{M90I}$) and HA-tagged USP9X and saw evidence for interaction of $RIT1^{WT}$ and $RIT1^{M90I}$ with USP9X (**Figure 3.7D**). To rule out potential confounding factors related to tagged USP9X, we performed this experiment with endogenous USP9X in HEK293T cells and found that endogenous USP9X also interacts with $RIT1^{WT}$ and $RIT1^{M90I}$ (**Figure 3.7E**).

To investigate if USP9X is regulating RIT1 ubiquitination, we transiently transfected HA-tagged RIT1 and His-tagged ubiquitin in HEK293T cells. We titrated increasing amounts of Flag-USP9X and found that ubiquitinated RIT1 decreased in a dose-dependent manner in relation to the amount of USP9X expressed (**Figure 3.7F**). To expand upon these findings, we performed ubiquitin-pulldown experiments with a catalytically dead (CD) form of USP9X that harbors an active site mutation (C1566A) which ablates its deubiquitinase activity (118). Expression of wild-type USP9X reduced ubiquitination of $RIT1^{WT}$ and $RIT1^{M90I}$, but expression of $USP9X^{CD}$ did not affect RIT1 ubiquitination (**Figure 3.7G**). These experiments confirm that the deubiquitinase activity of USP9X is responsible for modulating ubiquitination of RIT1.

3.1 USP9X COULD BE A PROMISING THERAPEUTIC TARGET FOR *RIT1*-DRIVEN DISEASES

Our findings suggest that *USP9X* genetic depletion reduces RIT1 protein abundance and abrogates *RIT1*-driven oncogenic phenotypes. As such, pharmacological inhibition of USP9X is predicted to have similar effects, and USP9X could be a promising drug target in diseases characterized by *RIT1* mutations and amplifications. Of note, these implications are not limited to lung adenocarcinoma. Analysis of the Cancer Dependency Map and associated proteomics datasets (168) revealed a positive correlation between USP9X protein abundance and RIT1

protein abundance (**Figure 3.8A**), suggesting that this regulation may extend to multiple cancer types driven by *RIT1* alterations. Importantly, this correlation was also seen with CDC20–a known USP9X substrate (118) (**Figure 3.8B**), whereas no correlation was observed when comparing USP9X protein abundance to mRNA expression of *RIT1* (**Figure 3.8C**) or *CDC20* (**Figure 3.8D**) (169). Additionally, analysis of *RIT1* copy number data in lung cancer cell lines revealed that cell lines with *RIT1* amplifications (i.e. copy number greater than 2) were more dependent on USP9X (**Figure 3.14A**). A similar analysis of *RIT1* expression data showed that lung cancer cell lines with increased expression of RIT1 had lower *USP9X* CRISPR scores (**Figure 3.14B**). Although we did not find any statistical differences across these groups, trends in these data are consistent with the copy number analysis (**Figure 3.14A**).Thus, pharmacological inhibition of USP9X could be an intriguing strategy to promote RIT1 degradation, which would be detrimental to the growth and proliferation of tumors driven by *RIT1* mutations and amplifications (**Figure 3.8E**).

Together, we propose a model whereby USP9X positively regulates wild-type and mutant RIT1 (**Figure 3.8E**). We predict that this regulation counteracts the effects of LZTR1 on wild-type RIT1 (**Figure 3.8E**). LZTR1 promotes K48 polyubiquitination of $RIT1^{WT}$ at K187 and K135 (26). Given this, it is possible that USP9X deubiquitinates $RIT1^{WT}$ at these lysine sites. Future work is needed to identify the precise lysines targeted by USP9X, and whether this varies between wild-type and mutant forms of RIT1. The E3 ligase responsible for ubiquitinating mutant RIT1 has yet to be identified (**Figure 3.8E**). In summary, our work builds upon the understanding that the protein abundance of RIT1 is key to its function, and we have identified USP9X as a positive regulator of wild-type and mutant RIT1.

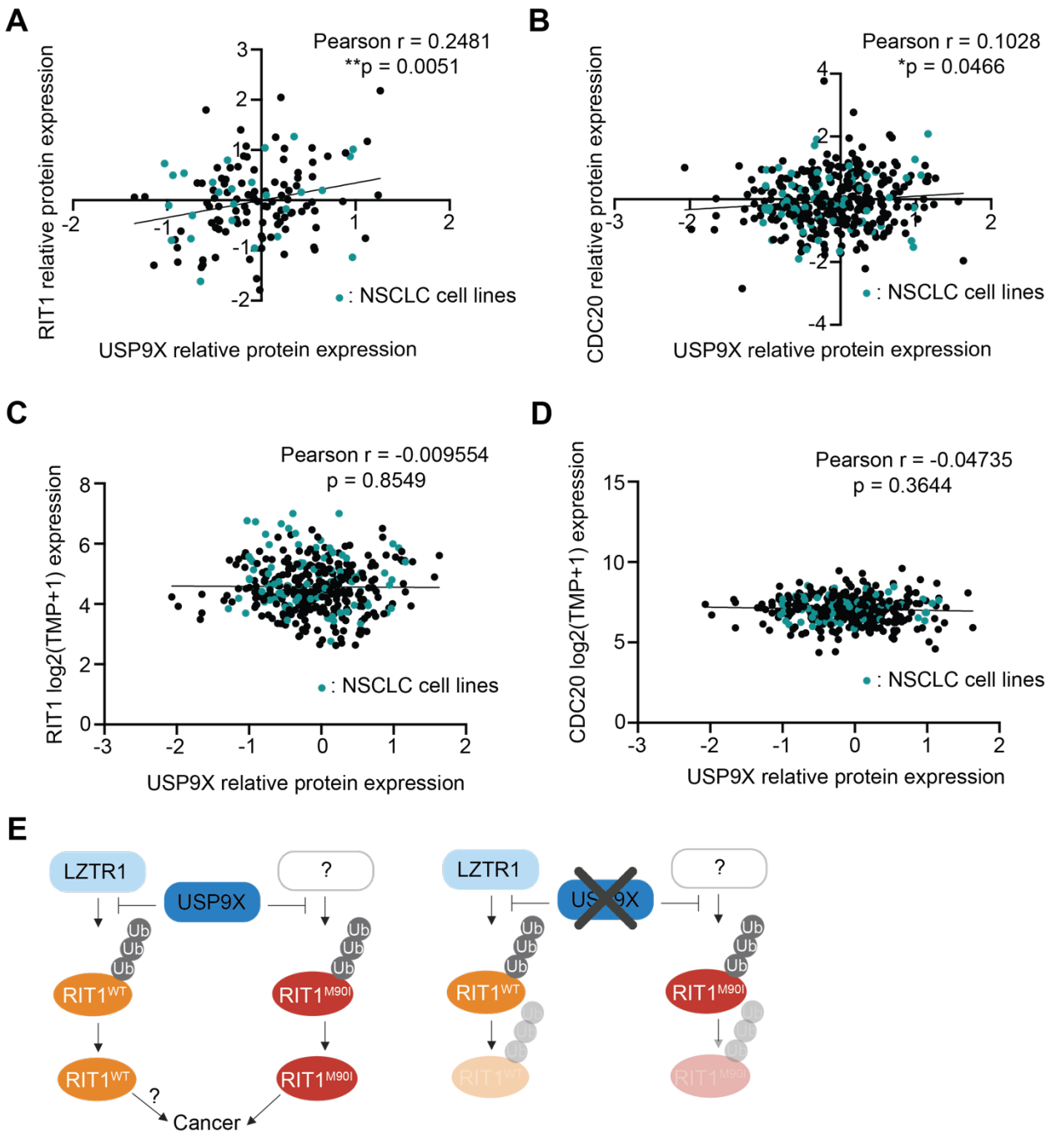

Figure 3.8. USP9X-mediated regulation of RIT1 is relevant across cancer types.

A) Correlation of proteomics data (168) from the Cancer Dependency Map (DepMap) comparing USP9X (Q93008) and RIT1 (Q92963-3). Pearson r and p-values calculated in Prism.

B) Correlation of DepMap proteomics data (168) comparing USP9X (Q93008) and CDC20 (Q12834). Pearson r and p-values calculated in Prism.

C) Correlation of DepMap gene expression data (Expression Public 23Q2) (169) for RIT1 and USP9X proteomics data (Q93008) (168). Pearson r and p-values calculated in Prism.

D) Correlation of DepMap gene expression data (Expression Public 23Q2) (169) for CDC20 and USP9X proteomics data (Q93008) (168). Pearson r and p-values calculated in Prism.

E) Proposed model (left) of RIT1 protein regulation. $RIT1^{WT}$ is ubiquitinated by LZTR1, while $RIT1^{M90I}$ is ubiquitinated by a currently unknown E3 ligase. USP9X counteracts the ubiquitination of both wild-type and mutant RIT1. Increased RIT1 abundance and stability are important for RIT1 function and disease progression. The exact biological consequences of $RIT1^{WT}$ amplification have yet to be elucidated. Genetic knockout (right) of *USP9X* prevents RIT1 deubiquitination, thereby promoting RIT1 degradation and abrogating oncogenic phenotypes. Figure created with Biorender.com.

3.2 Discussion

Our group previously performed CRISPR screens to explore *RIT1* genetic dependencies (18) and identified the deubiquitinase *USP9X* as a genetic regulator of RIT1 function (18). This finding was particularly interesting given that there is a growing understanding that the protein abundance of RIT1 is important for its function (26,34,44). Mutant forms of RIT1 evade regulation by the $CRL3^{LZTR1}$ complex, thereby increasing RIT1 protein abundance (26). As such, it is highly probable that the activity of RIT1 is also regulated by DUBs.

Given the function of USP9X as a deubiquitinase, we predicted that USP9X would physically interact with and modify the ubiquitination status of RIT1. Our unbiased AP/MS approach revealed that USP9X interacts with mono-ubiquitinated RIT1 (**Figure 3.7A-B, Figure 3.13A, and Figure 3.13D**). As expected, this assay also detected LZTR1–a known RIT1 interactor–thereby increasing the robustness of our findings (**Figure 3.7B, Figure 3.13A, and Figure 3.13C**). We further validated the physical interaction of USP9X and RIT1 in HEK293T cells (**Figure 3.7D-E**) and confirmed that the catalytic activity of USP9X regulates the ubiquitination status of $RIT1^{WT}$ and $RIT1^{M90I}$ (**Figure 3.7F-G**). Our findings suggest that USP9X deubiquitinates $RIT1^{M90I}$, but we have yet to identify the E3 ubiquitin ligase(s) that is

promoting ubiquitination. In our CRISPR screen, we identified 22 E3 ligases that were positively selected (**Supplementary Table 1**), meaning that individual genetic knockout of these ligases conferred a growth advantage in *RIT1*-mutant PC9 cells. Therefore, these genes are candidate E3 ligases that may target $RIT1^{M90I}$ independently or potentially cooperate with CRL^{LZTR1} to ubiquitinate RIT1. Systematic characterization and investigation of these 22 E3 ligases is required to further elucidate the protein-level regulation of $RIT1^{M90I}$.

Even though mutant RIT1 is the predominant form of RIT1 expressed in PC9 cells, LZTR1 was observed as a cooperating factor in our CRISPR screen (18). In other words, knockout of *LZTR1* conferred a growth advantage in $RIT1^{M90I}$-mutant PC9 cells (**Figure 3.2B, Figure 3.10A, and Supplementary Table 1**). This result was somewhat unexpected given that the M90I mutation in RIT1 prevents its interaction with LZTR1 (26). However, it is possible that LZTR1 is acting on the endogenous wild-type RIT1 that is also expressed in our engineered *RIT1*-mutant PC9 cells. Our work predicts that both USP9X and LZTR1 are acting on wild-type RIT1, while only USP9X is targeting mutant RIT1 (**Figure 3.8E**). The findings presented here support currently known mechanisms of RIT1 regulation (26,34,35,101), while also identifying USP9X as a novel regulator of both wild-type and mutant RIT1.

To confirm the dependency of *RIT1*-mutant cells on USP9X, we turned to our CRISPR screening system where we initially identified USP9X. This screen was performed with $RIT1^{M90I}$-mutant PC9 cells, which depend on $RIT1^{M90I}$ to confer resistance to EGFR inhibitors such as erlotinib or osimertinib (**Figure 3.2A**). In this setting, genes required under erlotinib treatment are RIT1 dependency genes. Given this context, we replicated the screen conditions when exploring USP9X-mediated regulation of RIT1. We validated this dependency in erlotinib- and osimertinib-treatment experiments (**Figure 3.2D-F and Figure 3.10B-D**). Notably, complete

knockdown of *USP9X* with siRNA resulted in a dramatic resensitization to erlotinib (**Figure 3.2C and Figure 3.2F**) and osimertinib (**Figure 3.2C and Figure 3.10D**), while incomplete knockout of *USP9X* via CRISPR editing only partially reverted this resistance phenotype (**Figure 3.2C-E and Figure 3.10B-C**). These differences in sensitivity appear to be directly related to the knockout efficiency of various techniques and further support the conclusion that USP9X is important for regulating *RIT1*-driven drug resistance.

As expected, *USP9X* knockout impaired the proliferation of *RIT1*-mutant cells in erlotinib (**Figure 3.3A**). In soft agar colony formation assays, *RIT1*-mutant *USP9X* knockout cells formed fewer and smaller colonies (**Figure 3.3C-E**). These phenotypic effects appear to be directly related to USP9X's regulation of RIT1 protein abundance. Importantly, USP9X knockout did not affect colony formation in erlotinib-resistant *EGFR*- or *KRAS*- mutant cells (**Figure 3.3C-E**). This coincides with our previous CRISPR screen results, where we found that USP9X is uniquely essential to *RIT1*-mutant cells (18). Given our knowledge of RIT1 biology and the importance of protein abundance, these data suggest that RIT1 itself is the substrate driving USP9X dependency.

Overall, we consistently found that USP9X depletion corresponded with decreased RIT1 protein abundance (**Figure 3.2C**, **Figure 3.4A-D**, **and Figure 3.12C-F**). *USP9X* knockdown did not affect *RIT1* gene expression (**Figure 3.12A-B, S3G**), suggesting that this regulation is occurring at the protein level. Of note, we recognize the limitations of the PC9 cell system in studying RIT1. PC9 cells harbor a mutation in *EGFR*, but in patient tumors *RIT1* mutations are almost always mutually exclusive with other mutations in the RTK/RAS pathway (2). Although the PC9+erlotinib/osimertinib system is an *in vitro*-based cell line model, it offers valuable insight into RIT1 regulation, genetic dependencies, and oncogenic mechanisms. Furthermore, our work

in NCI-H2110 cells (**Figure 3.12**), AALE cells (**Figure 3.5**) and DepMap analyses (**Figure 3.8A-D and Figure 3.14A-B**) underscores that RIT1 is a substrate of USP9X in other human lung cancer cell models and may be relevant across a wide range of cancer types. Indeed, USP9X could be a promising therapeutic target for diseases characterized by *RIT1* amplifications and mutations.

RIT1 regulation by a DUB could open up opportunities to inhibit DUB function and decrease RIT1 protein levels. Attempts have been made to develop small molecule inhibitors against USP9X. The compound WP1130 has been shown to inhibit USP9X as well as other DUBs including USP5, USP14, and UCH37 (170). In cells expressing high abundance of oncoproteins targeted by USP9X, WP1130 treatment abrogates growth and proliferation (171,172). However, the pre-clinical practicality of WP1130 is limited due to low solubility and poor bioavailability in animal models (173,174). The compound G9 was developed after WP1130 and is more soluble and less toxic than WP1130 (174). Experiments with G9 have shown promising results for breast cancer, leukemia, and melanoma cells harboring specific mutations (148,175–177). Notably, G9 has also been shown to target USP24 (178) and USP5 (179), so it is difficult to directly link the effects of this drug to USP9X inhibition. In 2021, a more specific USP9X inhibitor FT709 was developed with a nanomolar range IC50 (180). Unlike WP1130 or G9, FT709 does not target USP24 or USP5 (180). It will be intriguing to test if FT709 destabilizes RIT1 in NSCLC cells and whether FT709 sensitizing EGFRi-resistant NSCLC cells to EGFR or MAPK inhibition.

In summary, we identified USP9X as a positive regulator of RIT1 function. USP9X deubiquitinates wild-type and mutant RIT1 (**Figure 3.7F-G**), thereby increasing RIT1 abundance and stability. Given that protein abundance of RIT1 is important for its function (26), USP9X is a key factor in mediating *RIT1*-driven oncogenic phenotypes. Our work supports previously

known mechanisms of RIT1 regulation by LZTR1 (26,34,35), and we suggest that USP9X and LZTR1 oppose the action of one another in controlling the ubiquitination status of wild-type RIT1 (**Figure 3.8E**). We found that USP9X also targets $RIT1^{M90I}$ (**Figure 3.2C, Figure 3.4C-D, Figure 3.7D-E, Figure 3.7G, Figure 3.12C-F, and Figure 3.5A-B**) and future work is needed to identify other players within the ubiquitin-proteasome system that may be regulating mutant forms of RIT1 (**Figure 3.8E and Supplementary Table 1**). Additionally, more experimentation is required to understand the biological consequences of $RIT1^{WT}$ amplification in disease states. Overall, this work builds upon our knowledge of RIT1 biology and the mechanisms underlying how *RIT1* mutations and amplifications cause disease and improves our understanding of the role of USP9X in lung cancer. These insights can be leveraged in the future to develop robust novel therapies for diseases characterized by *RIT1* alterations.

3.3 Conclusion

Overall, this work supports previously known mechanisms of RIT1 protein regulation. The discovery of a DUB that targets mutant RIT1 may seem in contradiction with the finding that mutant RIT1 evades regulation by the cullin RING E3 ligase and the adaptor protein LZTR1. However, we are confident that our findings build upon current literature. To conclude this chapter, the interplay of LZTR1, USP9X, and RIT1 will be further addressed.

Our model predicts that LZTR1 may be acting on endogenous, wild-type RIT1 or other RAS proteins in this system. To explore this, we generated a clonal *LZTR1* knockout (KO) cell line (**Figure 3.9A**). We transduced PC9-Cas9 parental cells and the *LZTR1* KO cell line with FLAG-tagged $RIT1^{WT}$ or $RIT1^{M90I}$ (**Figure 3.9A**). As expected, *LZTR1* KO increased the abundance of wild-type RIT1 (**Figure 3.9A**). Upon *USP9X* knockdown, the abundance of $RIT1^{WT}$ and $RIT1^{M90I}$ decreased (**Figure 3.9A**). Dual knockout of *LZTR1* and *USP9X* rescued

the abundance of RIT1^{WT} but not RIT1^{M90I} (**Figure 3.9A**). Together, these results support previously published findings on LZTR1's regulation of wild-type RIT1 (26) and suggest that, unlike LZTR1, USP9X is able to act on both wild-type and mutant RIT1. In order to further confirm that USP9X–but not LZTR1–are modulating *RIT1*-driven EGFR inhibitor resistance, we treated FLAG- RIT1^{M90I}-expressing *LZTR1* KO cells with osimertinib and found that these cells have a similar osimertinib sensitivity to FLAG-RIT1^{M90I}-expressing cells, based on Area-Under-the-Curve (AUC) analysis (**Figure 3.9B**). *USP9X* knockdown resulted in a similar reversion of osimertinib sensitivity regardless of whether *LZTR1* was expressed (**Figure 3.9B**).

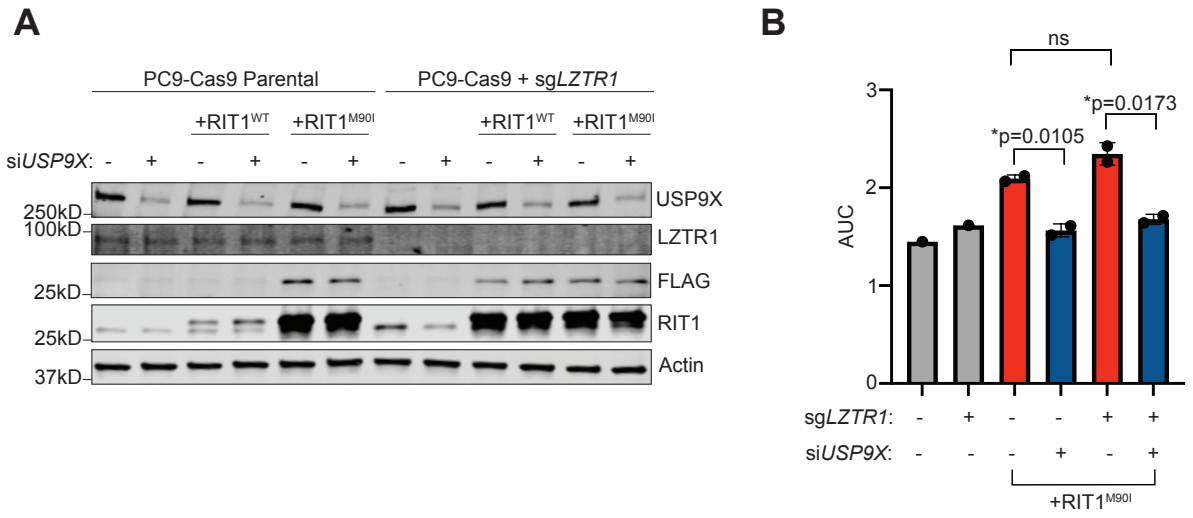

Figure 3.9. Evidence for dual LZTR1/USP9X regulation of wild-type RIT1.

A) Western Blot of PC9-Cas9 Parental cells and a clonal *LZTR1* KO cell line (sg*LZTR1*) expressing FLAG-tagged RIT1 variants and treated with indicated siRNAs for 48 hours. Actin serves as a loading control.

B) Area-Under-the-Curve (AUC) analysis of osimertinib-treated FLAG-RIT1^{M90I}-expressing PC9-Cas9 cells. p-values calculated by unpaired two-tailed t-tests. ns = not significant by unpaired two-tailed t-test. Data shown include n = 2 technical replicates from n = 2 biological replicates.

In summary, this work presents USP9X as a novel regulator of RIT1 protein abundance and suggests a model in which *RIT1* amplifications could be maintained by the opposing actions of LZTR1 and USP9X.

3.4 Materials and methods

3.4.1 *Cell lines*

PC9 cells were a gift from Dr. Matthew Meyerson (Broad Institute). PC9-Cas9 cells were generated as previously described (18). NIH3T3, NCI-H2110, and HEK293T cells were obtained from ATCC (CRL-1658, CRL-5924, and CRL-3216, respectively). PC9 and NCI-H2110 cells were cultured in RPMI-1640 (Gibco) supplemented with 10% Fetal Bovine Serum (FBS). NIH3T3 and HEK293T cells were cultured in Dulbecco's Modified Eagle's Medium (DMEM, Genesee Scientific) supplemented with 10% FBS (Peak Serum, PS-FB2). All cells were maintained at 37°C in 5% CO_2 and confirmed mycoplasma-free.

3.4.2 *Cell line generation*

RIT1^{M90I}, RIT1^{M90I} + sg*USP9X*, and RIT1^{M90I} + sg*RIT1* cells were generated as previously described (18). PC9-Cas9 Parental + sg*USP9X* cells were generated by co-transfecting with lipofectamine CRISPR max (Life Technologies) and a synthetic guide RNA: TCATACTATACTCATCGACA

Single cells were plated in a 96-well cell culture plate (Falcon), and clones were expanded and validated by Western blot analysis and Sanger sequencing. H2110iCas9 cells were generated as previously described (18).

PC9-Cas9 KRAS^{G12V}- and EGFR$^{T790M/L858R}$-mutant cells expressing sgNTC and sg*USP9X* were generated by transduction with pXPR003 and sgNTC or sg*USP9X* guide RNAs. Lentivirus was generated as previously described (18).

3.4.3 *Transformation and plasmid preparation*

To propagate plasmids, One Shot TOP10 Chemically Competent *E. coli* (ThermoFisher Scientific) were transformed with 1 μg of plasmid. Bacteria were propagated and plasmid was isolated using the Plasmid Plus Midi kit (Qiagen) as per the manufacturer's protocol.

3.4.4 *siRNA treatment*

Lyophilized siRNAs were ordered from Dharmacon and resuspended to make 100 μM stock solutions. For siCtrl conditions, ON-TARGETplus Non-targeting siRNA #1 was used. The sequence for si*USP9X* is as follows:

Sense: 5' ACACGAUGCUUUAGAAUUUUU 3'

Antisense: 5' PAAAUUCUAAAGCAUCGUGUUU 3'

Transfections were performed using Lipofectamine RNAiMAX (Life Technologies) following the manufacturer's protocol.

3.4.5 *Dose response curves*

For drug treatment experiments in PC9 cells, cells were plated in white-bottom 384-well plates (Falcon) at a density of 400 cells per well in 40 μL of media. For siRNA experiments, $1x10^6$ cells were plated in a 10 cm cell culture dish (ThermoFisher Scientific). 24 hours later, cells were transfected with 120 pmol of siCtrl or si*USP9X* (Dharmacon) following the Lipofectamine RNAiMAX transfection procedure (Life Technologies). 48 hours later, cells were plated in 384-well plates as described above. 24 hours after cell plating, a serial dilution of

erlotinib or osimertinib was performed using a D300e dispenser (Tecan). 72 hours post-treatment, 10 μL of CellTiterGlo reagent (Promega) was added to each well and luminescence was quantified on an Envision MultiLabel Plate Reader (PerkinElmer). The viable cell fraction was calculated by comparing the viability of drug-treated cells to the average viability of cells treated with DMSO only (Sigma-Aldrich), normalized by fluid volume. Curve fitting was performed using GraphPad Prism (v10.1.0). Inhibitors were obtained from SelleckChem: Erlotinib-OSI-774 (S1023) and Osimertinib-AZD92921 (S7297). Area-under-the curve (AUC) analyses were performed in Prism 10 (v10.0.3).

3.4.6 *Cell lysis and immunoblotting*

Whole-cell extracts for immunoblotting were prepared by washing cells with cold PBS (Corning) supplemented with phosphatase inhibitors (ThermoFisher) on ice and then scraping cells in RTK lysis buffer [20 mM Tris (pH 8.0), 2 mM EDTA (pH 8.0), 137 mM NaCl, 1% IGEPAL CA-630, 10% Glycerol, and ddH_20] supplemented with phosphatase inhibitors (ThermoFisher Scientific) and protease inhibitors (ThermoFisher Scientific, EDTA-free). Lysates were incubated on ice for 20 min. Following centrifugation (13,000 rpm for 20 min), lysates were quantified using the Pierce BCA Protein Assay Kit (ThermoFisher Scientific) in a 96-well plate and read on an Accuris Smartreader 96 (MR9600). Lysates were separated by SDS-PAGE and transferred to PVDF membranes using the Trans-blot Turbo Transfer System (BioRad). Membranes were blocked in Intercept PBS blocking buffer (LiCOR) for 1 h at room temperature followed by overnight incubation at 4°C with primary antibodies diluted in blocking buffer. IRDye (LiCOR) secondary antibodies were used for detection and were imaged on the LiCOR Odyssey DLx. Images were acquired using the Licor Acquisition Software (v1.1.0.61) from LiCOR Biosciences. Loading control and experimental proteins were probed on the same

membrane unless indicated otherwise. For clarity, loading control is shown below experimental conditions in all panels regardless of the relative molecular weights of the experimental protein(s). Quantification and normalization of Western blot band intensity was performed following protocols from Invitrogen (iBright Imaging Systems).

For immunoprecipitation experiments in Figures 4D and 4F-G: cells were lysed in EBC buffer (50 mM Tris pH 7.5, 120 mM NaCl, 0.5% NP-40/IGEPAL CA-630) supplemented with protease inhibitors (Thermo Scientific) and phosphatase inhibitors (Thermo Scientific). To prepare the Whole Cell Lysates (WCL), 3 × SDS sample buffer was directly added to the cell lysates and sonicated before being resolved on SDS-PAGE and subsequently immunoblotted with primary antibodies. The protein concentrations of the lysates were measured using the Bio-Rad protein assay reagent on a Bio-Rad Model 680 Microplate Reader. For immunoprecipitation, 1 mg lysates were incubated with the appropriate agarose-conjugated primary antibody for 3-4 h at 4°C or with unconjugated antibody (1-2 mg) overnight at 4°C followed by 1 h incubation with Protein G Sepharose beads (GE Healthcare). Immuno-complexes were washed four times with NETN buffer (20 mM Tris, pH 8.0, 100 mM NaCl, 1 mM EDTA and 0.5% NP-40) before being resolved by SDS-PAGE and immunoblotted with indicated antibodies.

Primary antibodies used for immunoblotting: β-Actin 1:1000 (Cell Signaling Technology, 4970), USP9X 1:500 (Proteintech, 55054-1-AP), RIT1 1:1000 (Abcam, Ab53720), Vinculin 1:1500 (Sigma-Aldrich, V9264), Cyclophilin A 1:1000 (Bio-Rad, VMA00535), Cas9 1:1000 (Cell Signaling Technology, 14697), CDC20 1:2000 (Santa Cruz, 13162), Tubulin 1:2000 (Sigma-Aldrich, T5168), Flag 1:2000 (Sigma-Aldrich, F1804), HA 1:2000 (Biolegend, 901503). MCL1 1:1000 (Cell Signaling Technology, 94296), EGFR 1:1000 (Cell Signaling Technology, 2232), KRAS 1:500 (Sigma-Aldrich, WH0003845M1).

3.4.7 *Proliferation assay*

PC9-Cas9 cells (Parental, RIT1^{M90I}, RIT1^{M90I} + sg*USP9X*, and RIT1^{M90I} + sg*RIT1*) were seeded in triplicate in 6-well tissue culture-treated dishes (CytoOne) at a density of 1x10^5 cells per well. Cells were counted and passaged every 2-4 days and replated at a density of 1x10^5 cells per well. Cumulative population doublings were calculated in excel, and statistical analyses were performed in Prism (v10.1.0).

3.4.8 *Soft agar assays*

For soft agar colony formation assays, 4x10^5 PC9-Cas9 cells (Parental, RIT1^{M90I}, RIT1^{M90I} + sg*USP9X*, and RIT1^{M90I} + sg*RIT1*) were suspended in 1.3 mL media and 2.7 mL 0.5% select agar (Sigma-Aldrich) in RPMI+10% FBS. 1 mL of this cell suspension was plated into 3 wells on a bottom layer of 0.5% select agar in RPMI+10% FBS in 6-well non-tissue culture treated dishes (Thermo Scientific). For soft agar inhibitor experiments, erlotinib was suspended in the top agar solution at a final concentration of 500 nM. DMSO control conditions were prepared to normalize by DMSO volume. After 10 days of growth, brightfield images were acquired on an ImageExpress (Molecular Devices) microscope using a 4x/0.2 NA objective. Fields of view were tiled in a 9x9 grid to cover the entire well with no overlap. A z-stack with 1125 μm range and 25 μm step size were acquired for each field of view and saved as a 2D minimum projection. All images were analyzed in ImageJ (1.53t) using a custom macro (available upon request). Images were excluded if they were obstructed by the 6-well plate and/or if the agar in view contained bubbles or other abnormalities.

3.4.9 *Cycloheximide-chase*

PC9-Cas9 Parental and sg*USP9X* cells treated with 100 µg/mL cycloheximide (CHX) for the indicated time periods before harvesting protein for Western blot. Cycloheximide (Tocris Bioscience, Cat. No. 0970, CAS No. 66-81-9), was dissolved in DMSO as 100 mg/ml stock solution freshly before each use.

3.4.10 *RT-qPCR*

For RT-qPCR experiments in siRNA-treated PC9 cells (parental and RIT1^{M90I}-mutant), 150,000 cells were plated in each well of a 6-well plate (CytoOne). The next day, siRNA treatment was performed as described above. 48 hours post-transfection, each well was washed with 1 mL cold PBS, and 700uL of Trizol reagent (Life Technologies) was added to each well. After 1 minute, the suspension was collected, and RNA was isolated using the Direct-Zol RNA Miniprep Plus (Zymo Research). Reverse transcription was performed with 1 µg RNA and the SuperScript IV First-Strand Synthesis System (Invitrogen). cDNA was amplified using TaqMan gene expression assays (ThermoFisher Scientific): RIT1 (assay Hs00608424_m1) and 18S (assay Hs99999901_s1). For RIT1 reactions, 30 ng of cDNA was used. For 18S reactions, 5 ng of cDNA was used. Reactions were run on the BioRad CFX384 Real-Time system and analyzed via the standard curve method.

For the H2110iCas9 RT-qPCR experiments, total RNA was extracted from two biological replicates of parental H2110iCas9 cells and H2110iCas9 + sg*USP9X* cells treated with siCtrl or si*USP9X*. Reverse transcription was performed with 1 µg RNA and the SuperScript IV First-Strand Synthesis System (Invitrogen). 20 ng of cDNA was used for each RT-PCR reaction. cDNA was amplified using TaqMan gene expression assays (ThermoFisher Scientific): RIT1 (assay Hs00608424_m1) and 18S (assay Hs99999901_s1). Reactions were run on the BioRad

CFX384 Real-Time system. Expression was normalized to 18S within each sample in the same experiment, and relative expression was quantified using the $2^{-\Delta\Delta Ct}$ method.

3.4.11 *Co-immunoprecipitation*

For $RIT1^{\sim Ub}$ pulldown, 2 million HEK293T cells were plated in 10 cm cell culture dishes (ThermoFisher Scientific). The next day, cells were transfected with 10 μg of indicated plasmids and jetPRIME reagent (Polyplus), following the manufacturer's protocol. 24 hours post-transfection, HA pulldown was performed using EZview Red Anti-HA Affinity Gel (Millipore Sigma). In brief, cells were washed with cold PBS supplemented with phosphatase inhibitors (ThermoFisher Scientific). Cells were scraped in 1 mL NP40 lysis buffer (150 mM NaCl, 1% NP40, 10% glycerol, 10mM Tris (pH 8.0), and ddH_20) supplemented with protease and phosphatase inhibitors (ThermoFisher Scientific). 50 μL of lysate was reserved for the Whole Cell Lysate. 30 μL of pre-washed EZview beads were added per condition, and samples were incubated for 2 hours at 4°C with shaking. Samples were washed 3X and then prepared for SDS-PAGE and Western blot as described above. For $RIT1^{\sim Ub}$ pull downs used for affinity purification mass spectrometry, a similar protocol was used with few substitutions. First, the number of cells was scaled up to 15 million in two 15 cm plates and magnetic anti-HA beads (ThermoFisher Scientific) were used instead. After washing beads with lysis buffer, two additional washes were performed using PBS to remove residual detergent present in the beads. For each experimental condition, four biological replicates were used.

For IP:RIT1 experiments with endogenous USP9X, 3 million HEK393T cells were plated in 10 cm cell culture dishes (ThermoFisher Scientific). The next day, cells were transfected with 2.5 μg of GST-tagged RIT1 plasmids or GFP control plasmid using Lipofectamine 3000 Reagent (ThermoFisher Scientific) following the manufacturer's protocol. 24 hours later, cells were

washed with cold PBS supplemented with phosphatase inhibitors (ThermoFisher Scientific). Cells were scraped in 700 µL lysis buffer (50mM Tris (pH 7.5), 1% IGEPAL-CA-630) supplemented with protease and phosphatase inhibitors (ThermoFisher Scientific). Protein lysates were quantified using the Pierce BCA Protein Assay Kit (ThermoFisher Scientific), and 1 mg of protein was used for each IP condition. 50 µg of protein was set aside for the Whole Cell Lysate. For IP conditions, each lysate was pre-cleared with 20 µL of pre-washed Protein A agarose beads (Cell Signaling 9863S). Next, 1 µg of RIT1 antibody (Abcam Ab53720) or 1 µg of control rabbit IgG antibody (R&D Systems AB-105-C) was added, and samples were incubated for 2 hours at 4°C with shaking. 20 µL of beads were added to each tube, and samples were incubated overnight at 4°C with shaking. The next day, samples were washed 3X and prepared for SDS-PAGE and Western blot as described above.

3.4.12 *In vitro ubiquitination assay*

HEK293T cells were transfected with RIT1, USP9X, and His-ubiquitin constructs. 36 hours after transfection, 10 µM MG132 was added to block proteasome degradation, and cells were harvested in denatured buffer (6 M guanidine-HCl, 0.1 M Na_2HPO_4/NaH_2PO_4, 10 mM imidazole), followed by Ni-NTA (Ni-nitrilotriacetic acid) purification and immunoblot analysis. MG-132 (Selleck Chemicals, Cat. No. S2619, CAS No. 1211877-36-9), was dissolved in DMSO as a 10 mM stock solution and stored in -20°C.

3.4.13 *Affinity purification/mass spectrometry*

On-bead trypsin digests were performed as previously described (26), and digested tryptic peptides were analyzed by LC-MS/MS on Orbitrap Fusion Lumos Tribrid Mass Spectrometer (Thermo Fisher Scientific) using the same configuration and settings as previously

reported (181). Acquired MS data were analyzed using a workflow previously described (80,181). Briefly, spectra were searched in Protein Prospector (version 6.2.4 (182)) against human proteome (SwissProt database downloaded on 01/18/2021) and decoy database of corresponding randomly shuffled peptides. Search engine parameters were as follows: "ESI-Q-high-res" for the instrument, trypsin as the protease, up to 2 missed cleavages allowed, Carbamidomethyl-C as constant modification, default variable modifications, up to 3 modifications per peptide allowed, 15 ppm precursor mass tolerance, and 25 ppm tolerance for fragment ions. The false discovery rate was set to <1% for peptides, and at least 3 unique peptides per protein were required. Protein Prospector search results formatted as BiblioSpec spectral library were imported into Skyline (v21) to quantify peptide and protein abundances using MS1 extracted chromatograms (183). Statistical analysis of observed protein abundances was performed using MSstats package integrated in Skyline (184).

Abundance per peptide represents the $\log_2$-abundance of the peak intensity (AUC) from mass-spectrometry for each peptide. Mean per-peptide abundance is the average enrichment of abundance for each peptide across replicates. Mean of mean-peptide abundance was calculated as the average of mean-peptide abundance for all peptides for the protein across repeats. Mean of mean-peptide abundance was used to generate the heatmap (**Figure 3.13A**). Heatmap shows a subset of those proteins with at least a 5-fold enrichment over empty vector (EV).

3.4.14 *CRISPR data analysis*

CRISPR scores were calculated as previously described (18). In brief, all data were scaled so that the median of non-essential genes (based on previously published lists in DepMap (185)) is 0 and the median of essential genes is -1. CRISPR scores were defined as this scaled,

normalized log-fold-change data. All data from this CRISPR screen are available within the main figures and supplemental information from the associated published manuscript (18).

3.4.15 *DepMap analyses*

For correlation analyses, data were explored in the Cancer Dependency Map (DepMap) online portal (https://depmap.org/portal/). Proteomics data were captured from (168) and available within DepMap. RIT1, CDC20, and USP9X expression were evaluated in the Expression Public 23Q2 datasets and previously published (169). Correlation and statistical tests were performed in Prism (v10.1.0). For the Copy Number analyses, data was obtained from the Copy Number Absolute dataset, as well as the Expression Public dataset in DepMap. USP9X CRISPR scores were obtained from DepMap Public 23Q4+Score, Chronos.

3.4.16 *Quantification and statistical analysis*

Data are expressed as mean $\pm$ s.d. unless otherwise noted. Exact numbers of biological and technical replicates for each experiment are reported in the Figure Legends. p-values less than 0.05 were considered statistically significant based on the appropriate statistical test for the experiment in question. For all data, *p<0.05, **p<0.01, ***p<0.001, ****p<0.0001. Data were analyzed using Prism Software 10.0 (GraphPad).

3.5 Acknowledgements

We would like to thank Dr. Lena Schroeder of the Fred Hutchinson Cancer Center Cellular Imaging Shared Resource for assistance with microscopy and image analysis. The wild-type and catalytically dead USP9X constructs used in ubiquitination experiments were a kind gift from Dr. Lindsey Allan at the University of Dundee and were previously published (118).

3.5.1 *Funding*

This research was funded in part through NCI F31CA271637 to A.K.R., NCI R37CA252050 and a Pardee Foundation award to A.H.B, R01CA255398 and ACS RSG-19-226-01-TBE to L.W., and ACS TLC-21-009-01-TLC to A.H.B. & L.W. This research was supported by the Cellular Imaging Shared Resource RRID:SCR_022609 of the Fred Hutch/University of Washington/Seattle Children's Cancer Consortium (P30 CA015704).

3.5.2 *Author contributions*

A.K.R., L.W., and A.H.B. conceived of and designed the study. A.K.R., M.G., and A.S. performed the cellular and biochemistry experiments. A.V. generated *RIT1*-mutant PC9-Cas9 knockout cell lines. S.M. analyzed the AP/MS data and generated associated plots. L.W. and A.S. provided panels 3E and 4D, and L.W. and M.G. provided panels 4F-G. P.C. contributed reagents. A.U. and P.C. performed AP/MS experiments and provided the associated methods. A.K.R. wrote the manuscript, which was reviewed by all co-authors.

3.5.3 *Competing interests*

The authors declare no competing interests.

3.6 DATA AND MATERIALS AVAILABILITY

Data and materials used for the USP9X/RIT1 study are outlined in **Table 3.1**.

Table 3.1. Key Resources Table.

REAGENT or RESOURCE	SOURCE	IDENTIFIER
Antibodies		
β-Actin	Cell Signaling Technology	4970
USP9X	Proteintech	55054-1-AP
RIT1	Abcam	Ab53720
Vinculin	Sigma-Aldrich	V9264
Cyclophilin A	Bio-Rad	VMA00535
Cas9	Cell Signaling Technology	14697
CDC20	Santa Cruz	13162
Tubulin	Sigma-Aldrich	T5168
Flag	Sigma-Aldrich	F1804
MCL1	Cell Signaling Technology	94296
EGFR	Cell Signaling Technology	2232
KRAS	Sigma-Aldrich	WH0003845M1
HA	Biolegend	901503
Rabbit IGG antibody	R&D Systems	AB-105-C
IRDye secondary antibodies	LiCOR	922-322/680
Bacterial and virus strains		
One Shot TOP10 Chemically Competent *E. coli*	ThermoFisher Scientific	C404010
Chemicals, peptides, and recombinant proteins		
Erlotinib-OSI-774	SelleckChem	S1023
Osimertinib-AZD92921	SelleckChem	S7297
MG132	Selleck Chemicals	Cat. No. S2619, CAS No. 1211877-36-9
Cycloheximide	Tocris Bioscience	Cat. No. 0970, CAS No. 66-81-9
Complete protease inhibitor cocktail tablets	ThermoFisher Scientific	A32955
Phosphatase inhibitor tablets	ThermoFisher Scientific	A32957
Trypsin	Corning	MT 25-053-CI
jetPRIME Reagent	Polyplus	101000027
Lipofectamine 3000 Reagent	ThermoFisher Scientific	L3000008
RNAiMAX	ThermoFisher Scientific	13778075

ANTI-FLAG M2 Affinity Gel	Millipore Sigma	A2220
EZview Red Anti-HA Affinity Gel	Millipore Sigma	E6779
Protein A agarose beads	Cell Signaling	9863S
Protein G Sepharose beads	GE Healthcare	17-0618-01
DMSO	Sigma-Aldrich	D2650
Critical commercial assays		
Pierce BCA Protein Assay Kit	ThermoFisher Scientific	23225
Bio-Rad Protein Assay Reagent	Biorad	5000001
CellTiter-Glo Luminescent Cell Viability Assay	Promega	G7572
Lipofectamine CRISPRMAX	Invitrogen	CMAX00008
SuperScript IV First-Strand Synthesis System	Invitrogen	18091050
Plasmid Plus Midi kit	Qiagen	12941
Trans-blot Turbo Transfer System	Biorad	1704274
Taqman Gene Expression Assay: RIT1	ThermoFisher Scientific	Hs00608424
Taqman Gene Expression Assay: 18S	ThermoFisher Scientific	Hs99999901_s1
Deposited data		
Proteomic data	ProteomeXchange Consortium PRIDE(186)	PXD047228
CRISPR screen	Published(18)	
Experimental models: Cell lines		
PC9	Dr. Matthew Meyerson (Broad Institute)	
NIH3T3	ATCC	CRL-1658
NCI-H2110	ATCC	CRL-5924
HEK293T	ATCC	CRL-3216
Oligonucleotides		
sg*USP9X*: TCATACTATACTCATCGACA	Synthego	
si*USP9X*: Sense: 5' A.C.A.C.G.A.U.G.C.U.U.U.A.G.A.A.U.U.U.U.U 3' Antisense: 5' 5'- P.A.A.A.U.U.C.U.A.A.A.G.C.A.U.C.G.U.G.U.U.U 3'	Dharmacon	CTM-511558
siCtrl: ON-TARGETplus Non-targeting siRNA #1	Dharmacon	D-001810-01-05
Software and algorithms		
Prism	Graphpad	v10.1.0
ImageJ	NIH	1.53t
ImageStudio	Licor	v5.2.5

Licor Acquisition Software	Licor	v1.1.0.61
Other		
DMEM	Genesee Scientific	25-500
RPMI 1640	Gibco	11875119
Fetal Bovine Serum	Peak Serum	PS-FB2
96-well cell culture plate	Falcon	353075
6-well cell culture plate	CytoOne	CC7682-7506
6-well non-treated plate	ThermoFisher Scientific	150239
10cm cell culture dish	ThermoFisher Scientific	12556002
White-bottom 384-well cell culture plate	Falcon	08-772-116
PBS	Corning	21-040-CV
Tris pH 7.5	Invitrogen	15-567-027
Tris pH 8.0	Lonza	51238
EDTA 0.5 M	Hoefer	GR123-100
NaCl 5 M	Growcells	MRGF-1207
IGEPAL CA-630	Sigma-Aldrich	18896
NP-40	GBiosciences	072N-A
Glycerol	ThermoFisher Scientific	3563501000M
Intercept PBS Blocking Buffer	LiCOR	927-70003
Select Agar	Sigma-Aldrich	A5054

3.6.1 *Lead contact*

Further information and requests for resources and reagents should be directed to and will be fulfilled by the lead contact, Dr. Alice Berger (ahberger@fredhutch.org).

3.6.2 *Materials availability*

This study did not generate new unique reagents. Reagents used in this study are commercially available or available upon request to the lead author.

3.6.3 *Data and code availability*

A) The data supporting the findings of this study are available within the article and its supplementary materials.

B) The mass spectrometry proteomics data have been deposited to the ProteomeXchange Consortium via the PRIDE(186) partner repository with the dataset identifier PXD047228.

C) Analysis of CRISPR screen data is based on a previously published manuscript(18).

D) This study did not generate code. The custom macro for image analysis is available upon request.

E) Any additional information required to reanalyze the data reported in this paper is available from the lead contact (Dr. Alice Berger, ahberger@fredhutch.org) upon request.

3.7 SUPPLEMENTAL DATA

3.7.1 *Supplemental tables*

All Supplemental Tables referenced in this chapter can be found at the following link: https://doi.org/10.1101/2023.11.30.569313

3.7.2 *Supplemental figures*

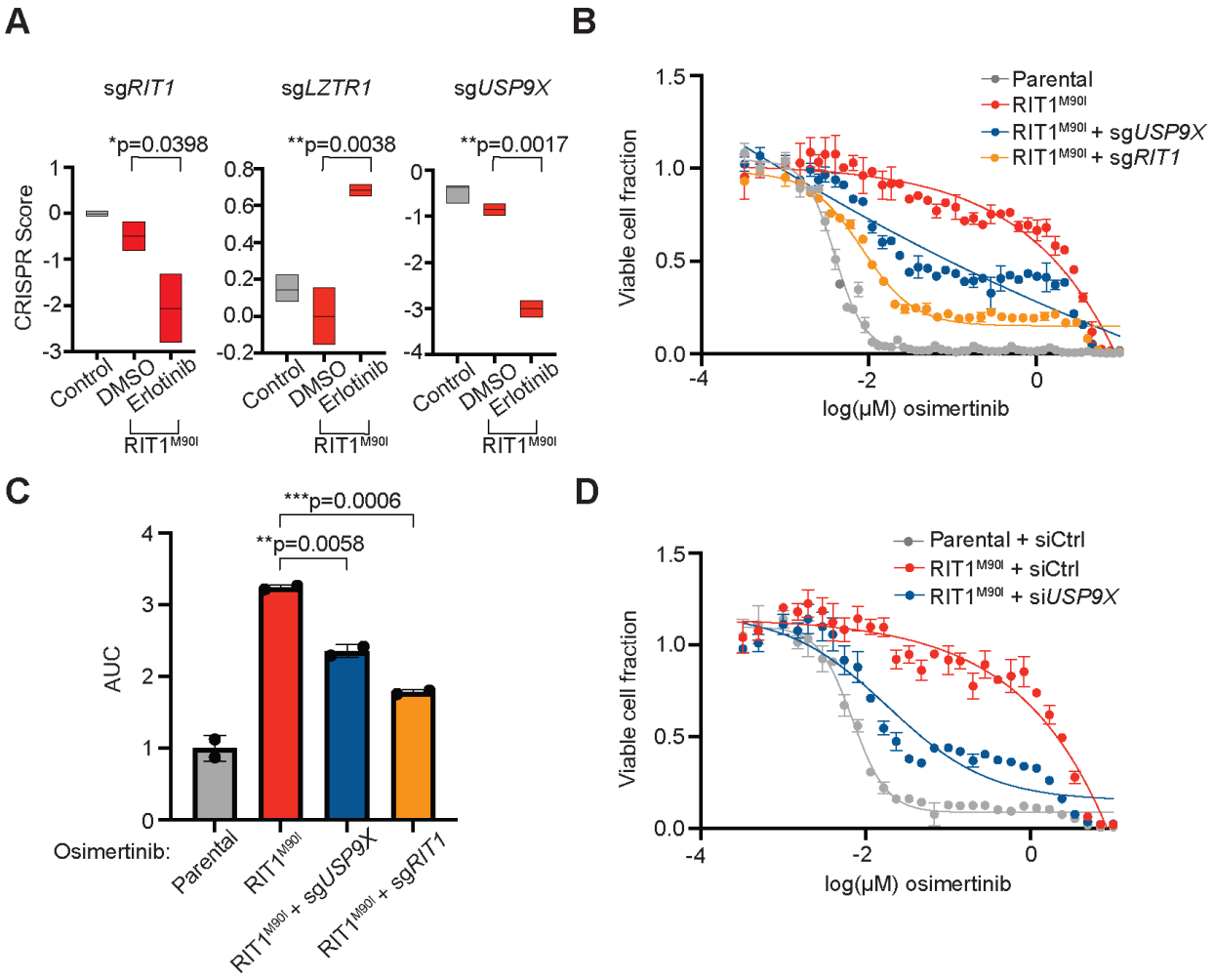

Figure 3.10. Supplementary figure associated with **Figure 3.2**.

- **A)** Box plots showing average CRISPR score of indicated sgRNAs in PC9-Cas9 Parental (+Luciferase/Control) cells or RIT1^{M90I}-mutant PC9-Cas9 cells. Box plots show the median (center line) and the min and max range of replicates. For Control conditions, n = 3 biological replicates. For RIT1^{M90I}-mutant cells, n = 2 biological replicates. p-values calculated by unpaired two-tailed t-tests.
- **B)** Dose-response curves of PC9-Cas9 Parental cells and RIT1^{M90I}-mutant PC9-Cas9 cells with indicated gene knockouts (sg*RIT1* and sg*USP9X*) treated with osimertinib for 72 hours. CellTiterGlo was used to quantify viable cell fraction determined by normalization to DMSO control. Data shown are the mean ± s.d. of two technical replicates. Data are representative results from n = 2 independent experiments.
- **C)** Area-under-the-curve (AUC) analysis of dose response curves shown in (D). p-values calculated by unpaired two-tailed t-tests.
- **D)** Dose-response curve of RIT1^{M90I}-mutant PC9 cells treated with siCtrl or si*USP9X* for 48 hours, prior to treatment with osimertinib for 72 hours. CellTiterGlo was used to quantify

viable cell fraction determined by normalization to DMSO control. Data shown are the mean $\pm$ s.d. of two technical replicates. Data are representative results from n = 3 independent experiments.

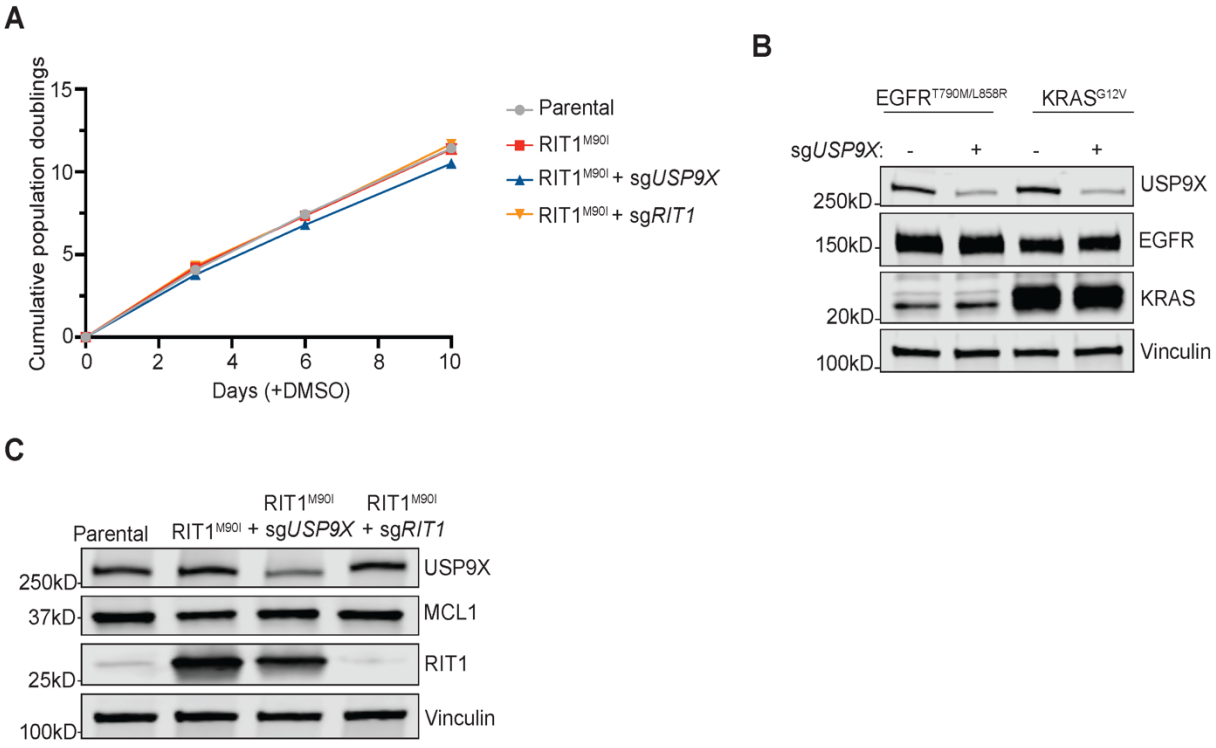

Figure 3.11. Supplementary figure associated with Figure 3.3.

A) Proliferation of PC9-Cas9 Parental cells and RIT1^{M90I}-mutant PC9-Cas9 cells with indicated gene knockouts (sg*RIT1* and sg*USP9X*) treated with DMSO (vehicle). Data shown are the mean $\pm$ s.d. of three technical replicates per cell line. Data are representative results from n = 2 independent experiments. p-value calculated by multiple unpaired two-tailed t-tests.

B) Western blot of *EGFR*- and *KRAS*-mutant PC9-Cas9 cells with or without sg*USP9X*. "-" lanes represent cells harboring sgNTC. Vinculin serves as a loading control.

C) Western blot of parental and RIT1^{M90I}-mutant PC9 cells with sg*USP9X* or sg*RIT1*. Vinculin serves as a loading control.

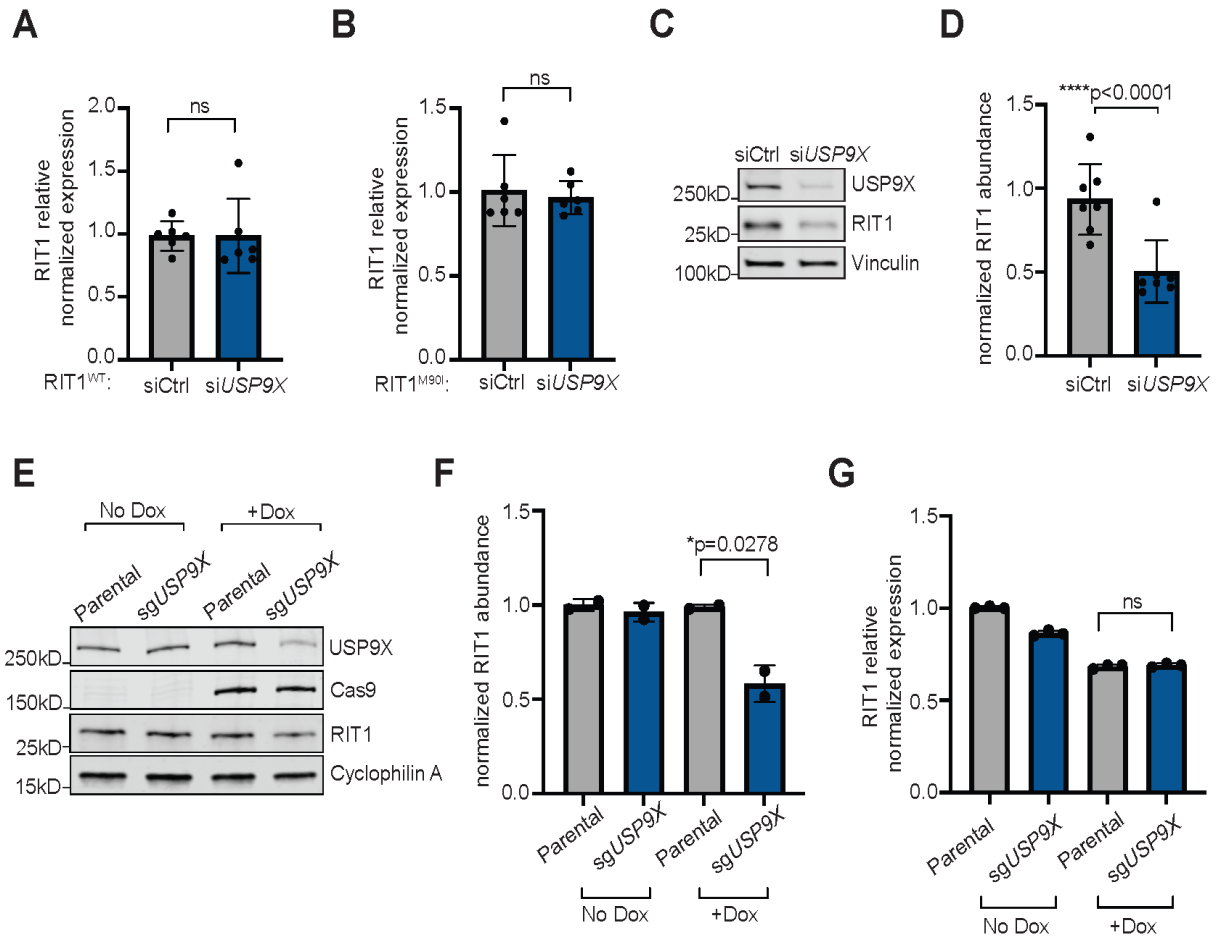

Figure 3.12. Supplementary figure associated with Figure 3.4.

A) Relative expression of *RIT1* as determined by qPCR and standard curve-based quantification. Parental PC9 cells were treated with siCtrl or si*USP9X* for 48 hours before RNA collection. Relative normalized expression calculated by BioRad software. Each dot represents a biological replicate (individual cDNA preparations). Each qPCR sample was run in triplicate for housekeeping (18S) and RIT1 probes.

B) Relative expression of *RIT1* as determined by qPCR and standard curve-based quantification. RIT1^{M90I}-mutant PC9 cells were treated with siCtrl or si*USP9X* for 48 hours before RNA collection. Relative normalized expression calculated by BioRad software. Each dot represents a biological replicate (individual cDNA preparations). Each qPCR sample was run in triplicate for housekeeping (18S) and RIT1 probes.

C) Western blot of NCI-H2110 cells treated with indicated siRNAs for 72 hours. Vinculin serves as a loading control.

D) Quantification of Western blot bands based on (A) and additional replicates. Data shown are the mean ± s.d. of three independent experiments with 2-3 technical replicates per condition. p-value calculated by paired two-tailed t-test.

E) Western blot of NCI-H2110iCas9 cells treated with 1 μg/mL Dox for 7 days to induce Cas9 expression. Cyclophilin A serves as a loading control.

F) Quantification of Western blot bands in (C). Data shown are the mean ± s.d. of two independent experiments. p-value calculated by paired two-tailed t-test.

G) Relative expression of *RIT1* as determined by qPCR and ΔΔCt analysis. Data shown are the mean ± s.d. of three technical replicates per condition. Data are representative of results from n = 2 independent experiments. ns = not significant by paired two-tailed t-test.

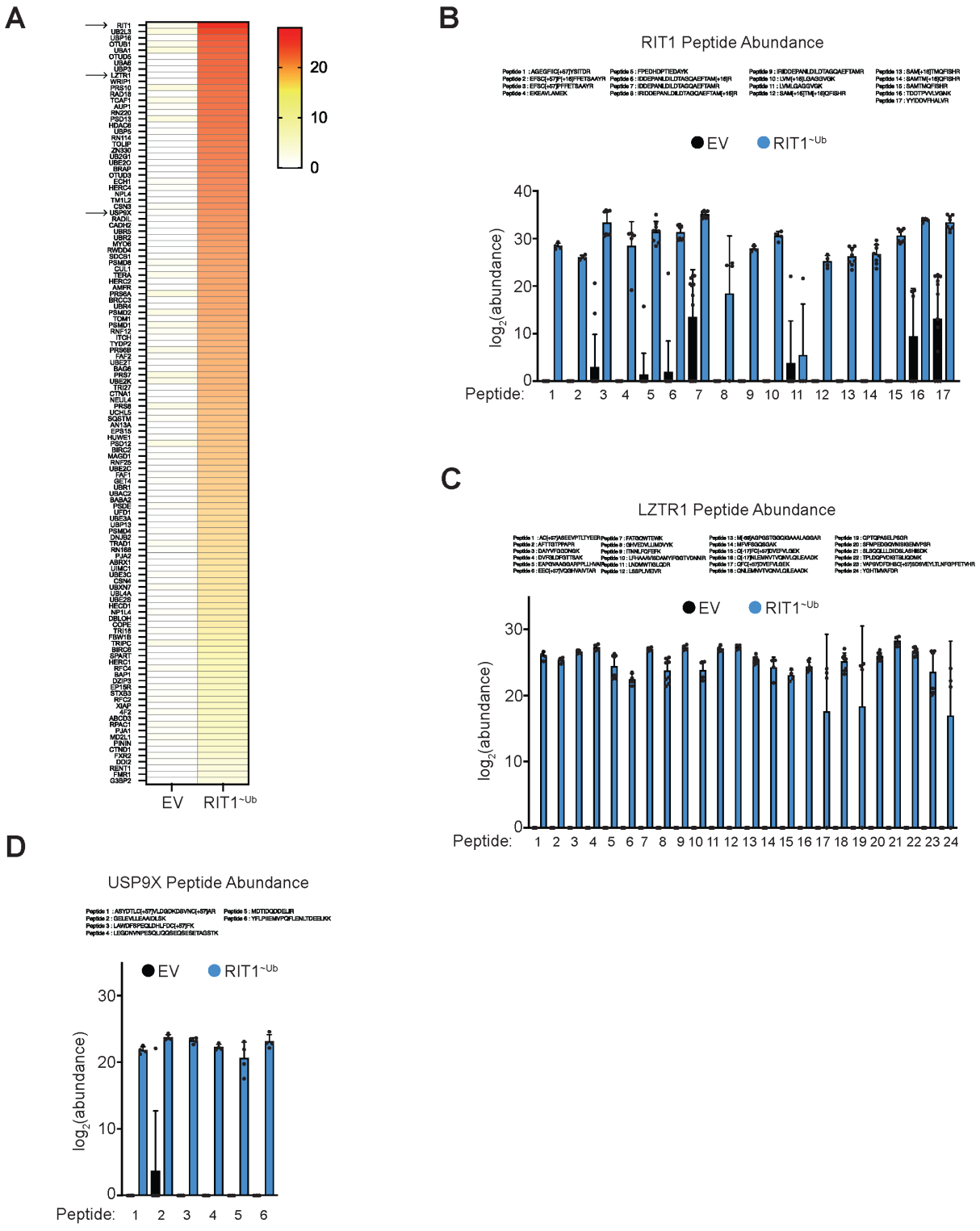

Figure 3.13. Supplementary figure associated with Figure 3.7.

A) Heatmap of peptides detected in affinity purification/mass spectrometry (AP/MS) experiment. Data were filtered for proteins that were at least 5 times higher in RIT1$^{\sim Ub}$ condition compared to EV (Empty Vector). Abundance values are the $\log_2$-based number

of the peak intensity from the MS. The mean of all peptides was combined across biological replicates. For EV samples, n = 7 biological replicates. For RIT1$^{\sim Ub}$ samples, n = 4 biological replicates.

B) Abundance (log_2-transformed) of individual RIT1 peptides in Empty Vector (EV) control and RIT1$^{\sim Ub}$ conditions from AP/MS.

C) Abundance (log_2-transformed) of individual LZTR1 peptides in EV and RIT1$^{\sim Ub}$ conditions from AP/MS.

D) Abundance (log_2-transformed) of individual USP9X peptides in EV and RIT1$^{\sim Ub}$ conditions from AP/MS. For B-D, some peptides were detected in all replicates while other peptides were only detected in some replicates.

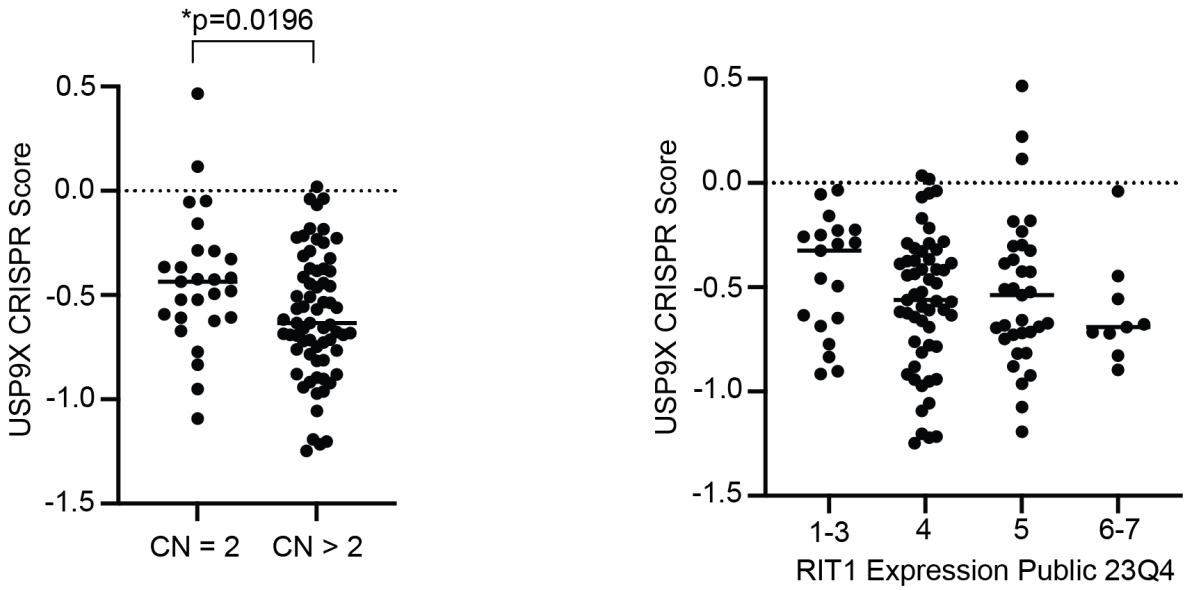

Figure 3.14. Supplementary figure associated with Figure 3.8.

A) Data from the Cancer Dependency Map (DepMap) comparing the CRISPR score of USP9X (DepMap Public 23Q4+ Score, Chronos) in lung cancer cells with normal copy number of RIT1 (CN = 1) versus cells with high copy number of RIT1 (CN > 1). Copy Number data were based on the Copy Number (Absolute) data set. p-value calculated by unpaired two-tailed t-test.

B) DepMap data comparing the CRISPR score of USP9X (DepMap Public 23Q4+ Score, Chronos) to RIT1 expression in the Expression Public 23Q4 dataset. For visualization purposes, cell lines were binned based on indicated ranges.

Chapter 4. DISCUSSION

4.1 CONCLUSIONS

In summary, my dissertation research has expanded our knowledge of RIT1 biology and protein regulation. This project began with analysis and publication of the Berger Lab's CRISPR screen data in PC9 lung adenocarcinoma cells. From that work, I explored the role of RIT1 in the Spindle Assembly Checkpoint (SAC) and found that mutant RIT1 weakens the SAC, rendering cells vulnerable to loss of SAC genes. This added to other research in the field showing that RIT1 comprises mitotic fidelity and promotes the accumulation of chromosomal abnormalities. I focused the remainder of my dissertation research on identifying novel therapeutic targets in *RIT1*-driven non-small cell lung cancer.

Through my dissertation work, I have identified the deubiquitinase USP9X as a positive regulator of both wild-type and mutant RIT1. This builds upon previous studies showing that the cullin 3 RING E3 ligase and the adaptor protein LZTR1 bind and ubiquitinate wild-type—but not mutant—RIT1. To date, USP9X is the first RIT1 deubiquitinase that has been characterized. Although my work focused on non-small cell lung cancer, analysis of cancer cell lines within the Cancer Dependency Map revealed a positive correlation between RIT1 protein abundance and USP9X. This suggests that my findings could be applicable across numerous cancer types driven by *RIT1* mutations and amplifications.

Of note, I acknowledge that my findings related to RIT1's mitotic perturbation and RIT1 as a USP9X substrate are not necessarily mutually exclusive. During mitosis, USP9X could be stabilizing RIT1, promoting the formation of RIT1/MAD2/p31^{comet} complexes. This would accelerate progression through mitosis and weaken the SAC, as is observed in *RIT1*-mutant cells.

Although this is possible, it appears to be in contradiction to the observation that USP9X strengthens the SAC by preventing the degradation of CDC20 (118). There are a few possible explanations to resolve these apparent contradictions. First, USP9X-mediated regulation of RIT1 might only occur outside of mitosis. During the cell cycle, modifications such as phosphorylation could dictate USP9X's substrate specificity and may direct it to CDC20 over RIT1. Indeed, phosphorylation has been shown to alter USP9X's activity (149). Another possibility is that, in lung cancer cells, USP9X preferentially binds RIT1 over other substrates. Although our work suggests that CDC20 is also a USP9X substrate in PC9 cells (**Figure 3.4E**), this has not been explored in mitotic cells. To resolve these possibilities, it will be important to conduct experiments in mitotic PC9 cells to ascertain if USP9X is binding to and deubiquitinating RIT1 during mitosis.

Altogether, my dissertation work adds to our understanding of RIT1 biology and the importance of RIT1 protein regulation in disease states. My research also opens opportunities to explore USP9X-mediated RIT1 regulation in other cancers and investigate the potential preclinical utility of USP9X inhibitors.

4.2 BROADER IMPACT

Ten years ago, *RIT1* was identified as an oncogene in lung cancer. Since then, somatic *RIT1* alterations have been found in a diverse range of cancer types, including hepatocellular carcinoma, endometrial cancer, and myeloid malignancies. Understanding RIT1 in cancer has been particularly challenging given that 1) we know very little about RIT1 function and 2) few model systems exist to allow us to study RIT1 in the lab.

In the face of these challenges, the Berger Lab developed a novel screening approach in PC9 lung adenocarcinoma cells to probe essential genes underlying RIT1 function. This

screening system is based on the observation that expression of $RIT1^{M90I}$ confers resistance to EGFR inhibition. This PC9 screening system also has important implications for other oncogenes that confer resistance to EGFR tyrosine kinase inhibitors. We have already published CRISPR screen results in erlotinib-resistant *KRAS*- and *EGFR*-mutant PC9 cells, and our screening system can also be used to understand oncogene-driven drug resistance in other cellular contexts. For example, over-activation of the PI3K/AKT/mTOR pathway is known to confer EGFR inhibitor resistance (187), and our PC9 system could be used to understand genetic dependencies underlying these resistance mechanisms. This information could nominate genes as novel therapeutic targets to mitigate drug resistance.

Of note, it is important to acknowledge the limitations of targeted therapies in cancer treatment. In general, targeted therapies are an improvement over cytotoxic chemotherapy because targeted therapies are designed to only kill transformed cells while ensuring that normal, healthy cells remain viable. Many side-effects of chemotherapy—namely hair loss and gastrointestinal discomfort—are primarily caused by the effects of chemotherapy on fast-dividing, non-cancer cells. Targeted therapies are designed to reduce these effects and more efficiently kill tumor cells. Despite this, small molecule inhibitors can be difficult to design. In the context of deubiquitinases (DUBs), this remains a complex challenge given the number of DUBs in human cells (over 100) and the fact that many of these DUBs show high sequence homology. Because of this, a small molecule DUB inhibitor is likely to inhibit at least more than one DUB family member. This has been an issue in the development of USP9X inhibitors, and even the newest inhibitors bind other targets. Despite this, an inhibitor that only binds one target is unlikely to exist. Instead, it is important to determine that any off-target effects do not negatively affect the viability of non-transformed cells. Nevertheless, the discovery of USP9X as

a novel RIT1 regulator represents one of the most promising therapeutic targets to date for cancers driven by *RIT1* mutations and amplifications.

Moving forward, research into oncogenic *RIT1* amplifications is crucial. Tumor sequencing studies have found *RIT1* amplifications across many cancer types, and studies have found that *RIT1* over-expression phenocopies mutant *RIT1* expression. These findings are in concordance with the hypothesis that RIT1 protein abundance is important for its function. My dissertation work presents USP9X as an essential gene for maintaining the abundance—and potential oncogenicity—of wild-type RIT1.

Over the course of my dissertation research, I have applied my skills in biochemistry and molecular biology to undercover novel mechanisms of oncogenic RIT1 protein regulation. I acknowledge that there are many steps ahead to translate this work to clinical outcomes. Despite this, I recognize the importance of my contributions, both for expanding our understanding of RIT1 biology and for nominating new therapeutic targets in *RIT1*-driven diseases. I hope that my work can inspire more research focused on RIT1 oncogenic mechanisms and that this knowledge can be used to develop new therapies and improve patient outcomes.

BIBLIOGRAPHY

1. Sung H, Ferlay J, Siegel RL, Laversanne M, Soerjomataram I, Jemal A, et al. Global Cancer Statistics 2020: GLOBOCAN Estimates of Incidence and Mortality Worldwide for 36 Cancers in 185 Countries. CA Cancer J Clin. 2021 May;71(3):209–49.

2. Cancer Genome Atlas Research Network. Comprehensive molecular profiling of lung adenocarcinoma. Nature. 2014 Jul 31;511(7511):543–50.

3. Trahey M, McCormick F. A cytoplasmic protein stimulates normal N-ras p21 GTPase, but does not affect oncogenic mutants. Science. 1987 Oct 23;238(4826):542–5.

4. Cox AD, Der CJ. Ras history: The saga continues. Small GTPases. 2010 Jul;1(1):2–27.

5. Simanshu DK, Nissley DV, McCormick F. RAS Proteins and Their Regulators in Human Disease. Cell. 2017 Jun 29;170(1):17–33.

6. Campbell SL, Khosravi-Far R, Rossman KL, Clark GJ, Der CJ. Increasing complexity of Ras signaling. Oncogene. 1998 Sep 17;17(11 Reviews):1395–413.

7. Shao H, Kadono-Okuda K, Finlin BS, Andres DA. Biochemical characterization of the Ras-related GTPases Rit and Rin. Arch Biochem Biophys. 1999 Nov 15;371(2):207–19.

8. Lee CH, Della NG, Chew CE, Zack DJ. Rin, a neuron-specific and calmodulin-binding small G-protein, and Rit define a novel subfamily of ras proteins. J Neurosci. 1996 Nov 1;16(21):6784–94.

9. Berger AH, Imielinski M, Duke F, Wala J, Kaplan N, Shi G-X, et al. Oncogenic RIT1 mutations in lung adenocarcinoma. Oncogene. 2014 Aug 28;33(35):4418–23.

10. Xu F, Sun S, Yan S, Guo H, Dai M, Teng Y. Elevated expression of RIT1 correlates with poor prognosis in endometrial cancer. Int J Clin Exp Pathol. 2015 Sep 1;8(9):10315–24.

11. Gómez-Seguí I, Makishima H, Jerez A, Yoshida K, Przychodzen B, Miyano S, et al. Novel recurrent mutations in the RAS-like GTP-binding gene RIT1 in myeloid malignancies. Leukemia. 2013 Sep;27(9):1943–6.

12. Harada G, Yang S-R, Cocco E, Drilon A. Rare molecular subtypes of lung cancer. Nat Rev Clin Oncol. 2023 Apr;20(4):229–49.

13. Siegel RL, Miller KD, Wagle NS, Jemal A. Cancer statistics, 2023. CA Cancer J Clin. 2023 Jan;73(1):17–48.

14. Reuther GW, Der CJ. The Ras branch of small GTPases: Ras family members don’t fall far from the tree. Curr Opin Cell Biol. 2000 Apr;12(2):157–65.

15. Santos E, Tronick SR, Aaronson SA, Pulciani S, Barbacid M. T24 human bladder carcinoma oncogene is an activated form of the normal human homologue of BALB- and Harvey-MSV transforming genes. Nature. 1982 Jul 22;298(5872):343–7.

16. Parada LF, Tabin CJ, Shih C, Weinberg RA. Human EJ bladder carcinoma oncogene is homologue of Harvey sarcoma virus ras gene. Nature. 1982 Jun 10;297(5866):474–8.

17. Der CJ, Krontiris TG, Cooper GM. Transforming genes of human bladder and lung carcinoma cell lines are homologous to the ras genes of Harvey and Kirsten sarcoma viruses. Proc Natl Acad Sci U S A. 1982 Jun;79(11):3637–40.

18. Vichas A, Riley AK, Nkinsi NT, Kamlapurkar S, Parrish PCR, Lo A, et al. Integrative oncogene-dependency mapping identifies RIT1 vulnerabilities and synergies in lung cancer. Nat Commun. 2021 Aug 9;12(1):4789.

19. Molina JR, Adjei AA. The Ras/Raf/MAPK pathway. J Thorac Oncol. 2006 Jan;1(1):7–9.

20. Mitin N, Rossman KL, Der CJ. Signaling interplay in Ras superfamily function. Curr Biol. 2005 Jul 26;15(14):R563-74.

21. Zenonos K, Kyprianou K. RAS signaling pathways, mutations and their role in colorectal cancer. World J Gastrointest Oncol. 2013 May 15;5(5):97–101.

22. Berger AH, Brooks AN, Wu X, Shrestha Y, Chouinard C, Piccioni F, et al. High-throughput Phenotyping of Lung Cancer Somatic Mutations. Cancer Cell. 2016 Aug 8;30(2):214–28.

23. Meyer Zum Büschenfelde U, Brandenstein LI, von Elsner L, Flato K, Holling T, Zenker M, et al. RIT1 controls actin dynamics via complex formation with RAC1/CDC42 and PAK1. PLoS Genet. 2018 May;14(5):e1007370.

24. Sakabe K, Teramoto H, Zohar M, Behbahani B, Miyazaki H, Chikumi H, et al. Potent transforming activity of the small GTP-binding protein Rit in NIH 3T3 cells: evidence for a role of a p38gamma-dependent signaling pathway. FEBS Lett. 2002 Jan 30;511(1–3):15–20.

25. Hoshino M, Yoshimori T, Nakamura S. Small GTPase proteins Rin and Rit Bind to PAR6 GTP-dependently and regulate cell transformation. J Biol Chem. 2005 Jun 17;280(24):22868–74.

26. Castel P, Cheng A, Cuevas-Navarro A, Everman DB, Papageorge AG, Simanshu DK, et al. RIT1 oncoproteins escape LZTR1-mediated proteolysis. Science. 2019 Mar 15;363(6432):1226–30.

27. Burge RA, Hobbs GA. Chapter Two - Not all RAS mutations are equal: A detailed review of the functional diversity of RAS hot spot mutations. In: O'Bryan JP, Piazza GA, editors. Advances in Cancer Research. Academic Press; 2022. p. 29–61.

28. Eccleston JF, Moore KJ, Morgan L, Skinner RH, Lowe PN. Kinetics of interaction between normal and proline 12 Ras and the GTPase-activating proteins, p120-GAP and neurofibromin. The significance of the intrinsic GTPase rate in determining the transforming ability of ras. J Biol Chem. 1993 Dec 25;268(36):27012–9.

29. Scheffzek K, Ahmadian MR, Wiesmüller L, Kabsch W, Stege P, Schmitz F, et al. Structural analysis of the GAP-related domain from neurofibromin and its implications. EMBO J. 1998 Aug 3;17(15):4313–27.

30. Rusyn EV, Reynolds ER, Shao H, Grana TM, Chan TO, Andres DA, et al. Rit, a non-lipid-modified Ras-related protein, transforms NIH3T3 cells without activating the ERK, JNK, p38 MAPK or PI3K/Akt pathways. Oncogene. 2000 Sep 28;19(41):4685–94.

31. Shi G-X, Andres DA. Rit contributes to nerve growth factor-induced neuronal differentiation via activation of B-Raf-extracellular signal-regulated kinase and p38 mitogen-activated protein kinase cascades. Mol Cell Biol. 2005 Jan;25(2):830–46.

32. Shi G-X, Rehmann H, Andres DA. A novel cyclic AMP-dependent Epac-Rit signaling pathway contributes to PACAP38-mediated neuronal differentiation. Mol Cell Biol. 2006 Dec;26(23):9136–47.

33. Aoki Y, Niihori T, Banjo T, Okamoto N, Mizuno S, Kurosawa K, et al. Gain-of-function mutations in RIT1 cause Noonan syndrome, a RAS/MAPK pathway syndrome. Am J Hum Genet. 2013 Jul 11;93(1):173–80.

34. Chen S, Vedula RS, Cuevas-Navarro A, Lu B, Hogg SJ, Wang E, et al. Impaired Proteolysis of Noncanonical RAS Proteins Drives Clonal Hematopoietic Transformation. Cancer Discov. 2022 Oct 5;12(10):2434–53.

35. Cuevas-Navarro A, Rodriguez-Muñoz L, Grego-Bessa J, Cheng A, Rauen KA, Urisman A, et al. Cross-species analysis of LZTR1 loss-of-function mutants demonstrates dependency to RIT1 orthologs. Elife [Internet]. 2022 Apr 25;11. Available from: http://dx.doi.org/10.7554/eLife.76495

36. Shi G-X, Cai W, Andres DA. Rit subfamily small GTPases: regulators in neuronal differentiation and survival. Cell Signal. 2013 Oct;25(10):2060–8.

37. Chan JJ, Flatters D, Rodrigues-Lima F, Yan J, Thalassinos K, Katan M. Comparative analysis of interactions of RASSF1-10. Adv Biol Regul. 2013 May;53(2):190–201.

38. Donninger H, Schmidt ML, Mezzanotte J, Barnoud T, Clark GJ. Ras signaling through RASSF proteins. Semin Cell Dev Biol. 2016 Oct;58:86–95.

39. Rezaei Adariani S, Kazemein Jasemi NS, Bazgir F, Wittich C, Amin E, Seidel CAM, et al. A comprehensive analysis of RAS-effector interactions reveals interaction hotspots and new binding partners. J Biol Chem. 2021 Apr 28;296:100626.

40. Leevers SJ, Paterson HF, Marshall CJ. Requirement for Ras in Raf activation is overcome by targeting Raf to the plasma membrane. Nature. 1994 Jun 2;369(6479):411–4.

41. Stokoe D, Macdonald SG, Cadwallader K, Symons M, Hancock JF. Activation of Raf as a result of recruitment to the plasma membrane. Science. 1994 Jun 3;264(5164):1463–7.

42. Terrell EM, Morrison DK. Ras-Mediated Activation of the Raf Family Kinases. Cold Spring Harb Perspect Med [Internet]. 2019 Jan 2;9(1). Available from: http://dx.doi.org/10.1101/cshperspect.a033746

43. Heo WD, Inoue T, Park WS, Kim ML, Park BO, Wandless TJ, et al. PI(3,4,5)P_3 and PI(4,5)P_2 Lipids Target Proteins with Polybasic Clusters to the Plasma Membrane. Science. 2006;314(5804):1458–61.

44. Cuevas-Navarro A, Wagner M, Van R, Swain M, Mo S, Columbus J, et al. RAS-dependent RAF-MAPK hyperactivation by pathogenic RIT1 is a therapeutic target in Noonan syndrome-associated cardiac hypertrophy. Sci Adv. 2023 Jul 14;9(28):eadf4766.

45. Migliori AD, Patel LA, Neale C. The RIT1 C-terminus associates with lipid bilayers via charge complementarity. Comput Biol Chem. 2021 Apr;91:107437.

46. Li L, He L, Wu B, Yu C, Zhao H, Zhou Y, et al. Structural Determinants for Light-Dependent Membrane Binding of a Photoswitchable Polybasic Domain. ACS Synth Biol. 2021 Mar 19;10(3):542–51.

47. Fang Z, Marshall CB, Yin JC, Mazhab-Jafari MT, Gasmi-Seabrook GMC, Smith MJ, et al. Biochemical Classification of Disease-associated Mutants of RAS-like Protein Expressed in Many Tissues (RIT1). J Biol Chem. 2016 Jul 22;291(30):15641–52.

48. Lo A, Holmes K, Kamlapurkar S, Mundt F, Moorthi S, Fung I, et al. Multiomics characterization of oncogenic signaling mediated by wild-type and mutant RIT1. Sci Signal. 2021 Nov 30;14(711):eabc4520.

49. Lo A, McSharry M, Berger AH. Oncogenic KRAS alters splicing factor phosphorylation and alternative splicing in lung cancer. BMC Cancer. 2022 Dec 16;22(1):1315.

50. Riley AK, Berger AH. Genome-wide CRISPR screening reveals novel therapeutic targets in RIT1-driven lung cancer. Mol Cell Oncol. 2021 Nov 16;8(6):2000318.

51. Paez JG, Jänne PA, Lee JC, Tracy S, Greulich H, Gabriel S, et al. EGFR mutations in lung cancer: correlation with clinical response to gefitinib therapy. Science. 2004 Jun 4;304(5676):1497–500.

52. Lynch TJ, Bell DW, Sordella R, Gurubhagavatula S, Okimoto RA, Brannigan BW, et al. Activating mutations in the epidermal growth factor receptor underlying responsiveness of non-small-cell lung cancer to gefitinib. N Engl J Med. 2004 May 20;350(21):2129–39.

53. Koga T, Suda K, Mitsudomi T. Utility of the Ba/F3 cell system for exploring on-target mechanisms of resistance to targeted therapies for lung cancer. Cancer Sci. 2022 Mar;113(3):815–27.

54. Daley GQ, Baltimore D. Transformation of an interleukin 3-dependent hematopoietic cell line by the chronic myelogenous leukemia-specific P210bcr/abl protein. Proc Natl Acad Sci U S A. 1988 Dec;85(23):9312–6.

55. Pich O, Reyes-Salazar I, Gonzalez-Perez A, Lopez-Bigas N. Discovering the drivers of clonal hematopoiesis. Nat Commun. 2022 Jul 23;13(1):4267.

56. Li Q, Haigis KM, McDaniel A, Harding-Theobald E, Kogan SC, Akagi K, et al. Hematopoiesis and leukemogenesis in mice expressing oncogenic NrasG12D from the endogenous locus. Blood. 2011 Feb 10;117(6):2022–32.

57. Van Meter MEM, Díaz-Flores E, Archard JA, Passegué E, Irish JM, Kotecha N, et al. K-RasG12D expression induces hyperproliferation and aberrant signaling in primary hematopoietic stem/progenitor cells. Blood. 2007 May 1;109(9):3945–52.

58. Cavé H, Caye A, Ghedira N, Capri Y, Pouvreau N, Fillot N, et al. Mutations in RIT1 cause Noonan syndrome with possible juvenile myelomonocytic leukemia but are not involved in acute lymphoblastic leukemia. Eur J Hum Genet. 2016 Aug;24(8):1124–31.

59. Zhao F, Bosler DS, Cook JR. Designing Myeloid Gene Panels. Arch Pathol Lab Med. 2022 Aug 1;146(8):1004–11.

60. Clara JA, Sallman DA, Padron E. Clinical management of myelodysplastic syndrome/myeloproliferative neoplasm overlap syndromes. Cancer Biol Med. 2016 Sep;13(3):360–72.

61. McCoach CE, Le AT, Gowan K, Jones K, Schubert L, Doak A, et al. Resistance Mechanisms to Targeted Therapies in ROS1+ and ALK+ Non-small Cell Lung Cancer. Clin Cancer Res. 2018 Jul 15;24(14):3334–47.

62. Sun L, Xi S, Zhou Z, Zhang F, Hu P, Cui Y, et al. Elevated expression of RIT1 hyperactivates RAS/MAPK signal and sensitizes hepatocellular carcinoma to combined treatment with sorafenib and AKT inhibitor. Oncogene. 2022 Jan;41(5):732–44.

63. Li J-T, Liu W, Kuang Z-H, Chen H-K, Li D-J, Feng Q-S, et al. [Amplification of RIT1 in hepatocellular carcinoma and its clinical significance]. Ai Zheng. 2003 Jul;22(7):695–9.

64. Mohanta S, Sekhar Khora S, Suresh A. Cancer Stem Cell based molecular predictors of tumor recurrence in Oral squamous cell carcinoma. Arch Oral Biol. 2019 Mar;99:92–106.

65. Song Z, Liu T, Chen J, Ge C, Zhao F, Zhu M, et al. HIF-1α-induced RIT1 promotes liver cancer growth and metastasis and its deficiency increases sensitivity to sorafenib. Cancer Lett. 2019 Sep 28;460:96–107.

66. Khalil A, Nemer G. The potential oncogenic role of the RAS-like GTP-binding gene RIT1 in glioblastoma. Cancer Biomark. 2020;29(4):509–19.

67. Che M, Lan Q. RIT1 Promotes Glioma Proliferation and Invasion via the AKT/ERK/NF-κB Signaling Pathway. J Mol Neurosci. 2022 Aug;72(8):1547–56.

68. Li N, Zhan X. Machine Learning Identifies Pan-Cancer Landscape of Nrf2 Oxidative Stress Response Pathway-Related Genes. Oxid Med Cell Longev. 2022 Feb 17;2022:8450087.

69. Feng Y-F, Lei Y-Y, Lu J-B, Xi S-Y, Zhang Y, Huang Q-T, et al. RIT1 suppresses esophageal squamous cell carcinoma growth and metastasis and predicts good prognosis. Cell Death Dis. 2018 Oct 22;9(11):1085.

70. Paladino A, D'Angelo F, Noviello TMR, Iavarone A, Ceccarelli M. Structural Model for Recruitment of RIT1 to the LZTR1 E3 Ligase: Evidences from an Integrated Computational Approach. J Chem Inf Model. 2021 Apr 26;61(4):1875–88.

71. Bigenzahn JW, Collu GM, Kartnig F, Pieraks M, Vladimer GI, Heinz LX, et al. LZTR1 is a regulator of RAS ubiquitination and signaling. Science. 2018 Dec 7;362(6419):1171–7.

72. Steklov M, Pandolfi S, Baietti MF, Batiuk A, Carai P, Najm P, et al. Mutations in LZTR1 drive human disease by dysregulating RAS ubiquitination. Science. 2018 Dec 7;362(6419):1177–82.

73. Abe T, Umeki I, Kanno S-I, Inoue S-I, Niihori T, Aoki Y. LZTR1 facilitates polyubiquitination and degradation of RAS-GTPases. Cell Death Differ. 2020 Mar;27(3):1023–35.

74. Riley AK, Grant M, Snell A, Vichas A, Moorthi S, Urisman A, et al. The deubiquitinase USP9X regulates RIT1 protein abundance and oncogenic phenotypes [Internet]. bioRxiv. 2023 [cited 2024 Jan 5]. p. 2023.11.30.569313. Available from: https://www.biorxiv.org/content/10.1101/2023.11.30.569313v1

75. Hanahan D. Hallmarks of Cancer: New Dimensions. Cancer Discov. 2022 Jan;12(1):31–46.

76. Gordon DJ, Resio B, Pellman D. Causes and consequences of aneuploidy in cancer. Nat Rev Genet. 2012 Jan 24;13(3):189–203.

77. Geurts van Kessel A. The cancer genome: from structure to function. Cell Oncol . 2014 Jun;37(3):155–65.

78. Holland AJ, Cleveland DW. Boveri revisited: chromosomal instability, aneuploidy and tumorigenesis. Nat Rev Mol Cell Biol. 2009 Jul;10(7):478–87.

79. Simonetti G, Bruno S, Padella A, Tenti E, Martinelli G. Aneuploidy: Cancer strength or vulnerability? Int J Cancer. 2019 Jan 1;144(1):8–25.

80. Cuevas-Navarro A, Van R, Cheng A, Urisman A, Castel P, McCormick F. The RAS GTPase RIT1 compromises mitotic fidelity through spindle assembly checkpoint suppression. Curr Biol. 2021 Sep 13;31(17):3915-3924.e9.

81. Su Y, Lin H, Yu J, Mao L, Jin W, Liu T, et al. RIT1 regulates mitosis and promotes proliferation by interacting with SMC3 and PDS5 in hepatocellular carcinoma. J Exp Clin Cancer Res. 2023 Nov 29;42(1):326.

82. Musacchio A. The Molecular Biology of Spindle Assembly Checkpoint Signaling Dynamics. Curr Biol. 2015 Oct 19;25(20):R1002-18.

83. Primorac I, Musacchio A. Panta rhei: the APC/C at steady state. J Cell Biol. 2013 Apr 15;201(2):177–89.

84. Hagan RS, Manak MS, Buch HK, Meier MG, Meraldi P, Shah JV, et al. p31(comet) acts to ensure timely spindle checkpoint silencing subsequent to kinetochore attachment. Mol Biol Cell. 2011 Nov;22(22):4236–46.

85. Zhang J, Shi X, Li Y, Kim B-J, Jia J, Huang Z, et al. Acetylation of Smc3 by Eco1 is required for S phase sister chromatid cohesion in both human and yeast. Mol Cell. 2008 Jul 11;31(1):143–51.

86. Chan K-L, Gligoris T, Upcher W, Kato Y, Shirahige K, Nasmyth K, et al. Pds5 promotes and protects cohesin acetylation. Proc Natl Acad Sci U S A. 2013 Aug 6;110(32):13020–5.

87. Wagner EF, Nebreda AR. Signal integration by JNK and p38 MAPK pathways in cancer development. Nat Rev Cancer. 2009 Aug;9(8):537–49.

88. D'Autréaux B, Toledano MB. ROS as signalling molecules: mechanisms that generate specificity in ROS homeostasis. Nat Rev Mol Cell Biol. 2007 Oct;8(10):813–24.

89. Cai W, Rudolph JL, Harrison SMW, Jin L, Frantz AL, Harrison DA, et al. An evolutionarily conserved Rit GTPase-p38 MAPK signaling pathway mediates oxidative stress resistance. Mol Biol Cell. 2011 Sep;22(17):3231–41.

90. Rane MJ, Pan Y, Singh S, Powell DW, Wu R, Cummins T, et al. Heat shock protein 27 controls apoptosis by regulating Akt activation. J Biol Chem. 2003 Jul 25;278(30):27828–35.

91. Zheng C, Lin Z, Zhao ZJ, Yang Y, Niu H, Shen X. MAPK-activated protein kinase-2 (MK2)-mediated formation and phosphorylation-regulated dissociation of the signal complex consisting of p38, MK2, Akt, and Hsp27. J Biol Chem. 2006 Dec 1;281(48):37215–26.

92. Wu R, Kausar H, Johnson P, Montoya-Durango DE, Merchant M, Rane MJ. Hsp27 regulates Akt activation and polymorphonuclear leukocyte apoptosis by scaffolding MK2 to Akt signal complex. J Biol Chem. 2007 Jul 27;282(30):21598–608.

93. Cai W, Andres DA. mTORC2 is required for rit-mediated oxidative stress resistance. PLoS One. 2014 Dec 22;9(12):e115602.

94. Rodriguez-Viciana P, Sabatier C, McCormick F. Signaling specificity by Ras family GTPases is determined by the full spectrum of effectors they regulate. Mol Cell Biol. 2004 Jun;24(11):4943–54.

95. Yuan TL, Cantley LC. PI3K pathway alterations in cancer: variations on a theme. Oncogene. 2008 Sep 18;27(41):5497–510.

96. Shi G-X, Jin L, Andres DA. A rit GTPase-p38 mitogen-activated protein kinase survival pathway confers resistance to cellular stress. Mol Cell Biol. 2011 May;31(10):1938–48.

97. Cai W, Rudolph JL, Sengoku T, Andres DA. Rit GTPase regulates a p38 MAPK-dependent neuronal survival pathway. Neurosci Lett. 2012 Dec 7;531(2):125–30.

98. Wang G-F, Dong Q, Bai Y, Yuan J, Xu Q, Cao C, et al. Oxidative stress induces mitotic arrest by inhibiting Aurora A-involved mitotic spindle formation. Free Radic Biol Med. 2017 Feb;103:177–87.

99. Hynds DL, Spencer ML, Andres DA, Snow DM. Rit promotes MEK-independent neurite branching in human neuroblastoma cells. J Cell Sci. 2003 May 15;116(Pt 10):1925–35.

100. Tian Y, Shao L, Wang Q, Ru G, Zhai C, Zhou L. NECAB3 promotes the migration and invasion of liver cancer cells through HIF-1α/RIT1 signaling pathway. Open Med. 2023 May 16;18(1):20230700.

101. Abe T, Kanno S-I, Niihori T, Terao M, Takada S, Aoki Y. LZTR1 deficiency exerts high metastatic potential by enhancing sensitivity to EMT induction and controlling KLHL12-mediated collagen secretion. Cell Death Dis. 2023 Aug 25;14(8):556.

102. Meng Z, Moroishi T, Guan K-L. Mechanisms of Hippo pathway regulation. Genes Dev. 2016 Jan 1;30(1):1–17.

103. Gysin S, Salt M, Young A, McCormick F. Therapeutic strategies for targeting ras proteins. Genes Cancer. 2011 Mar;2(3):359–72.

104. Moore AR, Rosenberg SC, McCormick F, Malek S. RAS-targeted therapies: is the undruggable drugged? Nat Rev Drug Discov. 2020 Aug;19(8):533–52.

105. Ostrem JM, Peters U, Sos ML, Wells JA, Shokat KM. K-Ras(G12C) inhibitors allosterically control GTP affinity and effector interactions. Nature. 2013 Nov 28;503(7477):548–51.

106. Llovet JM, Ricci S, Mazzaferro V, Hilgard P, Gane E, Blanc J-F, et al. Sorafenib in Advanced Hepatocellular Carcinoma. N Engl J Med. 2008 Jul 24;359(4):378–90.

107. Meraldi P, Draviam VM, Sorger PK. Timing and checkpoints in the regulation of mitotic progression. Dev Cell. 2004 Jul;7(1):45–60.

108. Topham CH, Taylor SS. Mitosis and apoptosis: how is the balance set? Curr Opin Cell Biol. 2013;25(6):780–5.

109. Sivakumar S, Daum JR, Gorbsky GJ. Live-cell fluorescence imaging for phenotypic analysis of mitosis. Methods Mol Biol. 2014;1170:549–62.

110. Kanda T, Sullivan KF, Wahl GM. Histone–GFP fusion protein enables sensitive analysis of chromosome dynamics in living mammalian cells. Curr Biol. 1998 Mar 26;8(7):377–85.

111. Santaguida S, Tighe A, D'Alise AM, Taylor SS, Musacchio A. Dissecting the role of MPS1 in chromosome biorientation and the spindle checkpoint through the small molecule inhibitor reversine. J Cell Biol. 2010 Jul 12;190(1):73–87.

112. Dobles M, Liberal V, Scott ML, Benezra R, Sorger PK. Chromosome missegregation and apoptosis in mice lacking the mitotic checkpoint protein Mad2. Cell. 2000 Jun 9;101(6):635–45.

113. Iwanaga Y, Chi Y-H, Miyazato A, Sheleg S, Haller K, Peloponese J-M Jr, et al. Heterozygous deletion of mitotic arrest-deficient protein 1 (MAD1) increases the incidence of tumors in mice. Cancer Res. 2007 Jan 1;67(1):160–6.

114. Li M, Fang X, Wei Z, York JP, Zhang P. Loss of spindle assembly checkpoint-mediated inhibition of Cdc20 promotes tumorigenesis in mice. J Cell Biol. 2009 Jun 15;185(6):983–94.

115. Zeng X, Xu WK, Lok TM, Ma HT, Poon RYC. Imbalance of the spindle-assembly checkpoint promotes spindle poison-mediated cytotoxicity with distinct kinetics. Cell Death Dis. 2019 Apr 5;10(4):314.

116. Yu F, Jiang Y, Lu L, Cao M, Qiao Y, Liu X, et al. Aurora-A promotes the establishment of spindle assembly checkpoint by priming the Haspin-Aurora-B feedback loop in late G2 phase. Cell Discov. 2017 Jan 10;3:16049.

117. Courtheoux T, Diallo A, Damodaran AP, Reboutier D, Watrin E, Prigent C. Aurora A kinase activity is required to maintain an active spindle assembly checkpoint during prometaphase. J Cell Sci [Internet]. 2018 Apr 12;131(7). Available from: http://dx.doi.org/10.1242/jcs.191353

118. Skowyra A, Allan LA, Saurin AT, Clarke PR. USP9X Limits Mitotic Checkpoint Complex Turnover to Strengthen the Spindle Assembly Checkpoint and Guard against Chromosomal Instability. Cell Rep. 2018 Apr 17;23(3):852–65.

119. Doench JG, Fusi N, Sullender M, Hegde M, Vaimberg EW, Donovan KF, et al. Optimized sgRNA design to maximize activity and minimize off-target effects of CRISPR-Cas9. Nat Biotechnol. 2016 Feb;34(2):184–91.

120. Shah KN, Bhatt R, Rotow J, Rohrberg J, Olivas V, Wang VE, et al. Aurora kinase A drives the evolution of resistance to third-generation EGFR inhibitors in lung cancer. Nat Med. 2019 Jan;25(1):111–8.

121. Alfieri C, Chang L, Zhang Z, Yang J, Maslen S, Skehel M, et al. Molecular basis of APC/C regulation by the spindle assembly checkpoint. Nature. 2016 Aug 25;536(7617):431–6.

122. Yamaguchi M, VanderLinden R, Weissmann F, Qiao R, Dube P, Brown NG, et al. Cryo-EM of Mitotic Checkpoint Complex-Bound APC/C Reveals Reciprocal and Conformational Regulation of Ubiquitin Ligation. Mol Cell. 2016 Aug 18;63(4):593–607.

123. Ciechanover A, Schwartz AL. The ubiquitin-proteasome pathway: the complexity and myriad functions of proteins death. Proc Natl Acad Sci U S A. 1998 Mar 17;95(6):2727–30.

124. French ME, Koehler CF, Hunter T. Emerging functions of branched ubiquitin chains. Cell Discov. 2021 Jan 26;7(1):6.

125. Yang Q, Zhao J, Chen D, Wang Y. E3 ubiquitin ligases: styles, structures and functions. Mol Biomed. 2021 Jul 30;2(1):23.

126. Canning P, Cooper CDO, Krojer T, Murray JW, Pike ACW, Chaikuad A, et al. Structural Basis for Cul3 Protein Assembly with the BTB-Kelch Family of E3 Ubiquitin Ligases*. J Biol Chem. 2013 Mar 15;288(11):7803–14.

127. Mevissen TET, Komander D. Mechanisms of Deubiquitinase Specificity and Regulation. Annu Rev Biochem. 2017 Jun 20;86:159–92.

128. Hanpude P, Bhattacharya S, Dey AK, Maiti TK. Deubiquitinating enzymes in cellular signaling and disease regulation. IUBMB Life. 2015 Jul;67(7):544–55.

129. Cooper GM, Stone EA, Asimenos G, NISC Comparative Sequencing Program, Green ED, Batzoglou S, et al. Distribution and intensity of constraint in mammalian genomic sequence. Genome Res. 2005 Jul;15(7):901–13.

130. Noma T, Kanai Y, Kanai-Azuma M, Ishii M, Fujisawa M, Kurohmaru M, et al. Stage- and sex-dependent expressions of Usp9x, an X-linked mouse ortholog of Drosophila Fat facets, during gonadal development and oogenesis in mice. Gene Expr Patterns. 2002 Nov;2(1–2):87–91.

131. Naik E, Webster JD, DeVoss J, Liu J, Suriben R, Dixit VM. Regulation of proximal T cell receptor signaling and tolerance induction by deubiquitinase Usp9X. J Exp Med. 2014 Sep 22;211(10):1947–55.

132. Jones MH, Furlong RA, Burkin H, Chalmers IJ, Brown GM, Khwaja O, et al. The Drosophila developmental gene fat facets has a human homologue in Xp11.4 which escapes X-inactivation and has related sequences on Yq11.2. Hum Mol Genet. 1996 Nov;5(11):1695–701.

133. Murtaza M, Jolly LA, Gecz J, Wood SA. La FAM fatale: USP9X in development and disease. Cell Mol Life Sci. 2015 Jun;72(11):2075–89.

134. Fischer-Vize JA, Rubin GM, Lehmann R. The fat facets gene is required for Drosophila eye and embryo development. Development. 1992 Dec;116(4):985–1000.

135. Wood SA, Pascoe WS, Ru K, Yamada T, Hirchenhain J, Kemler R, et al. Cloning and expression analysis of a novel mouse gene with sequence similarity to the Drosophila fat facets gene. Mech Dev. 1997 Apr;63(1):29–38.

136. Ryoo HD, Bergmann A, Gonen H, Ciechanover A, Steller H. Regulation of Drosophila IAP1 degradation and apoptosis by reaper and ubcD1. Nat Cell Biol. 2002 Jun;4(6):432–8.

137. Wing JP, Schreader BA, Yokokura T, Wang Y, Andrews PS, Huseinovic N, et al. Drosophila Morgue is an F box/ubiquitin conjugase domain protein important for grim-reaper mediated apoptosis. Nat Cell Biol. 2002 Jun;4(6):451–6.

138. Schwickart M, Huang X, Lill JR, Liu J, Ferrando R, French DM, et al. Deubiquitinase USP9X stabilizes MCL1 and promotes tumour cell survival. Nature. 2010 Jan 7;463(7277):103–7.

139. Savio MG, Wollscheid N, Cavallaro E, Algisi V, Di Fiore PP, Sigismund S, et al. USP9X Controls EGFR Fate by Deubiquitinating the Endocytic Adaptor Eps15. Curr Biol. 2016 Jan 25;26(2):173–83.

140. Chen H, Polo S, Di Fiore PP, De Camilli PV. Rapid Ca^{2+}-dependent decrease of protein ubiquitination at synapses. Proc Natl Acad Sci U S A. 2003 Dec 9;100(25):14908–13.

141. Marx C, Held JM, Gibson BW, Benz CC. ErbB2 trafficking and degradation associated with K48 and K63 polyubiquitination. Cancer Res. 2010 May 1;70(9):3709–17.

142. Murray RZ, Jolly LA, Wood SA. The FAM deubiquitylating enzyme localizes to multiple points of protein trafficking in epithelia, where it associates with E-cadherin and beta-catenin. Mol Biol Cell. 2004 Apr;15(4):1591–9.

143. Strutt H, Searle E, Thomas-Macarthur V, Brookfield R, Strutt D. A Cul-3-BTB ubiquitylation pathway regulates junctional levels and asymmetry of core planar polarity proteins. Development. 2013 Apr;140(8):1693–702.

144. Théard D, Labarrade F, Partisani M, Milanini J, Sakagami H, Fon EA, et al. USP9x-mediated deubiquitination of EFA6 regulates de novo tight junction assembly. EMBO J. 2010 May 5;29(9):1499–509.

145. Luton F, Klein S, Chauvin J-P, Le Bivic A, Bourgoin S, Franco M, et al. EFA6, exchange factor for ARF6, regulates the actin cytoskeleton and associated tight junction in response to E-cadherin engagement. Mol Biol Cell. 2004 Mar;15(3):1134–45.

146. Trinkle-Mulcahy L, Boulon S, Lam YW, Urcia R, Boisvert F-M, Vandermoere F, et al. Identifying specific protein interaction partners using quantitative mass spectrometry and bead proteomes. J Cell Biol. 2008 Oct 20;183(2):223–39.

147. Urbé S, Liu H, Hayes SD, Heride C, Rigden DJ, Clague MJ. Systematic survey of deubiquitinase localization identifies USP21 as a regulator of centrosome- and microtubule-associated functions. Mol Biol Cell. 2012 Mar;23(6):1095–103.

148. Potu H, Peterson LF, Kandarpa M, Pal A, Sun H, Durham A, et al. Usp9x regulates Ets-1 ubiquitination and stability to control NRAS expression and tumorigenicity in melanoma. Nat Commun. 2017 Feb 15;8:14449.

149. Dietachmayr M, Rathakrishnan A, Karpiuk O, von Zweydorf F, Engleitner T, Fernández-Sáiz V, et al. Antagonistic activities of CDC14B and CDK1 on USP9X regulate WT1-dependent mitotic transcription and survival. Nat Commun. 2020 Mar 9;11(1):1268.

150. Paudel P, Zhang Q, Leung C, Greenberg HC, Guo Y, Chern Y-H, et al. Crystal structure and activity-based labeling reveal the mechanisms for linkage-specific substrate recognition by deubiquitinase USP9X. Proc Natl Acad Sci U S A. 2019 Apr 9;116(15):7288–97.

151. Wrobel L, Siddiqi FH, Hill SM, Son SM, Karabiyik C, Kim H, et al. mTORC2 Assembly Is Regulated by USP9X-Mediated Deubiquitination of RICTOR. Cell Rep. 2020 Dec 29;33(13):108564.

152. Wang P, Wang J, Yao S, Cui M, Cheng Y, Liu W, et al. Deubiquitinase USP9X stabilizes RNA m6A demethylase ALKBH5 and promotes acute myeloid leukemia cell survival. J Biol Chem. 2023 Aug;299(8):105055.

153. Rott R, Szargel R, Haskin J, Bandopadhyay R, Lees AJ, Shani V, et al. α-Synuclein fate is determined by USP9X-regulated monoubiquitination. Proc Natl Acad Sci U S A. 2011 Nov 15;108(46):18666–71.

154. Imielinski M, Berger AH, Hammerman PS, Hernandez B, Pugh TJ, Hodis E, et al. Mapping the hallmarks of lung adenocarcinoma with massively parallel sequencing. Cell. 2012 Sep 14;150(6):1107–20.

155. Gillette MA, Satpathy S, Cao S, Dhanasekaran SM, Vasaikar SV, Krug K, et al. Proteogenomic Characterization Reveals Therapeutic Vulnerabilities in Lung Adenocarcinoma. Cell. 2020 Jul 9;182(1):200-225.e35.

156. Lengel HB, Mastrogiacomo B, Connolly JG, Tan KS, Liu Y, Fick CN, et al. Genomic mapping of metastatic organotropism in lung adenocarcinoma. Cancer Cell. 2023 May 8;41(5):970-985.e3.

157. Chen J, Yang H, Teo ASM, Amer LB, Sherbaf FG, Tan CQ, et al. Genomic landscape of lung adenocarcinoma in East Asians. Nat Genet. 2020 Feb;52(2):177–86.

158. Rizvi NA, Hellmann MD, Snyder A, Kvistborg P, Makarov V, Havel JJ, et al. Cancer immunology. Mutational landscape determines sensitivity to PD-1 blockade in non-small cell lung cancer. Science. 2015 Apr 3;348(6230):124–8.

159. Chen X, Yu C, Gao J, Zhu H, Cui B, Zhang T, et al. A novel USP9X substrate TTK contributes to tumorigenesis in non-small-cell lung cancer. Theranostics. 2018 Mar 22;8(9):2348–60.

160. Wang T, Jing B, Sun B, Liao Y, Song H, Xu D, et al. Stabilization of PTGES by deubiquitinase USP9X promotes metastatic features of lung cancer via PGE2 signaling. Am J Cancer Res. 2019 Jun 1;9(6):1145–60.

161. Jie X, Fong WP, Zhou R, Zhao Y, Zhao Y, Meng R, et al. USP9X-mediated KDM4C deubiquitination promotes lung cancer radioresistance by epigenetically inducing TGF-β2 transcription. Cell Death Differ. 2021 Jul;28(7):2095–111.

162. Wang Y, Liu Y, Yang B, Cao H, Yang C-X, Ouyang W, et al. Elevated expression of USP9X correlates with poor prognosis in human non-small cell lung cancer. J Thorac Dis. 2015 Apr;7(4):672–9.

163. Homan CC, Kumar R, Nguyen LS, Haan E, Raymond FL, Abidi F, et al. Mutations in USP9X are associated with X-linked intellectual disability and disrupt neuronal cell migration and growth. Am J Hum Genet. 2014 Mar 6;94(3):470–8.

164. Reijnders MRF, Zachariadis V, Latour B, Jolly L, Mancini GM, Pfundt R, et al. De Novo Loss-of-Function Mutations in USP9X Cause a Female-Specific Recognizable Syndrome with Developmental Delay and Congenital Malformations. Am J Hum Genet. 2016 Feb 4;98(2):373–81.

165. Cao J, Wu L, Zhang S-M, Lu M, Cheung WKC, Cai W, et al. An easy and efficient inducible CRISPR/Cas9 platform with improved specificity for multiple gene targeting. Nucleic Acids Res. 2016 Nov 2;44(19):e149.

166. Lundberg AS, Randell SH, Stewart SA, Elenbaas B, Hartwell KA, Brooks MW, et al. Immortalization and transformation of primary human airway epithelial cells by gene transfer. Oncogene. 2002 Jul 4;21(29):4577–86.

167. Asimaki E, Petriukov K, Renz C, Meister C, Ulrich HD. Fast friends - Ubiquitin-like modifiers as engineered fusion partners. Semin Cell Dev Biol. 2022 Dec;132:132–45.

168. Nusinow DP, Szpyt J, Ghandi M, Rose CM, McDonald ER 3rd, Kalocsay M, et al. Quantitative Proteomics of the Cancer Cell Line Encyclopedia. Cell. 2020 Jan 23;180(2):387-402.e16.

169. Ghandi M, Huang FW, Jané-Valbuena J, Kryukov GV, Lo CC, McDonald ER 3rd, et al. Next-generation characterization of the Cancer Cell Line Encyclopedia. Nature. 2019 May;569(7757):503–8.

170. Kapuria V, Peterson LF, Fang D, Bornmann WG, Talpaz M, Donato NJ. Deubiquitinase inhibition by small-molecule WP1130 triggers aggresome formation and tumor cell apoptosis. Cancer Res. 2010 Nov 15;70(22):9265–76.

171. Peddaboina C, Jupiter D, Fletcher S, Yap JL, Rai A, Tobin RP, et al. The downregulation of Mcl-1 via USP9X inhibition sensitizes solid tumors to Bcl-xl inhibition. BMC Cancer. 2012 Nov 21;12:541.

172. Wang S, Kollipara RK, Srivastava N, Li R, Ravindranathan P, Hernandez E, et al. Ablation of the oncogenic transcription factor ERG by deubiquitinase inhibition in prostate cancer. Proc Natl Acad Sci U S A. 2014 Mar 18;111(11):4251–6.

173. Perry JW, Ahmed M, Chang K-O, Donato NJ, Showalter HD, Wobus CE. Antiviral activity of a small molecule deubiquitinase inhibitor occurs via induction of the unfolded protein response. PLoS Pathog. 2012 Jul 5;8(7):e1002783.

174. Charbonneau M-E, Gonzalez-Hernandez MJ, Showalter HD, Donato NJ, Wobus CE, O'Riordan MXD. Small molecule deubiquitinase inhibitors promote macrophage anti-infective capacity. PLoS One. 2014 Aug 5;9(8):e104096.

175. Jaiswal A, Murakami K, Elia A, Shibahara Y, Done SJ, Wood SA, et al. Therapeutic inhibition of USP9x-mediated Notch signaling in triple-negative breast cancer. Proc Natl Acad Sci U S A [Internet]. 2021 Sep 21;118(38). Available from: http://dx.doi.org/10.1073/pnas.2101592118

176. Pal A, Dziubinski M, Di Magliano MP, Simeone DM, Owens S, Thomas D, et al. Usp9x Promotes Survival in Human Pancreatic Cancer and Its Inhibition Suppresses Pancreatic Ductal Adenocarcinoma In Vivo Tumor Growth. Neoplasia. 2018 Feb;20(2):152–64.

177. Akiyama H, Umezawa Y, Watanabe D, Okada K, Ishida S, Nogami A, et al. Inhibition of USP9X Downregulates JAK2-V617F and Induces Apoptosis Synergistically with BH3 Mimetics Preferentially in Ruxolitinib-Persistent JAK2-V617F-Positive Leukemic Cells. Cancers [Internet]. 2020 Feb 10;12(2). Available from: http://dx.doi.org/10.3390/cancers12020406

178. Peterson LF, Sun H, Liu Y, Potu H, Kandarpa M, Ermann M, et al. Targeting deubiquitinase activity with a novel small-molecule inhibitor as therapy for B-cell malignancies. Blood. 2015 Jun 4;125(23):3588–97.

179. Potu H, Peterson LF, Pal A, Verhaegen M, Cao J, Talpaz M, et al. Usp5 links suppression of p53 and FAS levels in melanoma to the BRAF pathway. Oncotarget. 2014 Jul 30;5(14):5559–69.

180. Clancy A, Heride C, Pinto-Fernández A, Elcocks H, Kallinos A, Kayser-Bricker KJ, et al. The deubiquitylase USP9X controls ribosomal stalling. J Cell Biol [Internet]. 2021 Mar 1;220(3). Available from: http://dx.doi.org/10.1083/jcb.202004211

181. Lopez J, Bonsor DA, Sale MJ, Urisman A, Mehalko JL, Cabanski-Dunning M, et al. The ribosomal S6 kinase 2 (RSK2)-SPRED2 complex regulates the phosphorylation of RSK substrates and MAPK signaling. J Biol Chem. 2023 Jun;299(6):104789.

182. Chalkley RJ, Baker PR. Use of a glycosylation site database to improve glycopeptide identification from complex mixtures. Anal Bioanal Chem. 2017 Jan;409(2):571–7.

183. Pino LK, Searle BC, Bollinger JG, Nunn B, MacLean B, MacCoss MJ. The Skyline ecosystem: Informatics for quantitative mass spectrometry proteomics. Mass Spectrom Rev. 2020 May;39(3):229–44.

184. Choi M, Chang C-Y, Clough T, Broudy D, Killeen T, MacLean B, et al. MSstats: an R package for statistical analysis of quantitative mass spectrometry-based proteomic experiments. Bioinformatics. 2014 Sep 1;30(17):2524–6.

185. Dempster JM, Rossen J, Kazachkova M, Pan J, Kugener G, Root DE, et al. Extracting Biological Insights from the Project Achilles Genome-Scale CRISPR Screens in Cancer Cell Lines [Internet]. bioRxiv. 2019 [cited 2023 Oct 25]. p. 720243. Available from: https://www.biorxiv.org/content/10.1101/720243v1

186. Perez-Riverol Y, Bai J, Bandla C, García-Seisdedos D, Hewapathirana S, Kamatchinathan S, et al. The PRIDE database resources in 2022: a hub for mass spectrometry-based proteomics evidences. Nucleic Acids Res. 2022 Jan 7;50(D1):D543–52.

187. Fumarola C, Bonelli MA, Petronini PG, Alfieri RR. Targeting PI3K/AKT/mTOR pathway in non small cell lung cancer. Biochem Pharmacol. 2014 Aug 1;90(3):197–207.

VITA

Amanda Riley grew up in Cary, North Carolina. She received her Bachelor of Science degree in Biology, *summa cum laude*, and graduated as valedictorian of her class at Muhlenberg College in 2016. As an undergraduate, she gained research experience during summer internships. In the summer of 2014, she worked at Novartis Vaccines (now Seqirus) in the Manufacturing Science and Technology Division. There, she worked in an analytical chemistry lab and gained experience using LC-MS to test influenza vaccine samples for hemagglutinin protein levels. In the summer of 2015, she worked at Duke University in Dr. David Hinton's lab in the Nicolas School of the Environment. In the Hinton Lab, she studied the effects of pollution adaptation on liver development in killifish. From this work, she published her first peer-reviewed, first-author journal article. After graduating from college in 2016, Amanda worked as a research technician in Dr. Cyril Benes' lab at the Massachusetts General Hospital Cancer Center in Boston, Massachusetts. In the Benes lab, she generated patient-derived cell lines to study resistance mechanisms to tyrosine kinase inhibitors. From this work, she is recognized as a co-author on five peer-reviewed publications. She enrolled in the Molecular and Cellular Biology PhD program at the University of Washington in 2018 and joined Dr. Alice Berger's lab at the Fred Hutch Cancer Center in 2019. During her dissertation work, she applied her skills in biochemistry and cell biology to understand genetic vulnerabilities in lung cancer. Throughout her time in graduate school, she received many accolades for her work, including two poster presentation prizes (including first place and the coveted Galloway Cup!). She also received several competitive training grants, including an F31 grant from the NIH. She was recognized as a Promising Young Scientist in an article from the Brotman Baty Institute, which highlighted her achievements and academic successes. In her free time, she enjoys yoga, running, swimming, live music, and outdoor picnics.